CHROMATIC CONFOCAL GAUGING FOR HIGH PRECISION DIMENSIONAL METROLOGY

by

Mathieu Rayer

Submitted for the degree of
Engineering Doctorate

School of Engineering and Physical Sciences

Institute of Photonics and Quantum Sciences
Heriot-Watt University

April 2015

The copyright of this thesis is owned by the author. Any quotation from the thesis or use of any information contained in it must acknowledge this thesis as the source of the quotation or information.

Abstract

Interest in the chromatic confocal microscope in the high precision dimensional metrology industry is growing rapidly. In fact, the chromatic confocal microscope offers a “stylus like” distance measurement applicable to various surface types. In addition, the chromatic confocal microscope can potentially compete in resolution with contact measurement probes, while significantly increasing the sampling rate to several kHz. Therefore, such technology is key to the Taylor Hobson Ltd. strategy. The work embodied in this thesis focuses on the design, development, and evaluation of a low cost and high resolution version of the chromatic confocal microscope. Both product are currently in pre-production phase.

The low cost version the chromatic confocal microscope is designed to be a compact and cost effective system while exhibiting “state of the art” performances. In fact, the raw material cost of the system is below £500, this being achieved while exhibiting an optical head outer diameter of 8 mm, a working distance of more than 27 mm, and a resolution better than 100 nm over a measurement range exceeding 7 mm.

The high resolution version of the chromatic confocal microscope is dedicated to precision. The aim of the design is to exhibit the highest achievable resolution while maintaining a measurement working distance exceeding 12 mm. By tailoring the chromatic dispersion to be appropriately low, a resolution of better than 10 nm is achieved.

Both designs have been tailored within a few design cycles; this has been achieved through the development of two novel models, the spectral irradiance model and the measurement standard deviation model. The spectral irradiance model enables the analytical estimation of the chromatic confocal peak from only the optical parameters of the optical heads. Based on a geometric approach; this is more than 5 times more precise than the previously used model based on wave optics. Furthermore, by applying a fully integrated system design approach incorporating design, production, and test of optical systems, the resulting chromatic confocal system surpasses comparable commercially available chromatic confocal gauges in terms of cost, resolution, numerical aperture, range of measurement, and working distance. Such performance is further enhanced by the use of staircase diffractive surfaces. Staircase diffractive surfaces are special hybrid aspheric diffractive surfaces exhibiting insignificant manufacturing losses allowing the design to be only limited by the scalar diffraction theory used by ray tracing packages. In addition, staircase diffractive lenses permit the passively athermalisation of the optical head of the chromatic confocal microscope.

The work encapsulated in this thesis extends the current understanding of the measurement environment impact on chromatic confocal gauges. This study includes the impact of the surface reflectivity, roughness, and slope onto the linearity of the chromatic confocal microscope. Using the previously described findings, methods to mitigate the linearity error induced by the surface roughness, reflectivity, and slope are presented and applied.

To Verena and Samuel

Acknowledgements

This Engineering Doctorate has been a unique experience filled with countless encounters during conferences, company visits, EngD meetings, external projects, *et al...* For me this program has been first a human experience. All of these people contributed one way or another to this work and I would like to express my thanks to them all.

I would like to deeply thank my academic and industrial supervisors Professor Ajoy Kar and Daniel Mansfield for their support throughout this Engineering Doctorate. Bob Bennett, should be also added to the supervisors or shall I say mentors. Each in their role; Ajoy as academic writing master, Daniel as word-smith and technical bible, and Bob as business and technology savvy, made this Engineering Doctorate the most rewarding experience of my career thus far. Their support has often been beyond their supervising role.

I gratefully acknowledge Taylor Hobson Ltd., Precitech Inc., and Solartron Metrology Ltd. for funding this research as well as EPSRC for my scholarship that made this research possible.

Jeff Roblee deserves my gratitude for is support and priceless advice. His enthusiasm is contagious!

I would like to thank all the Taylor Hobson Ltd. employees and especially Pete Ferguson, Jon Hackett, and Neil Fitzgibbon for their support. They supported me with countless advice and gave me hours (more than they had too) of their precious time. They made my time at Taylor Hobson Ltd. a real pleasure.

I thank as well all the IDC staff, especially Alison Low and Linda Bruce, for their friendly support.

I sincerely thank as well my parents in law, Werner and Brigite, who supported me more often than they should have.

I also would like to thank my family and particularly my parents, Jacques and Bernadette, who believed in me before I did and supported me during my 9 years as a student. I am also thinking in particular to my grand-parents for whom such a social elevation would not have been possible. I would not have completed this program without their faith and investment in the future generations.

I also would like to thank my son, Samuel. You will not remember this time, but your patience and happiness gave me the strength to write this thesis, a piece of you is in it.

Last but not least, I am deeply thankful to my wife Verena, she is the one who convinced me 4 years ago that I could actually manage such a program. During the Doctorate program, she became my wife and the mother of our son Samuel, while being the most precious daily support I could have dreamt of. I am proud of you and love you.

ACADEMIC REGISTRY

Research Thesis Submission

Name*:*	Mathieu Rayer		
School/PGI:	**School of engineering and physical sciences**		
Version: *(i.e. First, Resubmission, Final)*	Final	Degree Sought (Award **and** Subject area)	EngD, Optics and Photonics Technologies

Declaration

In accordance with the appropriate regulations I hereby submit my thesis and I declare that:

1) the thesis embodies the results of my own work and has been composed by myself
2) where appropriate, I have made acknowledgement of the work of others and have made reference to work carried out in collaboration with other persons
3) the thesis is the correct version of the thesis for submission and is the same version as any electronic versions submitted*.
4) my thesis for the award referred to, deposited in the Heriot-Watt University Library, should be made available for loan or photocopying and be available via the Institutional Repository, subject to such conditions as the Librarian may require
5) I understand that as a student of the University I am required to abide by the Regulations of the University and to conform to its discipline.

* *Please note that it is the responsibility of the candidate to ensure that the correct version of the thesis is submitted.*

Signature of Candidate*:*		Date:	01/05/15

Submission

Submitted By *(name in capitals):*	
Signature of Individual Submitting:	
Date Submitted:	

For Completion in the Student Service Centre (SSC)

Received in the SSC by *(name in capitals):*			
Method of Submission *(Handed in to SSC; posted through internal/external mail):*			
E-thesis Submitted (***mandatory for final theses)***			
Signature:		Date:	

Contents

List of Tables

List of Figures

Glossary

AFM Atomic Force Microscopy.

BCG Boston Consulting Group.

BIPM Bureau International des Poids et Mesures.

CCD Charge-Coupled Device.

CCM Chromatic Confocal microscope.

CCSM Chromatic Confocal Spectral Microscope.

CMM Cordinate Measurement Machine.

CMOS Complementary Metal Oxide Semiconductor.

CNC Computer Numerical Control.

DMAIC Define, Measure, Analyse, Improve, and Control.

DNR Dynamic Range.

DRI Dispersed Reference Interferometer.

DSP Digital Signal Processor.

FTS Fourier Transform Spectrometer.

FWHM Full Width Half Minimum.

GRIN Gradient Index.

HAD Hybrid Aspheric Diffractive.

IP Intellectual Property.

IR Infra Red.

LED Light Emitting Diode.

LVDT Linear Variable Differential Transducer.

LVF Linear Variable Filter.

MTF Modulated Transfer Function.

MWLI Multi-wavelength interferometer.

NA Numerical Aperture.

NIR Near Infra Red.

NIST National Institute of Standards and Technology.

NVTM Normal Vector Tracing Method.

OPD Optical Path Difference.

P2P Peak To Peak.

P2V Peak to Valley.

PDCA Plan, Do, Check, and Act.

PGI Phase Grating Interferometer.

PLC Product Life Cycle.

PSD Position Sensitive Detector.

PSF Point Spread Function.

RMS Root Mean Square.

ROI Return On Investment.

SDS Step Diffractive Surface.

SLED Super-luminescent Light Emitting Diode.

SNR Signal to Noise Ratio.

SPDT Single Point Diamond Turning Machining.

SWOT Strength, Weakness, Opportunity, and Threat.

TQM Total Quality Management.

TRL Technology Readiness Level.

UV Ultra Violet.

VHG Volume Holographic Grating.

WBS Work Breakdown Structure.

List of publication by the candidate

M. Rayer, "Chromatic confocal metrological apparatus", Patent WO2013093459, December 19, 2012.

M. Rayer, "Analysing and machining an optical profile", Patent WO2014080207, November 21, 2013.

M. Rayer, D. Mansfield, "Chromatic confocal microscope using hybrid aspheric diffractive lenses", In Proc. SPIE 9130, *Micro-Optics 2014*, 91300Z (May 10, 2014).

M. Rayer and D. Mansfield, "Chromatic confocal microscopy using staircase diffractive surface", *Applied optics*, vol. 53, no. 23, pp. 5123-5130 (2014).

Chapter 1

Introduction

1.1 Surface and form metrology in industrial management

In order to understand the field of high precision dimensional metrology a little bit of history can help. In 1886, William Taylor and his brother started a small lens manufacturing business. Soon, the small manufacturer became acknowledged as a premium supplier based on the quality of the lenses. Nevertheless, there was no instrument accurate enough to characterise the surface finish of their lenses. In order to determine the surface finish of their lenses, Taylor Hobson needed to create an in-house surface and form measurement instrument to improve even more the quality of their optics. Over the years, high precision dimensional metrology instruments became the speciality of Taylor Hobson Ltd. [1]. This short story shows us that surface and form metrology is an essential tool to understand a product from the macro to the nano scale.

The definition of high precision surface metrology evolves constantly. High precision dimensional metrology is commonly defined by the most precise dimensional metrology instrument currently sold. Today, state of the art instruments like the Phase Grating Interferometer (PGI) Dimension have typically a form error repeatability below 50 nm [2]. The repeatability is defined by the National Institute of Standards and Technology (NIST) and the Bureau

International des Poids et Mesures (BIPM) as the “closeness of the agreement between the results of successive measurements of the same measurand carried out under the same conditions of measurement” [3, 4].

High precision dimensional metrology instruments can be separated in two categories: contact and non-contact. Contact instruments use the motion of a stylus in contact with the surface to convert the surface profile into an electric signal. Historically, this was the first method to be developed. Today, apart from the widespread use of interferometers in the optics industry, the majority of commercial systems are based on this concept. In fact, contact surface metrology is still one of the most precise and robust measurement method. Non-contact dimensional metrology instruments may be broadly divided into two categories, full-field and single point measurement. Through the interaction of light with the surface, the surface texture may be used to modify various light attributes such as phase, polarisation, or frequency.

Quality management is key in todays automotive, aero-spacial and optic industries. Surface and form measurement are an everyday tool in quality management. Total Quality Management (TQM) [5] and Six Sigma [6] are two models used in quality management. One of the main tools in TQM is the Deming wheel shown in Figure 1.1 [5]. The Deming wheel model is applied to optimise a process. In surface and form measurement, the important link is ‘‘check’’. In order to establish if a workpiece fulfils the required tolerances, it is necessary to measure it [7]. An extension of the Deming wheel is the Define, Measure, Analyse, Improve, and Control (DMAIC) [8] loop shown in Figure 1.2.

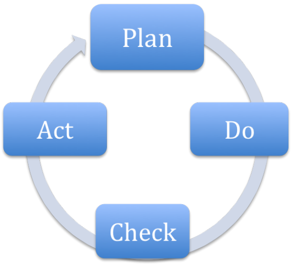

Figure 1.1: The 4 steps of the Deming wheel of continuous improvement: plan, do, check and act.

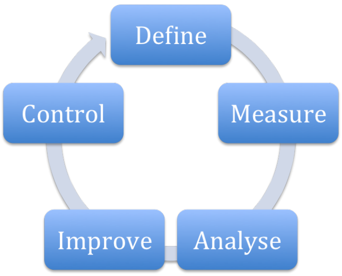

Figure 1.2: The DMAIC concept is represented as a closed loop to illustrate the continuity of the quality management.

Dimensional metrology now appears in "measure" and "control" as shown in Figure 1.2. In addition the DMAIC introduces the notion of standards. In order to be able to define complexes shapes or surface profiles, it necessary to define standards. The currently accepted one is the standard ISO 4287 [7].

This is not an exhaustive description of the role of of dimensional metrology in quality management. Nevertheless, it had been shown that both TQM and Six Sigma models require standards. Dimensional metrology is essential in today's industrial environment. Taylor Hobson Ltd. is engaged in supplying the industry with the best industrial dimensional metrology instruments. Taylor Hobson Ltd. has been involved with high precision engineering since the very beginning of the company. In fact, recent progress in technologies such as Computer Numerical Control (CNC) grinding, Single Point Diamond Turning Machining (SPDT), and multi axis CNC machines, high precision engineering industry is growing at an unprecedented pace.

1.2 Contact surface metrology instrument in the industry

Contact dimensional metrology instrument can be separated in two major categories, stylus based instrument and Atomic Force Microscopy (AFM).

1.2.1 Stylus based instrument

Stylus based instruments are the most commonly used in dimensional surface metrology. The stylus sensor is based on the motion of a stylus induced by the surface profile. The mechanical motion of the stylus is recorded using a variety of transducers; the most widespread one is the ferromagnetic transducer commonly called Linear Variable Differential Transducer (LVDT). The concept of a LVDT is illustrated in Figure 1.3. An LVDT consists of three coils; the central ‘‘primary’’ coil and two secondary coils, together with a ferrite core that can move axially. The primary coil is supplied by an alternative voltage driven at 0.4 to 5 kHz; through induction, this voltage creates a potential in the secondary coils. Any displacement of the ferrite core induces a modification of inductance. The two secondary coils are connected in series. The output voltage is a function of the core position. If the core is in on the middle, the measured voltage is null. Then, if the core moves to one side, the measured voltage increases.

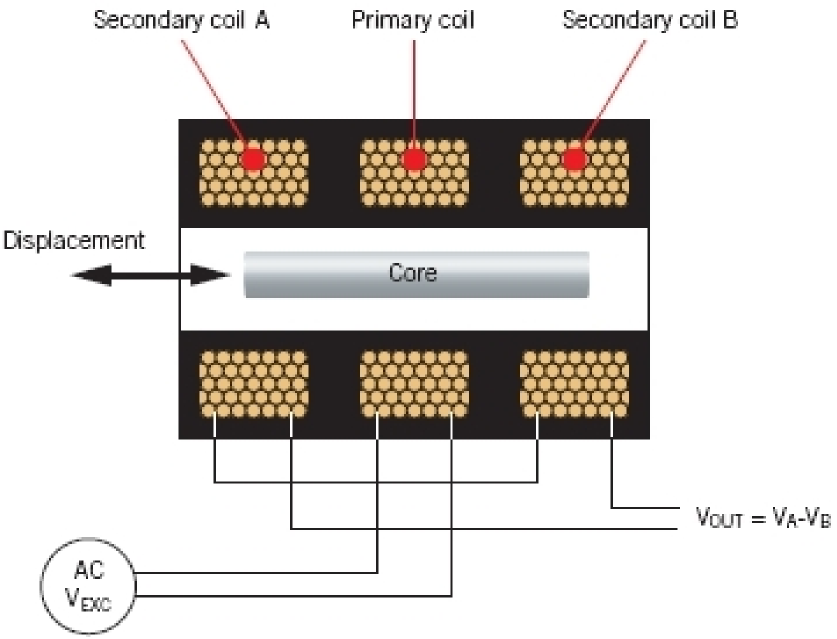

Figure 1.3: Schematic representation of a LVDT, the ferrite core has only one degree of freedom. The motion of the core induce an inductance variation function of the position of the core [9].

Over the central range of movement, the differential voltage output varies linearly as a function of the position of the core. The range of measurement can vary significantly. The measurement uncertainty can reach 0.01 % of the measurement range. The major source of error is temperature change; with a temperature compensation, an error of 100 ppm/°C may be achieved. The major limitation is the reading speed. Due to the probe mechanical assembly frequency response, the measurement cannot be done faster than 1.5 kHz. Nevertheless, stylus tracking requirement typically limits the measurement to few hundred hertz. The major limitation of such a sensor is the dynamic range defined as the ratio of the range of measurement over the resolution of the sensor. The resolution is defined by the BIPM as "smallest change in a quantity being measured that causes a perceptible change in the corresponding indication" [4]. The resolution σ_{res} is defined as

$$\sigma_{res} = k\,\sigma_{N-1}, \tag{1.1}$$

where k expands the interval of confidence. If k is not specified, the value is 3 in order to achieve a interval of confidence of 99.7 % [3]. σ_{n-1} is the sampled standard deviation as well called in this thesis measurement uncertainty and is calculated as

$$\sigma_{N-1} = \sqrt{\frac{1}{N-1}\sum_{n=1}^{N}(x_n - \overline{x})}, \tag{1.2}$$

where N should be at the minimum 200 to be close enough to the standard deviation σ while maintaining the recording time to a few minutes for practicality and temperature stability reasons. In addition, $\overline{x}$ is the arithmetic average of x.

Another approach that enables a probe with a far greater dynamic range to be achieved is based upon tracking the movement of the stylus probe with an interferometer. An excellent example is the PGI [10] gauge of Taylor Hobson Ltd. The schematic principal of the PGI is shown in Figure 1.4. The PGI enables measurements with a resolution of 1 nm and a range of measurement of 12 mm [11].

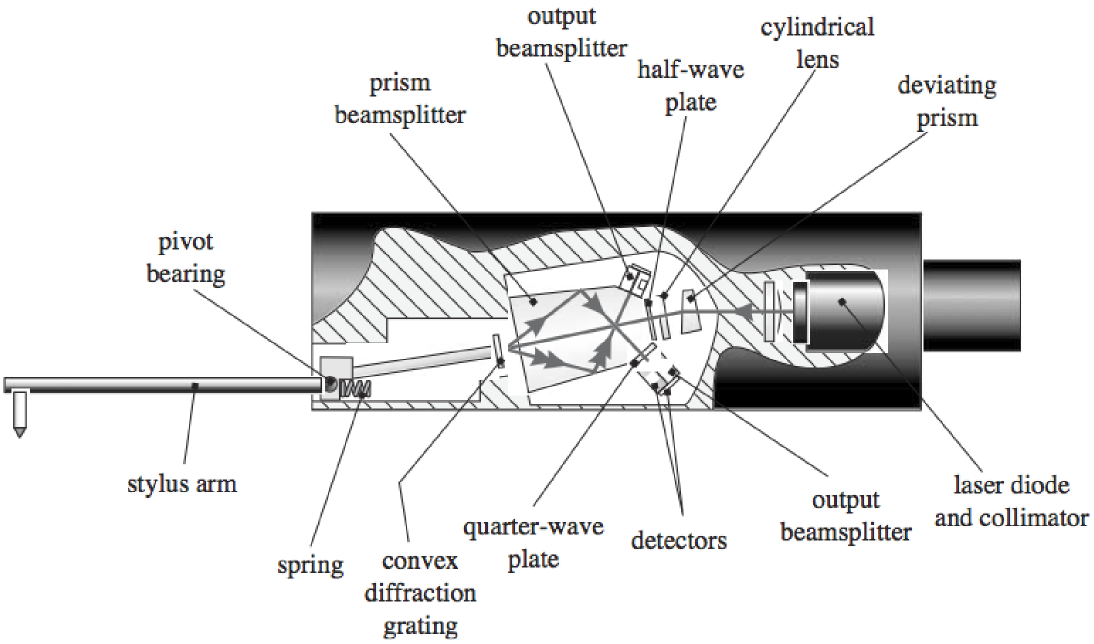

Figure 1.4: Schematic of the PGI gauge. The transverse motion of the stylus is converted to rotation by the pivot. This angular change is transferred to the convex grating [11].

1.2.2 Atomic force microscopy

AFM is not a contact technique. However, the AFM principal can be used as a contact and a non-contact dimensional profiler. Two surfaces interact by creating a bonding force, an attractive or repulsive function of the chemical constitution of the both surfaces [12]. The main force is electrostatic and varies as $1/d^2$ where d is the distance between the two surfaces [12]. This force is used to measure the surface profile. In addition, if the surface is non heterogeneous, the probes is subject to torsion. This torsion can also be measured. Regarding the AFM transducer, it is typically a contact free optical system, capable of measuring the displacement of the tip with a resolution of 0.01 nm [12]. The radius of the tip is few atoms. The displacement of the cantilever induced by the atomic force can be measured using a laser triangulation sensor. Two measurements modes have to be distinguished. Regarding the first mode, the altitude of the sample is controlled in order to keep the force between the tip and the surface constant. The distance between the tip and the surface is around 0.5 nm [12]. This mode is the most sensitive one. Regarding the second mode, the distance between the tip and the surface is around 5 nm and the displacement of the tip is measured directly [12]. The scan can be faster, however a higher traverse speed requires a lower force, hence the measurement uncertainty increases. The lateral range of measurement is limited by the piezoelectric transducer range. To summarise, the vertical range can reach 5 μm, and the lateral range 100 μm [12]. The lateral uncertainty is around 1 % [12]. The axial uncertainty is a few 0.1 nm [12]. Nevertheless, the nature of the surface, such as quantum and chemical states, strongly perturbs the measurement. The measurement speed is limited by the resonance frequency of the stylus. The measurement time can be a few seconds to several minutes for a surface of 100 μm x 100 μm [12]. This technique is suitable for small samples due to the piezoelectric transducer range. In addition, due to the level of measurement uncertainty, the system needs to be stable in temperature and vibration free [12]. Hence, classical linear stages are not suitable and so large areas are technologically difficult to measure with precision. This application domain of an AFM is not the surface finish or the form of an object but more the physical-chemical structure at an atomic level of the surface [12]. This technique is particularly suitable for non conductive materials. The major application domains are material research, microelectronics, ceramics [12].

1.3 Non-contact surface metrology in the industry

Non-contact dimensional metrology instruments in general are progressively becoming more widespread in their use. The need for fast measurement for a variety of component surfaces led to the a development of the non-contact dimensional metrology instruments. Most of them are dedicated to a specific application. Non-contact Non-contact dimensional metrology instruments are currently used when contact dimensional metrology instruments are not suitable, for reasons such as stylus force or stylus resonance frequency. Currently, in the field of high precision non-contact dimensional metrology the more widely used technologies are interferometry and confocal-microscopy.

1.3.1 Interferometer based instruments

Interferometers can be used to measure various types of structures. Nevertheless the principal remains the same. Two waves coherently generated, interfere together to create an interference pattern. If the phase difference $\Delta\phi$ between the arms is [13]

$$\Delta\phi = p\, 2\, \pi, \tag{1.3}$$

where p integer, the two waves interfere constructively. If the phase difference is [13]

$$\Delta\phi = (2p + 1)\, \pi, \tag{1.4}$$

the two waves interfere destructively. More generally, the output irradiance of an interferometer is [13].

$$I = \frac{1}{2}\, I_0 \left(1 + \cos \frac{2\, \pi\, \delta}{\lambda} \right), \tag{1.5}$$

where λ is the illumination wavelength and δ the optical path difference between the two waves. By recording the interferometric irradiance the profile of the sample can be deduced. This static technique is extremely limited, there is no way to determine if the path difference is 1 or m times the wavelength [13]. A more accurate way is to shift gradually the reference mirror to known distances, and record several profiles. This dynamic technique is called ‘‘phase shifting’’. An example of phase shifting interferometer is the Twyman green interferometer shown in Figure 1.5.

The interference pattern is recorded via a Charge-Coupled Device (CCD) sensor. The source is typically a white light source with a interference filter [14]. Each pixel of the detector needs to record at least three values for three positions of the reference mirror [13]. For each measurement, the reference mirror has to be shifted half a wavelength at the maximum due to the Shannon sampling theorem [15].In order to reduce the measurement noise and improve the resolution the number of sample can be increased. For each pixel the measured irradiance I varies sinusoidally

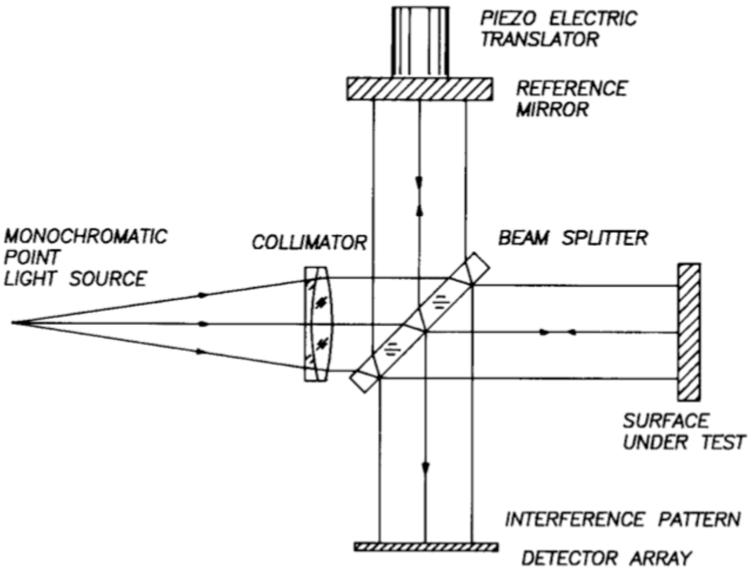

Figure 1.5: Twyman green interferometer adapted to do phase shifting. A degree of freedom is introduced by changing the reference mirror position. [13]

with the height of the reference mirror h [13] as following.

$$I = \frac{1}{2}\, I_0 \left(1 + \cos \frac{4\,\pi\,h}{\lambda}\right). \tag{1.6}$$

The signal intensity variation measured from each pixel allow us to calculate the phase modulo 2π. Each phase is related to a relative height of the surface by the relation [13]

$$h = \frac{\Delta\phi\,\lambda}{4\,\pi}. \tag{1.7}$$

The previous approach needs a white light source with chromatic filter. The concept of phase shifting can be extended using a polychromatic sources. The recorded signal intensity, proportional to the irradiance I, is the sum of all the irradiance for each wavelength, hence [13],

$$I = \int_{\lambda_{min}}^{\lambda_{max}} I(\lambda) \left[1 + K(\lambda) \cos\left(\phi(\lambda) + \frac{2\,\pi\,h}{\lambda}\right)\right] d\lambda. \tag{1.8}$$

where $K(\lambda)$ is the spatial coherence function of the source. For each point, the phase shift function of the wavelength is [13]

$$\phi(\lambda) = h\frac{4\,\pi}{\lambda}. \tag{1.9}$$

By determining the phase shift for each wavelength relative height can be calculated. Generally the phase shift is calculated using a Fourier transform of the interferograms followed by the application of the least mean squares technique to determine the relative height from the phase gradient [16]. A more recent approach is based upon a cross-correlation technique of the signal with a synthetic Gaussian curve in order to extract the envelop of the interferometric signal [17]. To conclude, the measurement is achieved by moving the reference mirror and recording the interference pattern for each step [16]. 40 to 1,000 frames are recorded depending on the depth of the surface to measure [16]. Using this technique, the range of measurement can reach 0.1 mm and a resolution of 1 nm [14]. For the measurement of parts such as spheres, measurement uncertainty of a few parts in 10,000 can be achieved [14]. The key factor is the repeatability. The repeatability mainly depends on the speed of recording. The stability can reach 0.3 nm with reduced number of frames recorded in order to reduce the measurement time [14]. The phase shifting technique is a dynamic technique. Phenomena faster than the recording time cannot be observed. In addition this technique requires a reflective surface on a stabilised table. This technique is adapted to soft surfaces with Ra below 0.2 μm [14]. Practically, the phase shifting technique is adapted to polished surfaces such as mirrors, optical surfaces, bearings, and the end of an optical fibre, or for surfaces which cannot be measured using a stylus[14].

1.3.2 Confocal based instrument

The confocal microscope was introduced by Minsky in 1961 [18]. This concept is widely used in biology, however, the concept can also be used for surface metrology.

Confocal microscopy is a scanning technique. It is based on depth discrimination due to light reflected off the measured surface passing through a pinhole [18] as shown in Figure 1.6 [13]. A point source is focused by an objective onto the surface. The

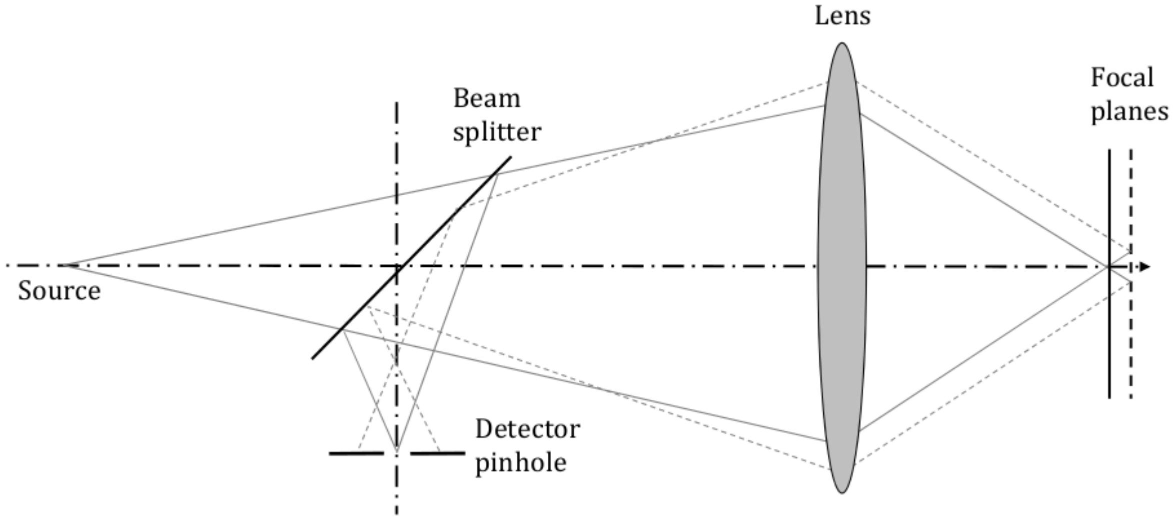

Figure 1.6: Diagrammatic representation of the depth discrimination property of confocal microscope. Only the rays focused onto the surface by the lens can be efficiently coupled through the pinhole detector [13, p 17.41].

reflected light is directed along the measurement arm by the beam splitter. The important parameter in a confocal setup is the depth of field of the lens defined by [19]

$$I(z) = I_0 \left\{ \frac{\sin[k\, z(1-\cos(\alpha)]}{k\, z(1-\cos(\alpha)} \right\}^2 , \tag{1.10}$$

where $k = \frac{2\pi}{\lambda}$, z is the axial distance, and α is the angle between the ray from the pupil plane to the focal point and the axis. The principle is to use a pinhole of the size of the Airy disk [20] of the optical system to evaluate the surface position as shown in Figure 1.6. A photo detector is placed on the back of the pinhole. The signal intensity measured by the photo detector is maximum if the surface is at the focus of the objective lens. A possible way of measuring the surface height is to move the position of the focusing lens with a piezo electric transducer. Through using synchronous detection, the height of the surface can be determined. The range of measurement can reach few millimetres. The range is limited by the maximal displacement of the detection lens. The simplest systems have no motion on the detection lens, so the range is linked to the depth of field of the objective lens; a typical value being 1 to 5 μm [21]. The lateral resolution is the one key virtue of a confocal microscope and can reach 0.3 μm for a diffraction-limited system using a short wavelength [21]. This value corresponds to the first zero of the square of the Airy function. The lateral irradiance for a diffraction limited system can be described as [19]

$$I(r) = I_0. \left[2 \frac{J_1\left(2\pi\, r\, \frac{R}{\lambda\, f}\right)}{2\pi\, r\, \frac{R}{\lambda\, f}} \right]^2 . \tag{1.11}$$

J_1 is the 1^{st} order Bessel function of the 1^{st} kind [22], r is the radial coordinate, M the magnification of the system, R is the radius of the lens aperture, and f the focal length of the objective.

1.4 High precision non-contact surface metrology; a vital technology for Taylor Hobson Ltd.

The current high precision surface metrology industry landscape has been described. It is now necessary to evaluate the strategic position of Taylor Hobson Ltd. within this landscape. In order to define the most appropriate strategic decision for Taylor Hobson Ltd., the strategic process model [23] will be used. The first step is to identify the strategic profile of Taylor Hobson Ltd. Then, the macro, internal and competitive environment will be analysed. This will then allow the Strength, Weakness, Opportunity, and Threat (SWOT) profile of Taylor Hobson Ltd. to be assessed. Then, according to this results, the generic and variation strategy will be developed. Finally, the implementation of the strategic choices will be discussed.

1.4.1 Macro, internal and competitive environment

From the 1^{st} day onward Taylor Hobson Ltd. applied a company strategy of an “analyser”[24, 1]. Therefore, in order for Taylor Hobson Ltd. to sustain technology leadership in the high precision dimensional metrology industry, Taylor Hobson Ltd. must stay in the front end of research.

The European Union is currently involved in the growth of photonics as it has been identified as a Key Enabling Technology for the future [25]. In addition, with the growing demand for high precision lenses for mass market applications such as mobile phone camera lenses, personal camera lenses, the optic market is full of new sales opportunities. In fact, Taylor Hobson Ltd. has already distribution channels and experience in the optics market. Therefore, Taylor Hobson Ltd. can aspire to increase its market share.

As shown in Figure 1.7 [26, 27, 28] the current technologies such as AFM, contact and optical technologies cover a wide range of distinct applications.

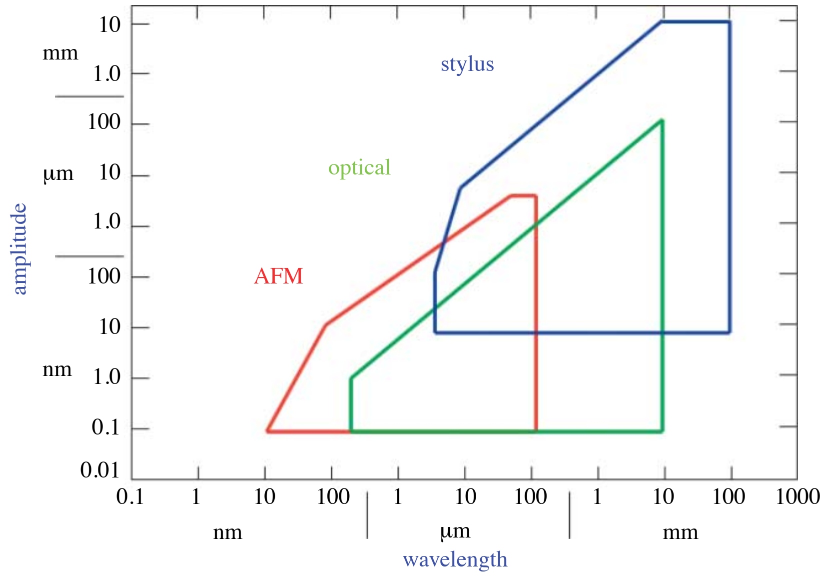

Figure 1.7: Example of typical measurable part amplitude vs spacial wavelength plots for AFM, optical and contact stylus instruments. The three method overlap in some area. In general each of these three technology family have distinct application area. [26, 27, 28]

On one hand, contact dimensional metrology instruments are covering a wider range of application due to low surface interaction with the stylus. On the other hand, non-contact dimensional metrology allows extremely high precision measurement but is restricted by fundamental limits such as the surface roughness or Numerical Aperture (NA).

Taylor Hobson Ltd. is currently supplying four instruments families:

- Talyrond; high precision roundness instruments using inductive gauges.
- Form talysurf; high precision roughness and form measurement instrument

using both PGI and LVDT gauges.

- PGI dimension; 3D high precision surface measurement instrument for high precision optics using the PGI gauges.
- CCI; white light interferometer.

Using the Product Life Cycle (PLC) model [29] shown in Figure 1.8, the place of Taylor Hobson Ltd. products portfolio is described in Table 1.1. The PLC model is based on the assumption that every product sales over time is following a generic profile. At the product introduction sales volume are low as potential new customers need to be convinced of the advantages of a new product compared to the current one. If the market is reacting, the sales grow until limited by competitive turbulence. After the competitive turbulence only a few products are still profitable. Then, the sales volume are constant during the maturity stage. Eventually, if no additional features are added to the product to maintain its product differentiation, sales decrease and the product enters declining phase. As mentioned previously, Taylor Hobson Ltd. is having an analyser strategic profile [24]. Hence, in order to keep a strategic consistency, the product portfolio must consist of products mainly in the growth phase.

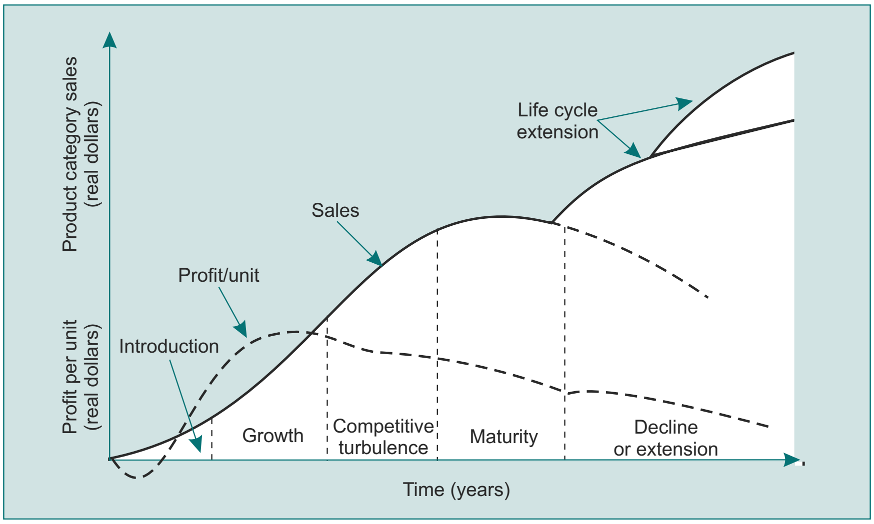

Figure 1.8: Typical PLC. Each product is following five distinct phases: The introduction, growth, competitive turbulence, maturity, and decline. The PLC can be extended by increasing the differentiation of a product. [30]

It appears from Table 1.1 that the product portfolio of Taylor Hobson Ltd. is mainly in the mature stage. If nothing is changed, the sales volume will decrease soon for the Talyrond and the Form Talysurf. In addition the CCI is entering the period of competitive turbulence, therefore it is uncertain if, or when, it will enter its maturity stage. Finally, the PGI Dimension is currently in growth stage. However, the PLC of the PGI Dimension is only estimated to be a few years.

Table 1.1: Taylor Hobson Ltd. product families PLC and portfolio analysis.

Product	Place in the PLCe	BCG Matrix product type
Talyrond	Extension	Cash cow
Form Talysurf	Mature/Decline	Cash cow
PGI Dimension	Growth	Star/Cash cow
CCI	Introduction/growth	Question Mark

Using the Boston Consulting Group (BCG) matrix shown in Figure 1.9 [31, 32], it appears as shown in Table 1.1 that Taylor Hobson Ltd. product portfolio consists mainly of late ”Cash Cow” and late ”Star”. The position of the CCI is uncertain.

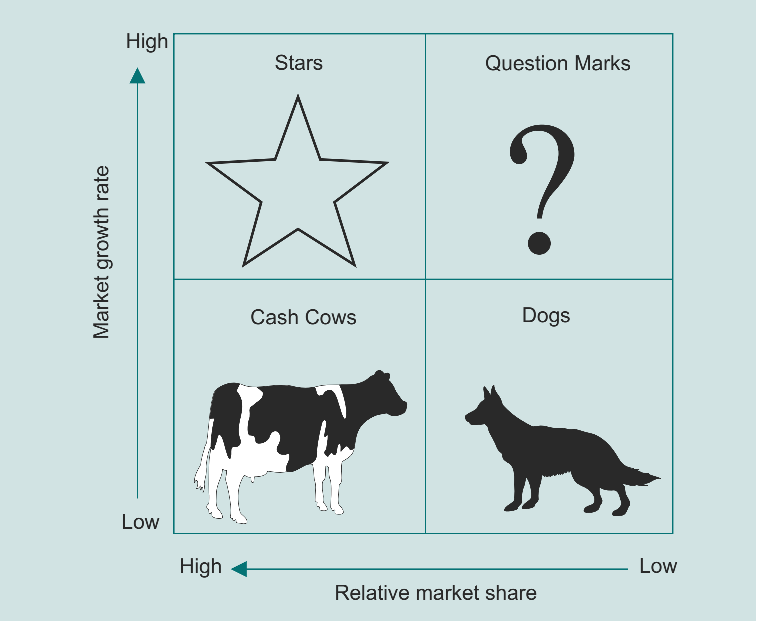

Figure 1.9: BCG Matrix representation, assuming an economy of scale, each product can be categories as a ”Dog”, ”Star”, ”Question Mark”, and ”Cash Cow” function of their position in the market share versus market growth matrix. [31, 32]

The CCI might evolve as a ”Star” or as a ”Dog”. If the CCI evolve as a ”Dog” it will have to be divested if not profitable. The generic BCG model state that the

R&D expenditure should be low for a "Dog" and a "Cash Cow" products but high for a "Star" and "Question Mark" products in order to increase or maintain the market share throughout a unique competitive advantage. The R&D expenditure of the "Star" and "Question Mark" are financed using the revenue of the "Cash Cow". It has to be pointed that the BCG model assumes that the products follow an economy of scale [31]. This argument can be argued, nevertheless, the high precision dimensional metrology industry is to a large extent following the economy of scale.

The macro and internal environments are now understood. The next step is to analyse the competitive environment using the Porter's five forces model as illustrated in Figure 1.10 [33].

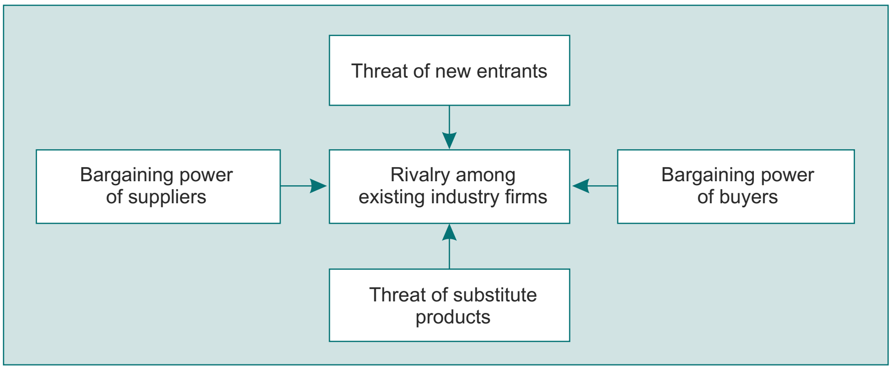

Figure 1.10: Illustration of the Porter's 5 competitive forces. [33]

The high precision dimensional metrology industry is an oligopoly [34] with only a few key players such as Mahr [35] and Panasonic [36] in the contact high precision dimensional metrology industry with probes and Zygo [36] in the non-contact high precision dimensional metrology industry. Each of these key players have high market share especially in certain geographic are such as Asia for Panasonic and Germany for Mahr. Nevertheless, the number on new small companies and university spin-off such as Sensofar [37] and Luphos [38] is rapidly increasing. In fact, the entry barriers are falling due to company such as Aerotech [39] supplying state of the art surface metrology measurement platforms. The entry barrier of the surface metrology measurement platform is now significantly reduced. Therefore, the threat of substitute technology is continuously increasing.

Nevertheless, the value chain [40] of such companies is restricted compared to the already established ones. This restriction limits the market share of these small companies. However, their limited value chain [41] reduced their overhead and gives them a cost leadership advantage. In addition, because the market is evolving from an oligopoly to a perfect competition industry structure, the bargaining power of the buyer is increasing. The competitive profile of Taylor Hobson Ltd. is summarized in Table 1.2.

Table 1.2: Taylor Hobson Ltd. competitive profile using the Porter's 5 forces model.

Competitive force	Current Force	Expected Force
Rivalry among existing industry firms	High	High
Threat of new entrants	Medium	High
Threat of substitute	Low	High
Bargaining power of buyers	Medium	High
Bargaining power of supplier	Low	Low

It has to be noted that corporate finance has not been covered in this analysis for reason of simplicity.

1.4.2 Generic and variation strategy

The macro, internal and competitive environment of Taylor Hobson Ltd. having discussed the previous results, can be summarized in a SWOT analysis.

Strength

- Strong brand.
- Established distribution channels.
- Multiple "Cash cow" products.
- Potential "Star" product.
- Experienced in R&D.
- Large distribution network.
- Strong value chain.

- Additional financial and human resources in the other companies of the Ametek Ultra Precision Technology (UPT) division [42].

Weakness

- Only one "Question Mark" product to be turned into "Star" or "Cash cow".
- Sales force are more "comfortable" with contact surface metrology.
- Large overhead.
- Limited human resources in R&D

Opportunity

- Growing market in the photonic industry.
- More optical technologies are becoming cheaper.
- New optical sensing technologies.

Threat

- Growing threat of new entrance.
- Growing threat of substitute.
- Lower entrance barrier.
- Lower product differentiation due to larger competition

The aim is to convert, mitigate, or suppress the threats and weaknesses using the strengths to build on the opportunities.

Due to the analyser profile of Taylor Hobson, the highly segmented market, and the strong strength of Taylor Hobson Ltd. in R&D, the generic strategy of Taylor Hobson Ltd. based on Porter's generic strategies [43] illustrated in Figure 1.11 is differentiation focus. In order to maintain the differentiation position it is necessary to increase the perceived added value of the current "Cash cow" products. Some PLC "Cash cow" might not be extendable due the high threat of new entrance and substitution, therefore it is necessary to create a new "Star" product to maintain a long term competitive advantage. The PLC extension and the new "Start" strategies can be based on the same non-contact sensing technologies. A fast, single point, high dynamic range, high NA non-contact dimensional probe would allow fast and versatile roundness and form measurement. Based on the previous analysis the strategic variations of Taylor Hobson Lts are:

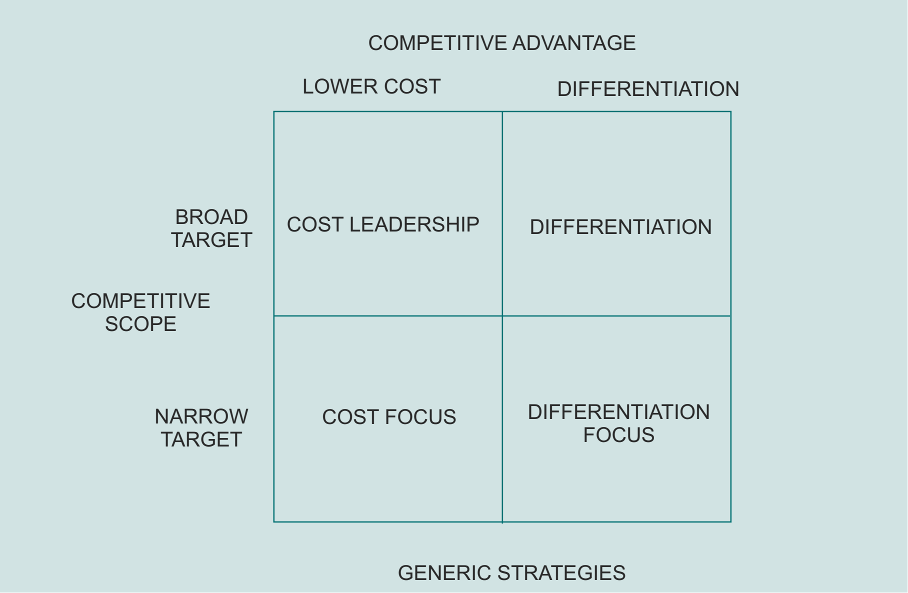

Figure 1.11: Competitive scope and advantages also called Porter Generic strategies. Following the Porter's Generic strategy model a company should pursue a cost leadership, differentiation, cost focus or differentiation focus strategy. In between strategies are not-recommended as create a loss of strategy focus. [43]

1. Acquiring an innovative non-contact distance measurement sensor to maintain the current and new product differentiation and increase the perceived added value.
2. Increasing the market entrance barrier for competitors.
3. Increasing customer retention by increasing the exit barrier.

1.4.3 Implementation of the strategy and thesis goals

The strategy variations have been identified in the previous section. First, the acquisition of an innovative non-contact distance measurement sensor can be achieved through R&D or by acquisition of a company. Company acquisition has been investigated but will not be discussed in this thesis. Because the Taylor

Hobson Ltd. sister companies Solartron Ltd. [44] and Precitech Inc. [45] share similar strategic interests, the innovative non-contact distance measurement sensor can be designed as a joint venture. Second, the market entrance barrier can be increased by patenting new technologies. Finally, customer retention can be achieved by increasing the Plan, Do, Check, and Act (PDCA) cycle integration of the products using joint ventures with companies such has Precitech Inc. and patents.

Because all of these tasks are a long term, high risk research, it is appropriate to allocate them to a research engineer under an Engineering Doctorate program. In fact, the Engineering Doctorate program permit to mitigate the long term associated risk thanks to the low capital involvement of this program as well as reducing the research risk due to involvement of a university. Therefore the goals of the Engineering Doctorates are:

- Develop an innovative non-contact distance measurement sensor for Solartron Ltd.
- Develop an innovative non-contact distance measurement sensor for Precitech Inc. for in line SPDT metrology.
- Develop the most precise industrial non-contact distance measurement sensor for Taylor Hobson Ltd. for three dimensional surface topography and roundness measurement.
- Increase the market entrance barrier to competitors with at least one patent on the technology.
- Increase the exit barrier by improving the Taylor Hobson Ltd. product integration into the PDCA cycle.

1.5 Discussion

The optical manufacturing industry needs a versatile non-contact dimensional metrology instrument enabling 3D surface topography measurement of lenses exhibiting a clear aperture of more than 70 mm. The measurement repeatability must be below 100 nm and the measurement cycle in the order of a few minutes maximum.

Today, neither contact nor non-contact dimensional metrology instruments offers such performances. Section 1.4 highlighted the need for Taylor Hobson Ltd. to include such a technology to its product portfolio.

In addition, Solartron Metrology Ltd. and Precitech Inc., both part of the Ametek UPT division together with Taylor Hobson Ltd., share a similar need respectively for an entry level versatile non-contact distance measurement gauge and in-line measurement of part machined using SPDT. There are several barriers which needs to be climbed to engineer an industrial 3D dimensional measurement system. One of the major barrier is the development of the gauging technology. Several technologies are potentially viable but need to be improved.

This thesis addresses the challenges related to the development of gauging technology suitable for non-contact dimensional measurement of mechanical parts from car wind-shield to diamond turned germanium lenses for Infra Red (IR) imaging while protecting the Ametek UPT division from competition.

1.6 Thesis outline

In order to achieve the previously detailed goals, the suitable technologies for high speed non-contact gauging will be investigated in the Chapter 2. It will be argued why the CCM is the most suitable technology for high speed, high resolution non-contact surface topography. This technology will be benchmarked against the three major alternative technologies; spectral chromatic confocal microscopy [46], multi-wavelength interferometry [47], and the dispersed reference interferometry [48].

Chapter 3 describes analytically and practically the design of a CCM using a systemic approach. Novel spectral irradiance and measurement standard deviation models are developed. Furthermore, this chapter details the optical design of the CCM head. Refractive, diffractive and hybrid aspheric diffractive structure are investigated and their performance compared. In addition, the concept of broadband diffractive optics are studied [49]. Using an analytical model, it is shown that the manufacturability of such element is limiting their capability how the manufacturing boundary can be extended by using Step Diffractive Surface (SDS). Finally the implementation of such lenses into an optical ray tracing software is discussed. By applying those models, a low cost and high resolution version CCM respectively for Solartron Ltd. and Precitech Inc has been developed. For all the sub-system, the viable technologies are investigated. It is then shown how the trade-offs are performed to reach the desired performances.

In chapter 4 the performances of the previously designed system are evaluated. In addition, the impact of the measurement environment is modelled, measured, and corrected when possible. The studied environmental factors are the temperature stability, surface slope, roughness and reflectivity. It is shown that careful system design, calibration, and data processing permit the mitigation of all the previously cited errors.

Finally, Chapter 5 presents the conclusions reached for the body of work and proposes future work in this area.

Chapter 2

Gauging technologies for high precision dimensional metrology

Two approaches have to be distinguished in the field of high precision dimensional metrology instruments; the laboratory instrument and the industrial instrument.

The former approach is usually achieved by using the Abbé measurement principle [50] for a one off instrument. The instrument will be used in a laboratory environment with a controlled temperature, airborne particle concentration, and humidity. The purpose is to create one or a few instruments to offer a metrology service for measurement and calibration. The Return On Investment (ROI) is calculated as

$$\text{ROI} = \frac{\text{Investment benefit}}{\text{Cost of investment}} \tag{2.1}$$

In the former approach, the "Investment benefit" is the revenue generated by the measurement service . The "Cost of investment" is the cost of the development and production of the measurement platform. Hence, the production of the platform is a one-off investment.

In the later approach, the instrument which is sold as a measurement solution will be used in an industrial environment. The instrument will be used in versatile environments with dirt, temperature fluctuation and non-specialist operators. The "Investment benefit" is the revenue generated by the sale of all the instruments and the "Cost of investment" is the instrument's cost to develop. Hence, the cost of production of each instrument reduces the “Investment benefit” while “Cost of Investment” is not increased. Therefore in this case, the ROI is more sensitive to the cost of production of the instrument.

In our case, Taylor Hobson Ltd is looking to develop an industrial dimensional metrology solution. Therefore, even if some solutions are superior in performance, the incremental cost of production will reduce the ROI. Taylor Hobson Ltd is looking for the solution maximising the ROI for the market of high precision dimensional metrology instruments and not in providing a high precision dimensional metrology service.

2.1 High precision dimensional measurement sensor technological landscape.

In order to identify the most suitable technology, industrial and academic research have been undertaken. The following technologies have been identified as suitable.

1. Low-coherence interferometry [51].
2. Short coherence fiber probe interferometer [52].
3. Fiber-based white-light interferometer [53, 54].
4. Normal vector tracing method [55].
5. Multi-wavelength interferometer [56, 47].
6. Dispersed reference interferometer [48].
7. Chromatic confocal microscope [57].
8. Spectral chromatic confocal microscope [46].

The technologies 1 to 3 are protected through patents and are commercialised by competitors of Taylor Hobson Ltd. Hence, this technology are not suitable. The technologies 4 to 8 will be described. Their potential and limitations will be discussed in order to identify the most appropriate one.

2.1.1 Normal vector tracing method

The Normal Vector Tracing Method (NVTM) is a unique method to measure high precision polished surfaces. The basic concept is to measure the angles of the normal vector to the surface in a spherical coordinate system. The angle is measured by finding the part position where the incident collimated beam is normal to the surface as shown in Figure 2.1 [55]. Thus, the reflected beam coincides with the incident beam when the normal vector to the surface is collinear with the incident laser beam. Matsumura . implemented such a system [55]. The main source of uncertainty is the measurement uncertainty of the angle θ, ϕ, α, β, and the distance L. They achieved a resolution of 1 nm Peak to Valley (P2V). The measurement cycle time is unknown. Such a system does not have any limitation in surface slope or maximum heigh apart from those of the goniometers. This means that the system is particularly suitable to measure free-form surfaces or aspheric lenses.

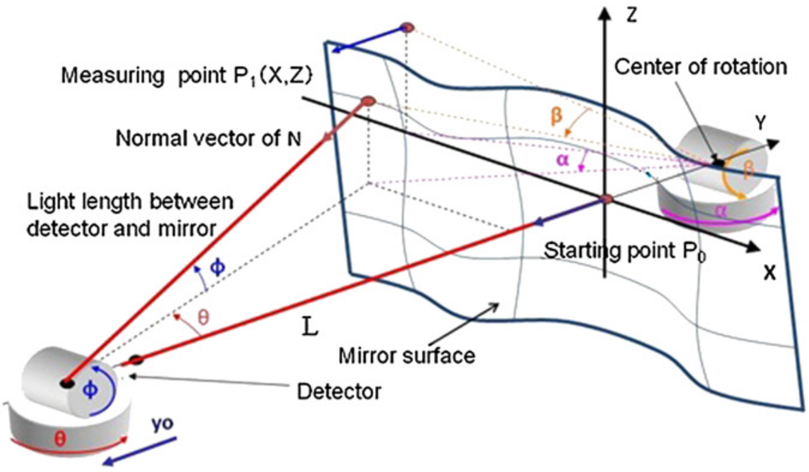

Figure 2.1: NVTM principal. The angle θ, ϕ, α, and β are tuned to have the incident and reflected beam having the same angle. [55]

The major limitation of the system is the assumption made on the surface under the size of the laser spot. The beam has the be Gaussian in order for the quadrant detector to assess the normal vector to the surface [55]. However, due to long distance involved in the measurement, the laser beam divergence must be low, which induces a large beam waist [58]. In a personal interview with H. Matsumara, he revealed that the laser spot on the surface can be as large as 500 μm. The latter point underpins that any light surface interaction within the spot size will degenerate the laser spot Gaussian intensity profile. The surface under the spot size is assumed to be a perfect flat mirror. Otherwise, the measurement error is increasing. Therefore, only polished surfaces with no discontinuity or significant profile variation within the spot size can be measured precisely.

Regardless of the latter limitation, the simplicity of the method enables highly accurate and repeatable measurements on selected parts. The main constraints are the limited part type which can be measured and the requirement for a temperature controlled environment. Therefore, the NVTM is particularly suitable as a reference measurement method for non-contact free-form metrology.

2.1.2 Multi-wavelength interferometer

In a case of a single wavelength interferometer, absolute position is achieved by fringe counting. Therefore, a static measurement has an unambiguous range of $\lambda/2$. Using such a method, the position can be assessed with a sub-wavelength accuracy by interpolation of the interference intensity within the unambiguous range. However, if one period is lost, the measurement is shifted. In addition, only relative distance measurement is possible.

In the case of the Multi-wavelength interferometer (MWLI), the position is assessed by measuring the beat frequencies of multiple coherent sources in order to assess the fringe count and the single wavelength interference intensity in order to assess the sub-wavelength resolution as shown in Figure 2.2. Hence, using such a method fringes-counting is not necessary within the beat frequency of the synthetic wavelength Λ [59].

The beat frequency is generated by combining several waves of different wavelength. In the case of a two wavelength λ_1 and λ_2 system, the synthetic wavelength Λ is equal to [47].

$$\Lambda = \left| \frac{\lambda_1 \, \lambda_2}{\lambda_2 - \lambda_1} \right|, \tag{2.2}$$

with the unambiguous range being $\Lambda/2$.

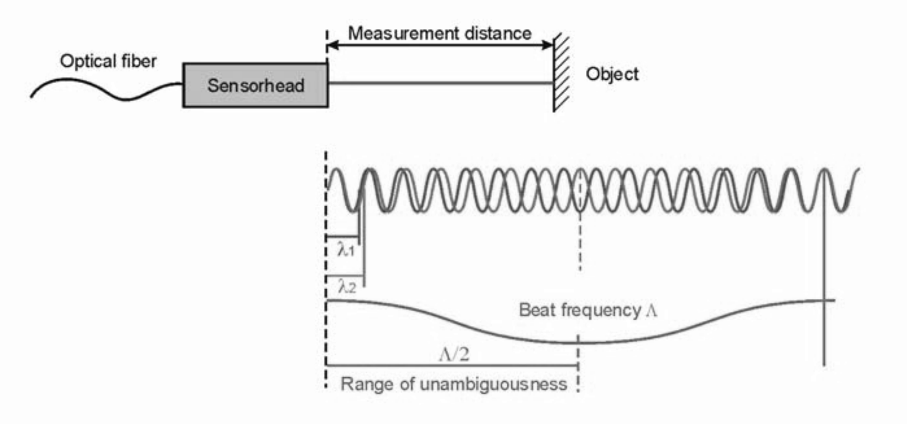

Figure 2.2: MWLI concept. The two wavelengths λ_1 and λ_2 are generating the beat frequency Λ. Hence, the ambiguity length is enlarged to $\Lambda/2$ allowing long measurement range with no requirement for fringe counting. [56, 47]

Hence, the synthetic wavelength Λ is inversely proportional to the difference of the two wavelength injected. In addition, if three independent wavelength are used, three independent speckle patterns are generated. Therefore the true position can be partially decoupled from the speckle noise [47]. The beat frequency position measurement permits the position count to be assessed within the unambiguous range $\Lambda/2$.

The phase value is obtained by shifting through time the position of the optical head relative to the measured surface using a piezo-electric actuator [56]. The measurement uncertainty, for an interval of confidence of 95 %, is 1 nm at a measurement rate of 2 kHz over a measurement range of 300 μm. Hence, the Dynamic Range (DNR) is 300,000. The measurement rate is limited by the need of phase shifting.

Because the multi-wavelength approach is an interferometric method, the measurement is not related to the spatial intensity distribution of the light. Therefore, in order to achieve a measurement spot size of a few tens of μm over a measurement distance of a few mm, the NA must be low. In fact, the optical from Luphos exhibiting a measurement range of 3 mm is having an NA of 0.03. Using a Cordinate Measurement Machine (CMM) with 3 axis of freedom and a following mode axis can measure an object with up to 5 degrees of freedom, α, β, x, y, and z in a cartesian coordinate system where α, β, γ are the Euler angles. However, free-form parts have 6 degrees of freedom α, β, γ, x, y, and z. One of the major issue of this technology is that Luphos Gmbh. is currently holding a patent [56] on the technology restricting the freedom to operate.

2.1.3 Dispersed reference interferometer

The Dispersed Reference Interferometer (DRI) can be modelled as a Michelson interferometer where the reference arm is chromatically dispersed, as shown in Figure 2.3. Hence, the optical path is a function of the wavelength and can be described as [48]

$$\delta(k) = \frac{l}{\sqrt{1 - \left(\frac{2\pi}{k\,D}\right)^2}}, \tag{2.3}$$

where l is the separation between of the gratings G1 and G2 and D the grating period.

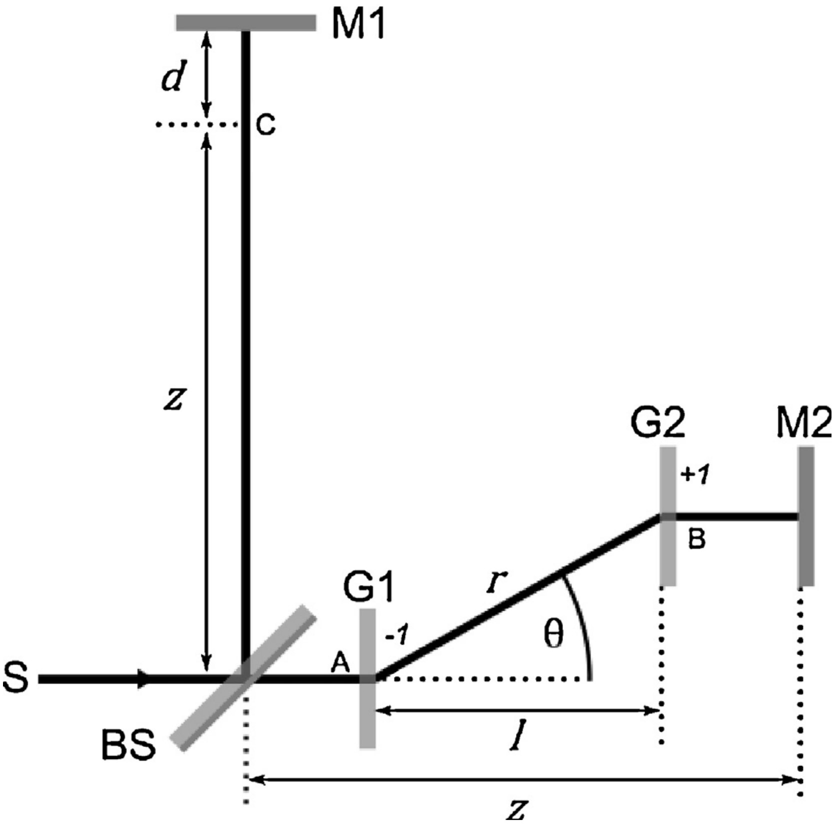

Figure 2.3: Schematic of the DRI. The distance d is measured by recording the interferometric signal chromatically modulated in the reference arm by the grating G1 and G2. [48]

In such a system, the length d in Figure 2.3 is coded with a chromatic interference pattern. At the centre of the coherence length, the chromatic interference pattern is as shown in Figure 2.4

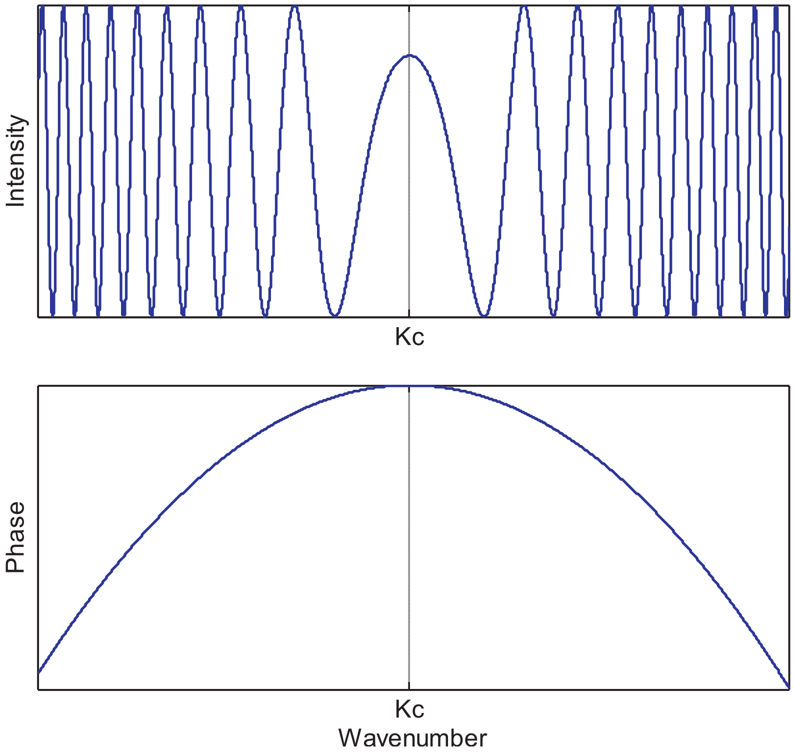

Figure 2.4: Interferometer output intensity (top) and corresponding phase difference (bottom) function of k [48].

If the mirror M1 is shifted from the centre of the coherence length, the interferometer output intensity shown in Figure 2.4 will be de-centered compared to the centre wave number of the source. Hence, each position of the mirror M1 is having a unique interferometer output intensity.

H. Martin and X. Jiang implemented such a system in Reference [48]. The position is assessed by measuring the peak position of the auto-convolution of the interferometer output. The achieved measurement range is 100 μm. An interview with H. Martin revealed that they achieved a DNR of 30,000 at a sampling frequency of 20 Hz. Nevertheless, the resolution is not constant over the range of measurement. In fact, the interference pattern shown in Figure 2.4 is shifted to the side on the edge of the measurement range. This lead to less information in the interference pattern and therefore a loss of resolution.

The dispersed reference interferometer is estimated to be at a Technology Readiness Level (TRL) [60] 3 and therefore it will take a lot of time to achieve a practical industrial application.

The system can be improved by reducing the light losses in order to increase the sampling rate. However, the data processing speed will soon limit the sampling rate of the system. Nevertheless, technology trend shows a constant increase in computation power. Therefore, the dispersed reference interferometer application range is limited but future development should increase the spectrum of application.

2.1.4 Chromatic confocal microscope

The basis of the CCM is the chromatic coding if the measured axis [57]. A broadband source is focused onto the surface using a hyper-chromatic lens so that each wavelength is focused at a unique position as shown in Figure 2.6. By analysing the reflected light spectrum as shown in Figure 2.5 the surface position can be measured.

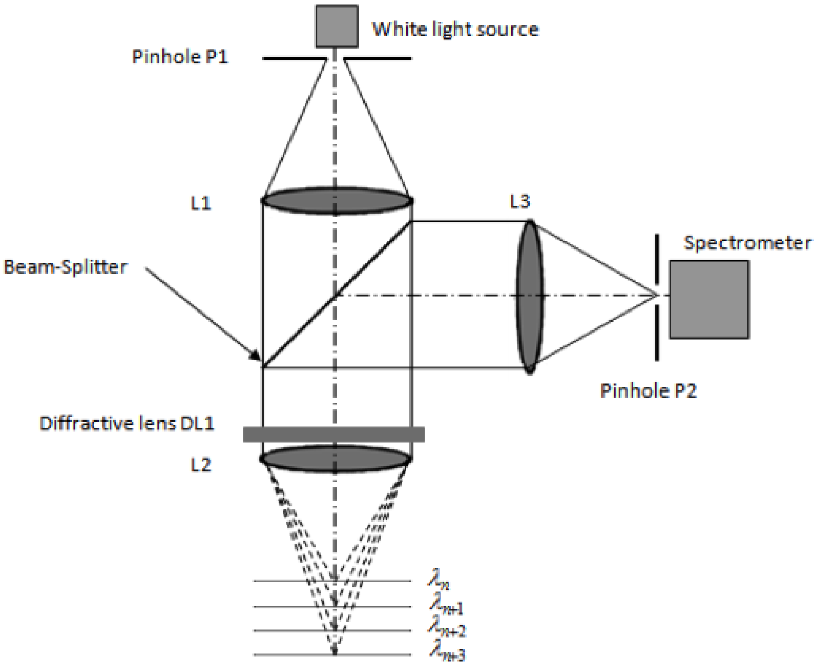

Figure 2.5: Chromatic confocal microscope principal. A broadband source is focused onto the surface using a hyper-chromatic lens. Hence, each wavelength is focused at a unique position. By analysing the spectrum of the reflected light, the position of the surface can be measured.

The CCM has been commercially available for several years by companies such

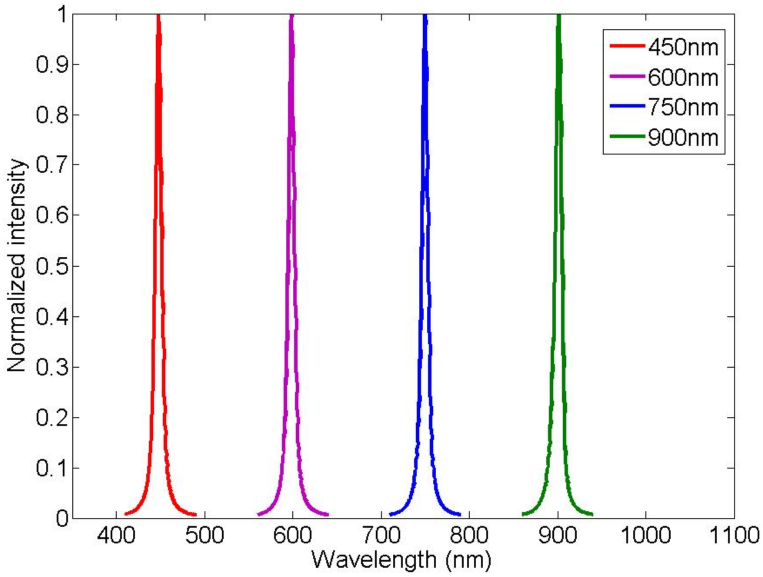

Figure 2.6: Chromatic confocal microscope peak response at several wavelength. The equivalent spatial position on the measurement axis varies as a function of the dispersion function of the hyper-chromatic head [61].

as Stil SA. [62], Precitec Gmbh. [63] and Nanovea Inc. [64]. One of the leading manufacturer, Micro-Epsilon Gmbh. supplies a CCM with a maximum surface slope of 34°, a range of measurement of 300 μm and a resolution of 10 nm [65] which creates a dynamic range of such system of 30,000 at 2 Hz.

It has to be pointed out that even if the maximum slope is specified to be 34°, the measurement uncertainty is increasing significantly when the surface angle is increasing. No literature has been found on the subject, nevertheless CCM manufacturer disclosed an surface slope error of 0.1 % of the range of measurement.

Most of the commercial CCM use refractive lenses [66, 67]. Dispersive lenses are more simple to design using classical ray tracing optical design. In addition, the manufacturing of dispersive lenses is repeatable by using conventional technologies.

Gradient Index (GRIN) lenses are used for compact systems [68]. However, the focal length of GRIN lenses are more temperature sensitive than for refractive lenses and therefore need a temperature compensation of the measurement [68]. For high precision applications, refractive lenses are the current standard.

Another approach is to use diffractive lenses [69, 70, 71, 72, 73]. By using a single diffractive lens manufactured using multi-level beam etching assembled with a classical microscope objective, a nearly diffraction limited CCM objective head with only off-the-shelf components is build[69]. This approach is not suitable for industrial applications due to the high cost of the head in volume production as well as the limited range of measurement [69, 73] and short working distance of the microscope objective. Even with the current limitations of diffractive lenses, the chromatic aberration of diffractive lenses exceeds those of a refractive lens [74]. Despite this advantage, manufacture and volume production is currently limiting the industrial applications of the CCM using diffractive lenses.

The combination of various scanning techniques to CCM measurement represents a significant advance; inspired by classical confocal microscope scanning techniques, CCM single point measurement has been extended to become Chromatic Confocal Spectral Microscope (CCSM). Two major categories of CCSM have been developed; addressing the position of the spot and parallel measurement.

Addressing the position of the spot onto the surface can be realised in various ways, such as:

1. Acousto optic deflector [75].
2. Digital mirror devices [76].
3. Rotating mirror [77].
4. Nipkow disk [66].

In techniques 1 and 2, the beam is deflected electronically. Hence, no mechanical motion is introduced and the system is vibration-free. In techniques 2 and 3, a Nipkow disk or a spinning mirror addresses the position of the spot. Hence, these systems need to be engineered carefully to not introduce vibrations. Using this method an area of 320x240 pixels can be scanned at a rate of 3 Hz [69].

Parallel measurement has been implemented experimentally using the following two approaches:

- A bundle fibre in which each core acts as a point source [62].
- A colour camera [67].
- Spectral multiplexing [78].

In the first method, instead of deflecting the beam, the confocality of each core allows the parallel measurement of several points. In the second method, a colour camera has been used to analyse the reflected wavelength. By recording a colour picture, using 3 filters, the peak wavelength is interpolated. This method can be regarded as a 3 pixels spectrometer. The resolution is significantly deteriorated. The last method split the spectrum of the light source by using the diffraction efficiency of multiple diffraction mode. Each part of the spectrum is then focused at various lateral positions.

There is substantial CCM knowledge in the public domain. The basic concept was established by Molesini in 1984 [57]. Various patents are in application but none significantly restricts the freedom to operate [79, 80, 81, 82, 83].

2.1.5 Chromatic confocal spectral microscope

An extension of the CCM is the CCSM. For such a system, the CCM has a reference arm with a plane mirror and a measurement arm chromatically codes the measurement axis as shown Figure 2.7 [46]. Hence, the reflected light from the surface interferes with the light from the reference arm. Therefore, the confocal peak signal is modulated by a white light interference pattern as shown in Figure 2.8 [46]. Thus, this signal is an equivalent to that of a white light interferometer without the need of an axial scan. Therefore, the resolution of such a system is improved compared with the the one of CCM and faster than the one of white light interferometer. One industrial version manufactured by STIL SA [62] claims a 1 nm resolution for a range of measurement of 130 μm and a sampling rate of 2 kHz. The main limitation of the sampling rate is the data processing speed. In fact, analysing such a signal is computationally expensive. It has to be noted that if the depth discrimination of the confocal response is smaller than the coherence length of the source, the interference pattern is filtered by the confocal peak [46]. The latter comment led to a paradox between the confocal and interference signal.

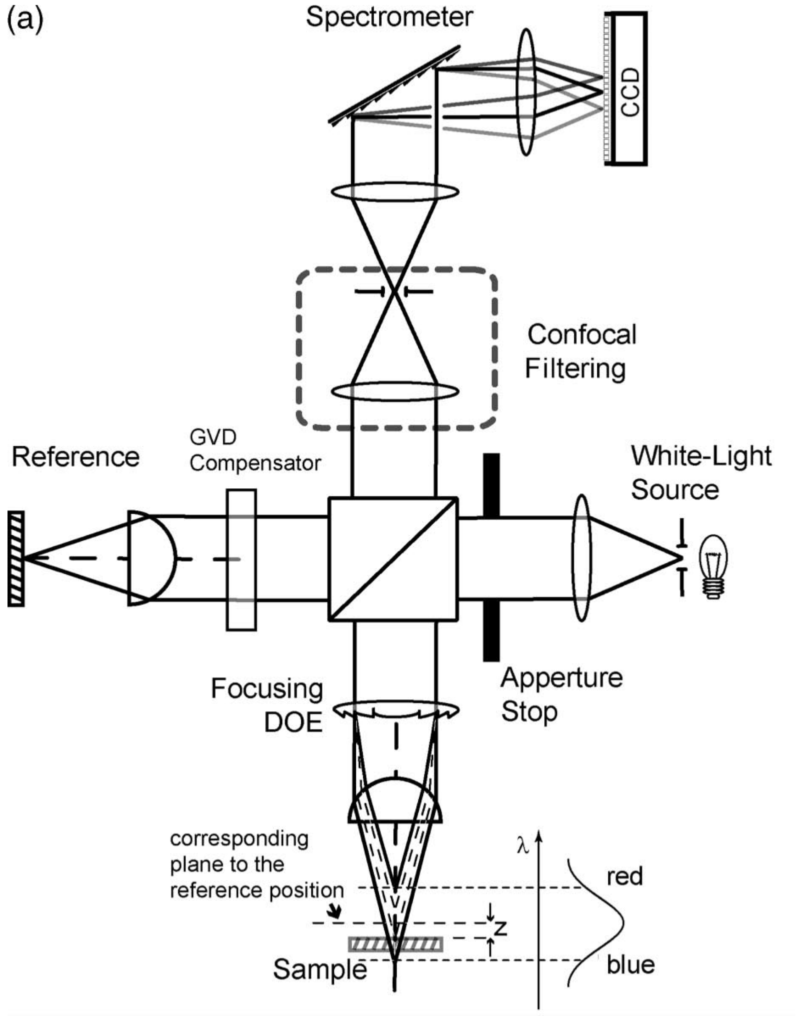

Figure 2.7: Spectral chromatic confocal microscope principal. The spectral chromatic confocal microscope is build as a CCM with an interferometric reference arm in order to modulate the peak response of the CCM [46].

Even though this method is supposed to have a higher dynamic range than the CCM, the viability of the method is yet to be shown in industrial application. In fact, due to the use of a reference arm, the optical path difference between the reference and the measurement arm has to be within the coherence length of the source. Because the CCM uses an incoherent source, the coherence length is short. Therefore, the implementation of an optical fibre based system would be difficult. Hence, the measurement cannot be performed remotely from the spectrometer and the sources. This implies that the full system has to be near the sample. Engineering

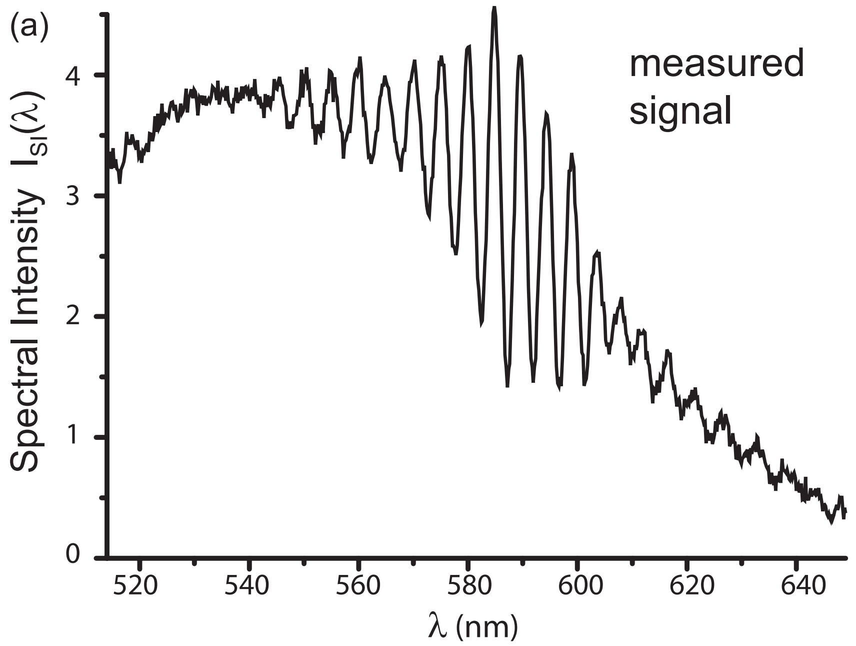

Figure 2.8: The signal of the spectral chromatic confocal microscope is superposition of the confocal signal, the interferometric pattern of the equivalent white light interferometer, and the optical spectrum if the source. [46]

such a system is complicated and expensive as it involves translation stage capable of carrying heavy load.

In conclusion, despite clear advantages compared to a white light interferometer or a CCM this technology is limited in its application range. The non-viability of remote single point measurement makes this technology less suitable for scanning 3D measurement than the CCM. In addition, since the CCSM is already coded in the spectral domain, one-shot 3D scan is not practical on a CCD array as it would involve multiplexing the signal on at least one axis. Therefore, the measurement speed advantage of the CCSM compared to a white light interferometer is not relevant.

2.2 Why is the chromatic confocal microscope an attractive technology for the surface metrology industry?

Various technologies have been identified and investigated to evaluate their suitability as a non-contact substitute to the PGI and inductive gauge respectively for high precision surface and roundness dimensional metrology.

Table 2.1 demonstrates that the MWLI uses is limited by Intellectual Property (IP) from various sources. In addition, the factors limiting the maximum sampling rate are not described in the literature but limits the application spectrum. Even if the sampling rate is increased, the strong IP protection shift the “Bargaining power of supplier” in Porter’s Five Forces profile of Taylor Hobson Ltd in Table 1.2 from “low” to “high”. Hence, the MWLI would deteriorate the risk profile of the project.

Table 2.1: Comparison of the various viable technologies for a high precision non-contact free-form dimensional metrology.

Technology	Resolution	DNR	Max. slope (°)	Sampling rate	TRL[60]	IP
MWLI	1 nm	400,000	7	2 kHz	9	Strong
DRI	3.3 nm	30,000	5	20 Hz	3	Accessible
CCM	10 nm	30,000	35	30 kHz	9	Few
CCSM	1 nm	270,000	7	2 kHz	7	Few
NVTM	1 nm	Infinite	90	unknown	7	None

The DRI is a potentially relevant technology for high precision dimensional metrology. Nevertheless, the early TRL stage of the DRI decrease significantly the viability of the DRI as a medium term solution. In fact, the DRI still has to go through “The Valley of Death” before reaching a TRL of 7. The DRI can still be developed by academics before the TRL reaches 7. Then, Taylor Hobson Ltd. could convert this technology into a product. If Taylor Hobson would decide to develop the product from the current TRL, the risk weighted ROI would not exceed the cost of the necessary capital invested by Taylor Hobson Ltd. Hence, this technology is not suitable for this project.

The CCSM is an hybrid technology having the resolution of a white light interferometer with no need of phase scanning due to the chromatic aberration of the CCM. Nevertheless, the paradox between the NA and the white light signal restricts this technology to specific applications. This technology does not match the requirement set-up in Chapter 1.

The NVTM performances are competitive compared to state of the art interferometric techniques without the need of a reference surface. In addition, the simplicity of the concept is attractive. However, this technology is incredibly sensitive to the environment. On one hand, the measurement uncertainty decreases when the length L in Figure 2.1 increases. On the other hand, the longer is the length L, the larger is the measurement deviation due to misalignment or linear thermal expansion of the measurement platform. This measurement method is limited by the stability of the measurement environment. Therefore, this measurement technique is particularly suited for a metrology laboratory but not for industrial application. In addition, due to the large laser spot, this instrument can only measure polished parts without discontinuities, neither large profile variation within the 0.5 mm radius of the laser spot. In conclusion, this measurement method is more suitable to provide reference measurement for 3D free-form.

The CCM has the advantage of being a versatile measurement method with a remote measurement head. Therefore, the system is suitable for roundness and surface dimensional measurement. In addition, the CCM is potentially a fast measurement method with a sampling rate of 30 kHz. Hence, the CCM could unleash the full potential of non-contact measurement by suppressing the stylus force and and associated vibrations at high surface speed. Hence, fast full 3D measurement could be possible. This key attributes could provide Taylor Hobson Ltd. with one technology suitable for all the product portfolios.

The CCM is currently limited by the dynamic range. Additionally, even though the measurement range is reduced, commercially available CCM systems do not have a resolution better than 5 to 10 nm. However no research has been carried out on the fundamental limits of the CCM. Using the current architecture, the dynamic range limit is defined how precisely the peak position can be determined on the linear array sensor of the spectrometer. The sources of position uncertainty are various and complex but, if understood, can be minimised.

2.3 Chromatic confocal microscopy; a promising technology

It is essential to understand the fundamental DNR limitation of the chromatic confocal microscope, in order to know how the system can be optimised. From the basic working principal of the CCM described in Section 2.1.4, it appears that the resolution is determined by the ability to determine the peak position on the line scan sensor of the spectrometer. Hence the fundamental resolution limit can be expressed in pixels. The measurement range is defined by the dispersive power of the chromatic head over the wavelength range of the source. Hence the range of measurement can be tuned easily by changing the light source spectrum or the optical head dispersion. Despite the later point, the fundamental range limit is directly related to the number of pixels used on the line scan sensor. Therefore, the fundamental dynamic range limit of the chromatic confocal is the ratio of expended noise position uncertainty over the number or pixels used and can be described as follows

$$\mathrm{DNR}_{\mathrm{limit}} = \frac{N_{\mathrm{pixel}}}{2\,\sigma^{\mathrm{pos}}}, \tag{2.4}$$

where σ^{pos} is the standard deviation of the measured position, and N_{pixel} the number of pixels used. The standard deviation is multiplied by a factor two to have an interval of confidence of around 95 % [3]. In order to estimate the limit of such a system, a Gaussian peak of FWHM of 60 pixels with a Signal to Noise Ratio (SNR) of 42 dB, which correspond to the SNR or the Dr-4k-500 Complementary Metal Oxide Semiconductor (CMOS) sensor [84], is numerically generated as shown in Figure 2.9a. The peak position is then calculated using a Blais Rioux peak detector [85]. The positions distribution is shown in Figure 2.9b.

The standard deviation is found to be 0.006 pixels. Using a standard 2048 pixels line sensor, the dynamic range with a degree of confidence of 95% would be 170,667. If the measurement range is 300 μm, the resolution is therefore 1.8 nm.

This brief computations show that currently commercialised CCM are not using the full potential of the technology.

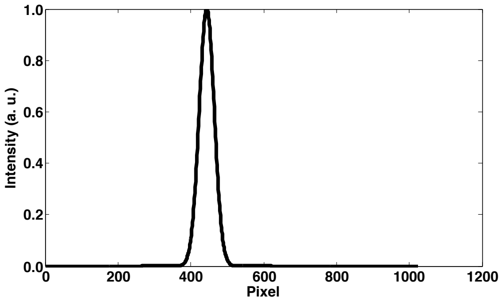

(a) Gaussian peak normalised to 1 with a standard deviation of 60 pixels and a SNR of 42dB

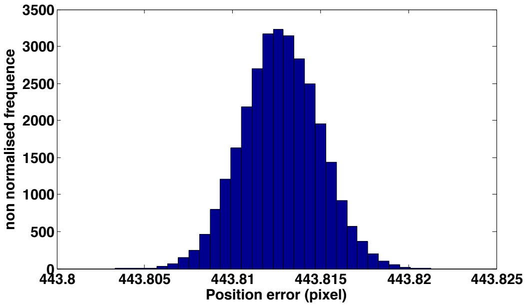

(b) Peak position distribution. It appears that the distribution is Gaussian with a standard deviation of 0.006 pixels

The measurement linearity limitations are partially described in the literature [86]. However, measurement linearity limitation factors include every internal and external variables which are different from the calibration such as

- Temperature drift.
- Calibration drift.
- Surface reflectivity.
- Surface slope.
- Surface finish

This non-exhaustive list illustrates that the source and magnitude of the errors can vary significantly. In order to bring the linearity error closer to the resolution, all the errors have to be mitigated, corrected or eliminated.

2.4 Discussion

It has been demonstrated in this chapter that the most suitable technology for Taylor Hobson Ltd. to develop further to replace the contact probes for surface and roundness dimensional metrology is the CCM. The CCM has the potential to cover a large number of markets ranging from roundness measurement at more than 20 rpm to precision free-form optics measurement with measurement resolution better than 50 nm. In addition, using the same technology, the architecture can be used for precision probing application for Solartron Ltd. with a measurement resolution better than 500 nm and in-line SPDT metrology for Precitech Inc. Hence, the financial and human resources can be shared within the UPT division of Ametek Inc.. Nevertheless, a flexible system architecture has to be developed to cover all these versatile applications. Moreover, the most demanding applications such has precision aspheric lens measurements with surface form error below 200 nm, require the system to reach its fundamental limits. Due to the fact that the CCM is the most versatile and robust system capable of covering the larger total market, the CCM is the solution maximising the “Investment benefit” in Equation 2.1. In addition, due to global UPT division interest in the CCM, the “Cost of investment” is mitigated. Therefore, the CCM is the technology maximising the ROI for Taylor Hobson Ltd. and the UPT.

The following chapter 3 will develop the design of a CCM architecture allowing the generation of a fundamental model which can then be modified for various applications. Since the optical head is the most critical part of the system, the design of a flexible and novel hyper-chromatic confocal head will be investigated. In Chapter 4, the previously designed system will be evaluated to compensate, mitigate or suppress the remaining systematic errors.

Chapter 3

Chromatic Confocal System optimisation and design

Even though the CCM is a linear system, optimisation of the chromatic confocal microscope is a strongly multi-variable non-linear problem. This chapter address the issue of designing such a system in a systematic and deterministic fashion.

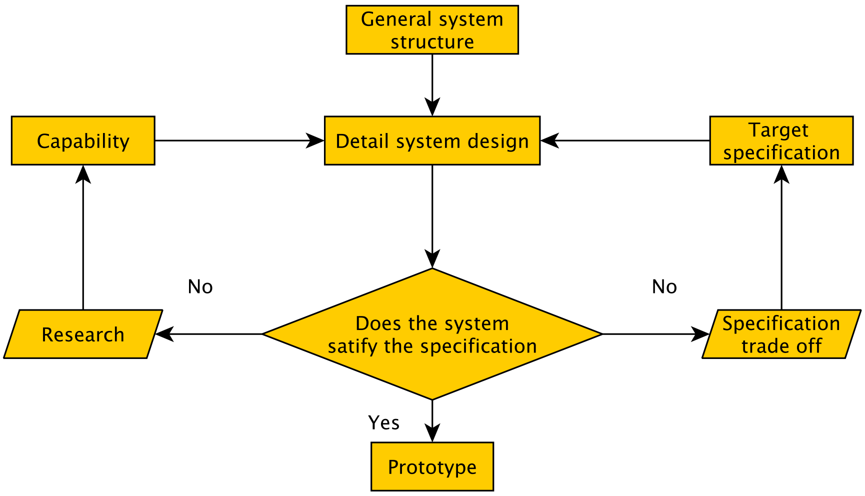

Figure 3.1: General chromatic confocal microscope design and optimisation method

To start the design process, the general system structure assembly is as shown as in Figure 3.1. From this general structure, with the available engineering capability, a detailed system design which meets the target specifications is built. The performance of the system is then computed. If the target specifications are achievable, a prototype is assembled. Otherwise, either a trade-off of the specifications is performed or further research is required to improve the engineering capability. These steps are repeated as long as necessary to reach the target specification. The final step is to build a prototype and to test the performance. If, the performance is not as expected, the model is corrected and the process is repeated.

To apply the previously described system design process, firstly, the CCM is systematised in terms of developing a theoretical CCM model. Secondly, for each individual sub-system, a current picture of the available technologies is then drawn. Finally, using the previously described theoretical model combined to the current technology capabilities a low cost and a high resolution version of the CCM may be designed.

3.1 Theoretical model of the chromatic confocal microscope

To match the specification of most application 6 performance design parameters were identified:

- Dynamic range.
- Maximum measurable surface slope [87].
- Range of measurement or chromatic depth of field [87].
- Working distance [87].
- Measurement sampling rate.
- Spot size [87].

Most of these parameters are defined in international standard ISO 25178-602:2010 [87]. Other parameters such as system size, temperature stability, ease of use, and cost could also be investigated. The aim of the design is to optimise all these parameters in order to reach the design specification. However, different structures

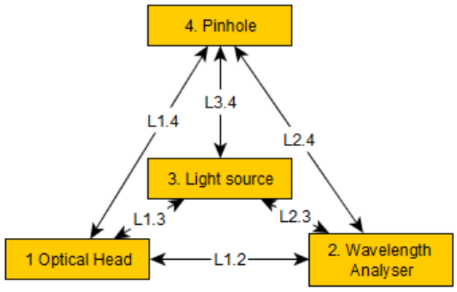

(a) Macro structure dependency of the chromatic confocal microscope.

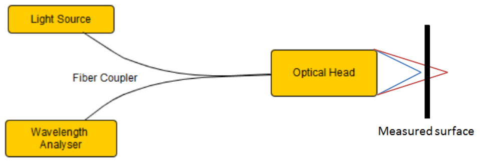

(b) Architecture of an optical fibre based chromatic confocal microscope.

of the system interact with each other. The interactions between the different structures are shown in the Figure 3.2a.

Firstly, the 4. Pinhole affects the confocality of the system and therefore the peak width (L1.4). Thus, a smaller pinhole will lead to a smaller peak response. In addition, the pinhole profile, convolved with the Point Spread Function (PSF) of the 1. Optical head, will determine the spot size and shape (L1.4).

Following the same principal, the pinhole profile convolved with the 2. wavelength analyser PSF will limit the resolution of the 2. Wavelength analyser (L2.4).

The 4. Pinhole size and numerical aperture limit the proportion on light into the system (L4.3).

Also, the 3. Light source determines the spectral range in the design of the 1. Optical Head (L1.3) and 2. Wavelength analyser (L12.13).

Finally, the 2. Wavelength analyser resolution power must be in accordance with 1. Optical head peak width (L1.2).

This is a non exhaustive list of the macro-interdependencies of the system. However, to design a system in a deterministic way, an analytical model of the CCM can be build. The following sections are first determines a the chromatic confocal peak shape using only optical parameters of the optical head. Then, analytical measurement uncertainty and linearity models are build to predict the performances of the system.

3.1.1 Theoretical peak shape model

The key issue of the CCM peak shape dependence on the various design parameters has not been well covered in the literature. Some researchers have adapted the theory of confocal microscopy, especially Equation 1.10 to the CCM which links the peak shape only to the numerical aperture and the illumination wavelength using wave theory [71, 66, 88]. The models have never been compared to experimental measurements. In fact, the correlation between theory and practice is poor as it will be shown in Figure 4.1.

A geometric optic approach based on ray tracing described in Figure 3.3 is proposed. The architecture of a fibre based CCM is presented in Figure 3.2b. This approach is inspired by a method which attempts to reduce the peak FWHM by using an annulus illumination [89]. The authors claim that this effect is related to the increase of the “effective NA”. This statement is true for confocal microscopy but not for CCM. Their mistake led me to a novel CCM peak shape model.

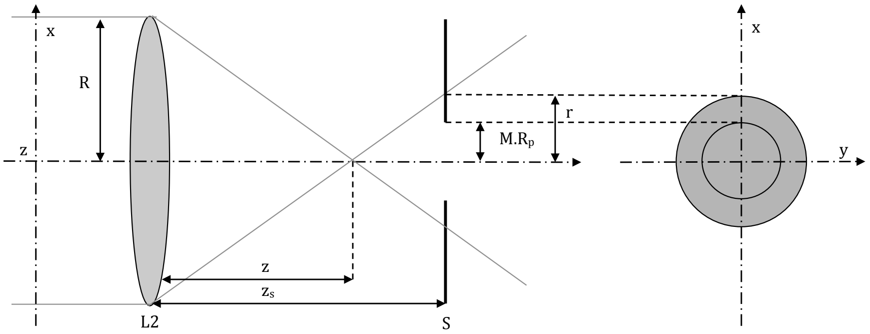

Figure 3.3: Ray tracing CCM model. Left : geometry description in the x-z plane. Right : projection of the geometry in the x-y plane. The de-focused light coupling efficiency is described as the area ratio between the magnified pinhole onto the surface and the conic section of the de-focussed light cone on the surface plane.

Thanks to the chromatic aberration of the optical elements, if the surface S is at a distance z_s within the range of measurement, the source pinhole of radius R_p is always imaged on the surface at a unique wavelength. In addition, the de-defocused beam, corresponding to other wavelength than the one focused on the surface, are focused at a distance z different than z_s. This de-focused beam is creating a conic section on the surface S. The normalised spectral irradiance I measured on the line sensor is the area ratio between the imaged pinhole and the conic section.

If the surface is normal to the optical axis, the conic section is a disk of radius r and the imaged pinhole is a disk of radius $M\ R_p$ where M is the magnification of the system and R_p the radius of the pinhole.

The radius r of the conic section function of the focus position z can be expressed as

$$r(z) = \frac{|z - z_s|\ R}{z_s}, \tag{3.1}$$

with R the useful radius of the exit lens L2 in Figure 3.3.

Hence, the normalised spectral irradiance I can be described as

$$I(z) = \frac{(M\ R_p)^2}{(M\ R_p)^2 + r(z)^2}. \tag{3.2}$$

By arranging Equation 3.2, and replacing $r(z)$ by Equation 3.1 the normalised CCM spectral irradiance can be expressed as

$$I(z) = \frac{1}{1 + \left(\frac{(z - z_s)\ R}{z_s\ M\ R_p}\right)^2}. \tag{3.3}$$

From the previous expression the FWHM can be calculated as

$$\text{FWHM} = \frac{2\ M\ R_p\ z_s}{R}. \tag{3.4}$$

It has been demonstrated that the FWHM of the peak is not only related to the illumination wavelength and the NA but as also to the magnification M of the optical system.

3.1.2 Analytical measurement uncertainty model

It is assumed that the measurement uncertainty is related to several parameters such as the FWHM of the chromatic confocal peak and the line sensor SNR. However, the literature does not analytically describe the link between these parameters and the measurement uncertainty. For the first time, a relationship will be established between the measurement uncertainty, the FWHM of the chromatic confocal peak, and the line sensor SNR. To estimate the link between these parameters, the measurement uncertainty is study numerically.

The concept is to generate a Gaussian peak $N = 1000$ times with a random noise of standard deviation σ_{CCD}. N is set to 1000 to minimise the numerical noise while maintaining the computation time to a couple of minutes. The peak position is calculated by using a Blais-Rioux peak detector [85]. The Blais-Rioux peak detector introduces a linear filter of order N_{BR} acting as a numerical derivative operator described as [**?**]

$$g_{N_{BR}}(p) = \sum_{n=-N_{BR}/2}^{-1} y(p+n) - \sum_{k=1}^{N_{BR}/2} y(p+n), \tag{3.5}$$

with y the irradiance measured on a CCD and p the index of the pixel with the highest irradiance. The sub-pixel peak position is then assessed as

$$p_{sub} = p + \frac{g(p)}{g(p) - g(p+1)}, \tag{3.6}$$

It has been found empirically that the order N_{BR} should be the closest integer to the FWHM of the measured peak to optimise the sub-pixel peak detection.

The measured peak position distribution $P(X)$ is assumed to be Gaussian and expressed as [90, eq. 2.1.1]

$$P(X) = \frac{1}{\sigma_p\sqrt{2\pi}} \exp\left[-\left(\frac{X - \mu_0 - \Delta\mu}{2\,\sigma_p}\right)^2\right], \tag{3.7}$$

where σ_p the standard deviation or measurement uncertainty, μ_0 the measured maximum position of the chromatic confocal peak, and $\Delta\mu$ the position detection or linearity error.

First of all, the CCM measurement uncertainty σ_p is calculated as a function of the FWHM of the peak. The results shown in Figure 3.4 indicate that the relationship between the CCM measurement uncertainty σ_p and the FWHM can be expressed as

$$\sigma_p = k\,\sqrt{\mathrm{FWHM}} + c, \tag{3.8}$$

where c can usually be neglected. The fitting correlation factor R is not significantly affected by the factor c. The factor c is just used to help the convergence of the fitting. It should be noted that this model is only valid for FWHM greater than 3 pixels. The first point, with a FWHM of 3 pixels, is not well fitted by the model in Figure 3.4. This poor fitting correlation for FWHM smaller than 3 pixels is reproducible and above the numerical noise.

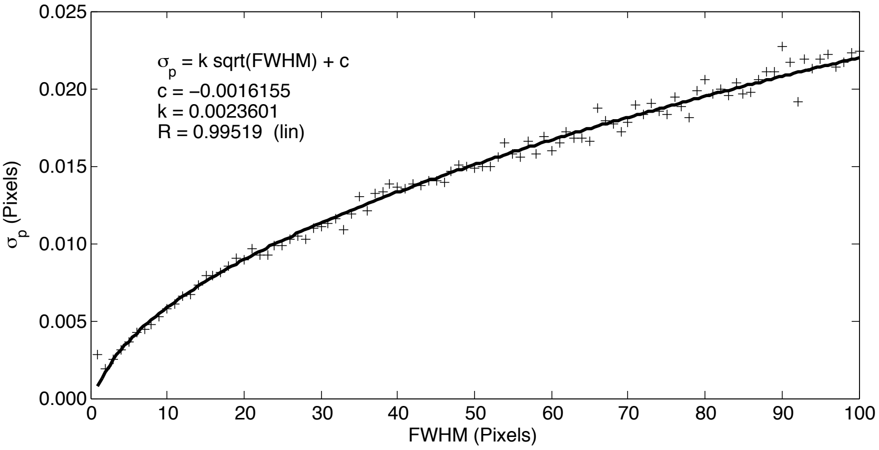

Figure 3.4: Cross marker : CCM measurement uncertainty σ_p function of the peak FWHM. Plain line: curve fitting on the computed points. The fitted curve has a high degree of correlation with the numerically calculated points which indicates a high degree of confidence in the model. This model seems to be valid for FWHM greater than 3 pixels only.

The lin sensor noise standard deviation σ_{CCD} is now changed; both the relationships between the CCM measurement uncertainty σ_p and the FWHM are maintained but the parameter k changes. A linear correlation is observed in Figure 3.5 between the parameter k and the line sensor noise standard deviation σ_{CCD} which can be written as

$$k = k'\,\sigma_{CCD}. \tag{3.9}$$

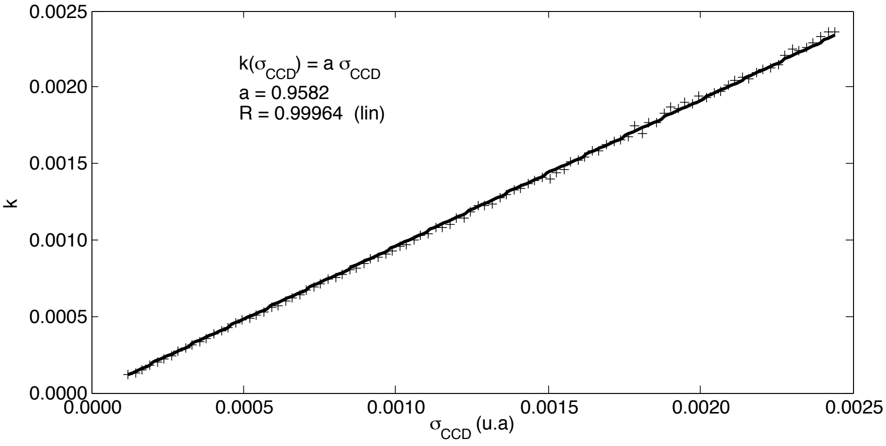

Figure 3.5: Cross marker : Coefficient k function of the line sensor noise standard deviation σ_{CCD}. Plain line: curve fitting on the computed points. The fitted curve highlight the linear dependency between the coefficient k and the CCD noise σ_{CCD}.

Equation 3.4 can be re-written as

$$\sigma_p = \sigma_{CCD}\, k' \, \sqrt{\mathrm{FWHM}}. \tag{3.10}$$

So far, the maximum spectral irradiance of the CCM peak is normalised to 1. If the maximum spectral irradiance is now normalised between 0 and 1, the coefficient k' varies as shown in Figure 3.6.

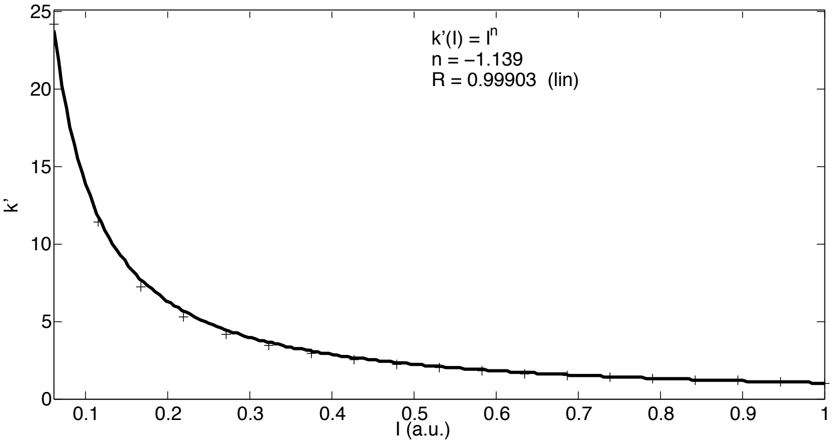

Figure 3.6: Cross marker : coefficient k' function of the maximum spectral irradiance I. Plain line: curve fitting on the computed points. A power fit with a coefficient of -1.139 shows a high correlation between the coefficient k' and the maximum spectral irradiance with a correlation factor R of 0.999.

Figure 3.6 suggests that the relationship between the coefficient k' and the maximum spectral irradiance I can be expressed as

$$k' = \frac{1}{I^n}, \tag{3.11}$$

with $n \approx 1.139$.

By combining Equation 3.11 and Equation 3.10, the measurement uncertainty of the CCM can be approximated using the following expression

$$\sigma_p \approx \frac{\sigma_{CCD}}{I^n}\sqrt{\text{FWHM}}, \tag{3.12}$$

The measurement uncertainty in pixels can be converted to the measurement uncertainty in position by using the dispersion of the wavelength analyser $\frac{\delta\lambda}{\delta p}$ and the dispersion of the optical head $\frac{\delta z}{\delta\lambda}$ as the following

$$\sigma_z \approx \frac{\delta z}{\delta\lambda}\frac{\delta\lambda}{\delta p}\left(\frac{\sigma_{CCD}}{I^n}\sqrt{FWHM\left(\frac{\delta\lambda}{\delta p},\frac{\delta z}{\delta\lambda}\right)}\right). \tag{3.13}$$

By examining Equation 3.13, it can be observed that the equation is dimensionally incorrect. In fact, Equation 3.13 is expressed in $(L.pixel^{-1/2})$ when it should be (L). Thus, using Equation 3.13, the measurement uncertainty can be estimated only. Equation 3.13 must be used with care; the FWHM can only be expressed in pixels. In addition, this expression is based on assumptions such as the line sensor noise statistical distribution, the peak shape, and the real peak position which has been set to be equidistant from two adjacent pixels.

The measurement uncertainty function of the nearest pixel distance is not significantly correlated to the FWHM of the CCM peak. With every other variable kept constant, the variation of the measurement uncertainty function of the distance to the nearest pixel is less than 10%. Hence, the latter relationship can be neglected.

3.1.3 Analytical linearity error model

The previous section has demonstrated that the measurement uncertainty shows little correlation with the distance to the nearest pixel. However, the linearity error or position detection error $\Delta\mu$ as a function of the nearest pixel distance is significant, as shown in Figure 3.7. From Figure 3.7, the measurement error $\Delta\mu$ function of the nearest pixel distance Δp can be estimated using the following expression:

$$\Delta\mu(\Delta p) \approx A\ \sin(2\,\Delta p\,\pi)\ \mathrm{FWHM}^{B} \tag{3.14}$$

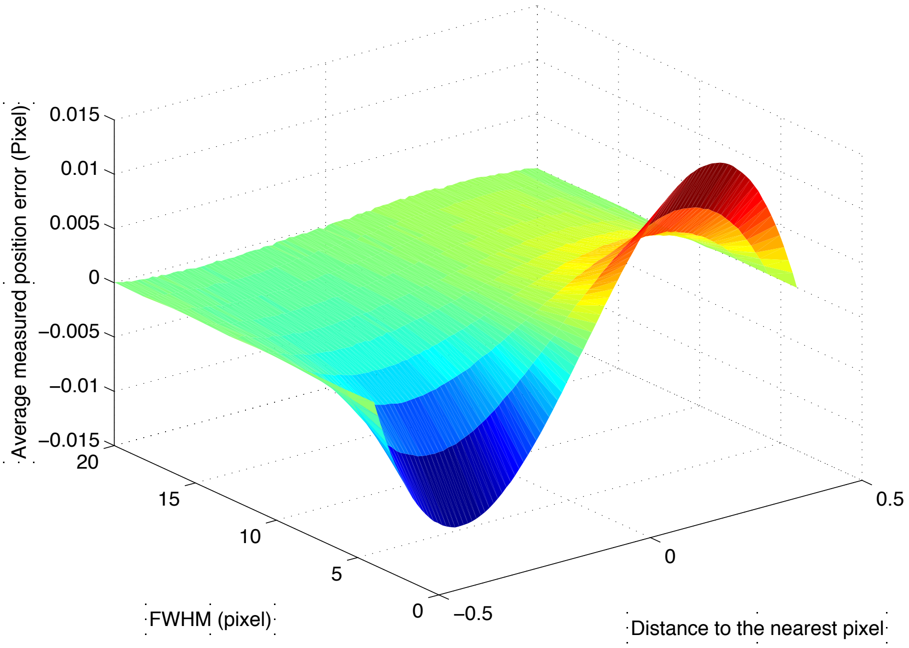

Figure 3.7: Position detection error function of the FWHM of the chromatic confocal peak and the distance of the peak to the nearest pixel. The errors rise sharply for FWHM smaller than 5 and exhibit a sinus as a profile function of the distance to the nearest pixel.

The parameters A and B are determined empirically and are found to be equal to 0.18698 and -1.8627 respectively, as shown in Figure 3.8. Consequently, the FWHM should not be minimised to reduce the measurement uncertainty σ_z in equation 3.13. The FWHM must be calculated so that the maximum linearity error $\Delta\mu$, occurring at a nearest pixel distance Δp of 1/4 is equal to the extended measurement

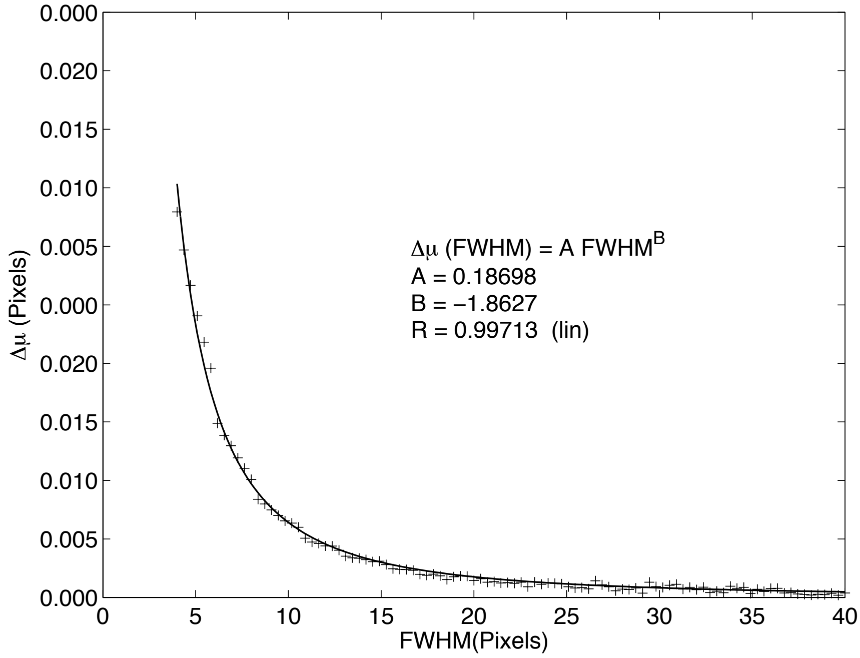

Figure 3.8: Position detection error function of the FWHM of the chromatic confocal peak for a distance to the nearest pixel equal to 0.25 pixel. The distance of 0.25 pixels to the nearest pixel corresponds to the maximum position detection error

uncertainty or resolution $k_e\, \sigma_p$ and can be expressed as

$$\Delta\mu\left(\frac{1}{4}\right) = k_e\, \sigma_p. \tag{3.15}$$

where the factor k_e expands the level of confidence [3].

Hence, the optimum FWHM is

$$FWHM_{opt} = \left(\frac{A}{k_e\, \sigma_{CCD}}\right)^{-\frac{2}{2\,B-1}}. \tag{3.16}$$

Equation 3.16 is the starting point for the optical design of the chromatic confocal head. For a given CCD, the optimum FWHM can be calculated. Then, using Equation 3.4, the optical parameters, such as the magnification M and NA, can be calculated.

3.2 System description and available technologies

To understand the detailed architecture, the system is divided as a Work Breakdown Structure (WBS) as shown below and in Figure 3.9

1. CCM
    1.1. Optical Sytem
        1.1.1. Optical Head
        1.1.2. Wavelength Analyses
        1.1.3. Light Source
        1.1.4. Light Splitter
    1.2. Electronic
        1.2.1. Hardware
        1.2.2. Software

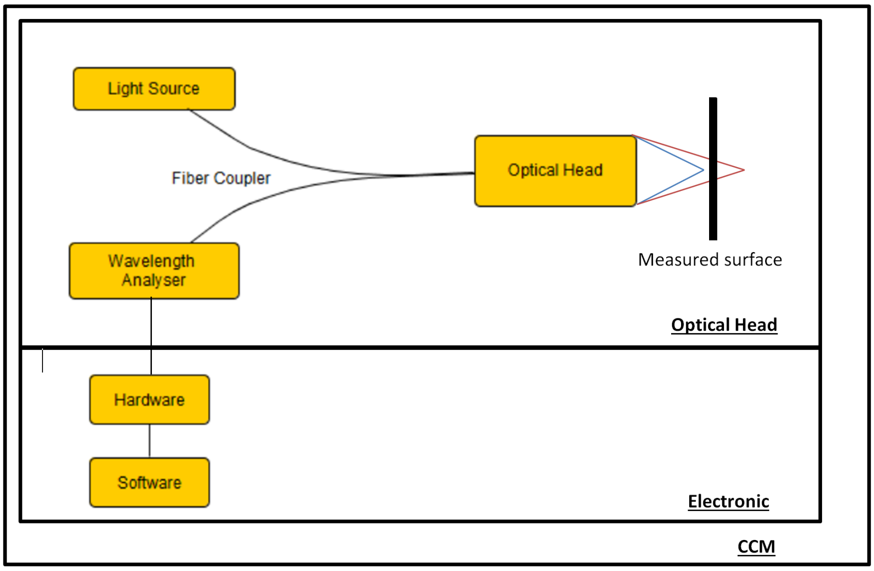

Figure 3.9: Schematic of the architecture of an optical fibre based CCM.

Each of these sub-systems has to be designed and optimised individually. Moreover, the interaction between the sub-systems has to be considered. Nevertheless, the available technologies limit the possible system combinations. Hence, the currently available technologies for each individual sub-system will be investigated.

3.2.1 The light source

Generally the light source needs to be broad-band and continuous. Historically, discharge lamps were in use first [57]; in particular, xenon discharge lamps, which have the advantage of providing both a high output luminous flux of 3,000 lm [91] and a large spectrum from the Ultra Violet (UV)to the IR, as shown in Figure 3.10 [92, p. 701]. However, a disadvantage is its large solid emitting angle of 4π sr which leads to inefficient fibre coupling. STIL SA [62] and Micro Epsilon Gmbh [65] still use xenon arc discharge lamps for their high speed CCM with a sampling rate of approximately 50 kHz. In addition, in a personal interview with the optical engineer from Digital Surf SA, Dr. Hans J. Jordan highlighted that the temperature of the lamp can reach more than $70°C$ and the lifetime is also restricted to around 3,000 hours [91].

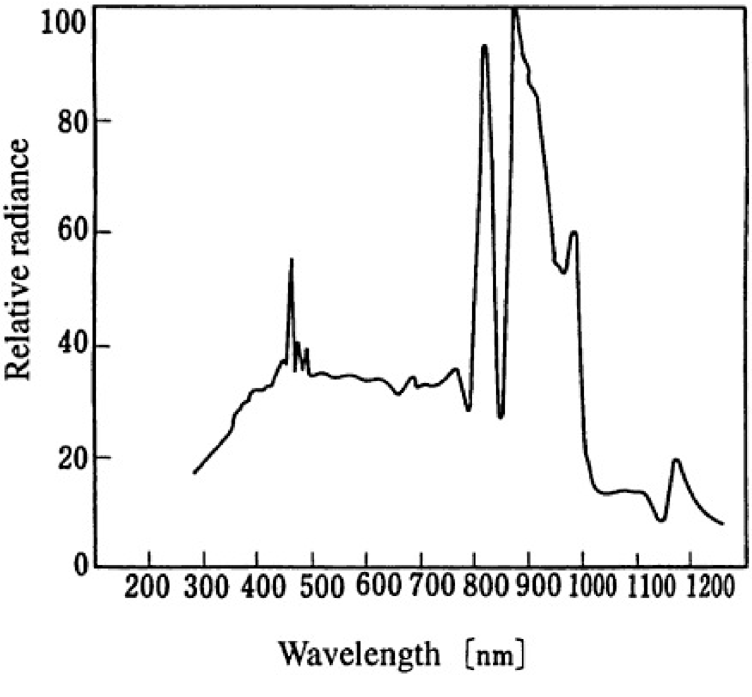

Figure 3.10: Spectrum of a low pressure Xenon arc discharge lamp [92, p. 701]

Nowadays, high power Light Emitting Diode (LED) with output power of more than 200 lm, are becoming ever more suitable as inexpensive alternatives for the CCM. High power white light LEDs use a blue LED to stimulate a phosphor powder. Then, through de-stimulation, a white continuous spectrum is emitted [93, p. 15-17]. A large range of LEDs is now available; one of the key parameters for the

CCM is the power per square meter per steradian. Because such LEDs are both inexpensive and exhibit a long lifetime of more than 10,000 hours, high power LED are becoming more suitable and are currently used in most industrial systems.

Super-luminescent Light Emitting Diodes (SLEDs) offer a high optical output of several mW [94] easily coupled into an optical fibre due to the guided nature of the light within the SLED structure [95]. The structure of a SLED is similar to a diode laser. However, instead of creating a resonance inside a cavity, the SLED structure avoids any resonance. Hence, spontaneously emitted light is trapped in the waveguide created by the PN junction [95]. By combining the natural bandwidth of two PN junction, SLEDs with a spectral width of 100 nm have been realised as shown Figure 3.11 [96].

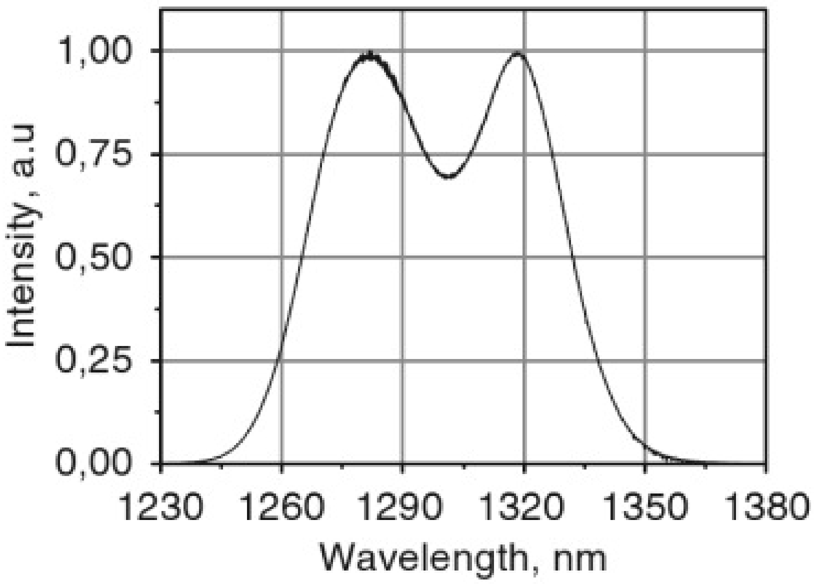

Figure 3.11: Spectrum of a dual broadband SLED [96]

Because of the spontaneous nature of the emission at the PN junction, larger bandwidths are achieved in the Near Infra Red (NIR) than in the visible domain [95]. Moreover, SLEDs have been developed for optical coherent tomography applications [97]. Thus, the emission wavelength of a SLED corresponds to the bio-photonic window [98]. No reference has been found indicating that SLEDs have been used in a CCM, although SLEDs can be directly coupled to a monomode optical fibre. However, it should be noted that SLEDs are more expensive than LEDs.

Supercontinuum lasers are a new source offering a high power white light source of 2 W [99]. A high energy pulse is injected into a photonic crystal fibre [100]. Due to the large energy per volume ratio, several non-linear effects, such as 4-wave mixing, Raman/Stoke shifts, and second harmonic generation occur in the fibre [100], resulting in an energy transfer from the original pulse to other wavelengths, throughout the length of the fibre, so that the laser spectrum becomes a continuous broadband source from UV to far NIR [100]. Supercontinuum lasers offer the best solution for CCM systems. However, their size and price currently restrict the use to non-commercial applications [101]. Table 3.1 summarises the performance of the various sources.

Table 3.1: Comparison of the suitable light source for a chromatic confocal microscope

	Discharge lamp	SLED	Supercontinuum Laser	LED
Cost	£500	£2,500	£10,000	£5
Luminous flux	3,000 lm	10 mW	2 W	200 lm
Numerical Aperture	4π sr	0.1	0.1	0.8
Spectral range	600 nm	200 nm	1200 nm	400 nm
Spectral Domain	UV/VIS/NIR	NIR	UV/VIS/NIR	VIS
Lifetime	500 h to 2,000 h	NA	NA	10,000 h
Heat dissipation	high	low	high	medium
Power consumption	high	medium	high	low
Size	medium	small	large	small

3.2.2 The light circulator

A beam-splitter is the simplest and easiest approach. An un-polarised beam-splitter with broadband anti-reflection coatings can be used to generate the input and output signals. Historically, a beam-splitter was the first choice [57].

Fibre couplers enable the light to be distributed into two or more arms. In addition, the ratio between the two arms can be chosen. A standard approach is to fuse two fibre cores [102, p. 361]. However, the coupling ratio depends on the wavelength. Therefore, the fibre coupler must be chosen to match the wavelength range of the source. A possible alternative to a fibre coupler is a fibre circulator.

No source has been found of a CCM using a fibre circulator.

Fibre circulators allow theoretically the transmission of 100 % of the light from the source towards the surface and importantly allow the return of 100 % of the collected reflected light to the spectrometer. Broadband circulators are not widely used, particularly in the visible domain. Nevertheless, due to the development of optical coherent tomography, SLEDs and circulators have been designed to function in conjunction, hence both SLEDs and circulators can be used in the same spectral domain. Table 3.2 summarises the described technologies

Table 3.2: Comparaison of suitable light splitters for a chromatic confocal microscope

	Circulator	Coupler	Telecom Coupler	Beam Splitter
Cost	£350	£250	£50	£70
Complexity	Low	Low	Low	High
Spectral Bandpass	1200-1400 nm	400-800 nm	400-800 nm	400-800 nm
Efficiency	50 %	25 %	12 %	25 %

3.2.3 The optical head

This section firstly identifies the most appropriate hyper-chromatic lens technology. Secondly, the manufacture of Hybrid Aspheric Diffractive (HAD) lenses using SPDT is studies analytically. This study leads to the use of a SDS lens, a special type of HAD lens. Thirdly, the implementation of an SDS lens is studied to achieve a “state of the art” CCM objective head. Finally, special ray tracing computational tools for hyper-chromatic lens using HAD are developed.

3.2.3.1 Hyper-chromatic lens technology

A CCM hyper-chromatic objective lens is required to illuminate a surface with a beam that exhibits a nearly diffraction limited point-spread function over a defined z-range, the z-location of any such point-spread function being a function of wavelength. Four strategies can be used to create an objective with sufficiently high chromatic aberration:

- Using gradient index lenses [68].
- Using the natural dispersion of glass [57].
- Using diffractive lenses [73].
- Using hybrid refractive diffractive lenses.

Gradient index lenses are widely used for compact chromatic confocal lenses [68]. Nevertheless, their thermal stability restricts their application range [68]. In addition, in an interview, the optical engineer from Digital Surf SA, Dr Hans J. Jordan highlighted that the optical performance repeatability exhibited from one lens to another is insufficient to achieve a diffraction limited chromatic confocal system.

The refractive approach is the most classical one. By taking advantage of the chromatic dispersion of the glass, the lens generates an axial focus that is a function of wavelength. For a thin lens, the focal length F_{Ref} can be estimated by [103]

$$\frac{1}{F_{\mathrm{ref}}(\lambda)} = \left(n\left(\lambda\right) - 1\right)\left(\frac{1}{R_1} - \frac{1}{R_2} + \frac{\left(n\left(\lambda\right) - 1\right)\, d}{n\left(\lambda\, R_1\, R_2\right)}\right), \tag{3.17}$$

where λ is the illumination wavelength, n the lens refractive index, d the lens thickness, and R_1 and R_2 are the radii of curvature of the lens.

As expressed in this equation, the refractive index of the lens is a function of the illumination wavelength. The refractive index itself is a function of the illumination wavelength and can be described using the Sellmeier equation [104]:

$$n(\lambda) = \sqrt{1 + \sum_{i=1}^{k} \frac{\lambda^2 B_i}{\lambda^2 - C_i}}. \tag{3.18}$$

The Sellmeier coefficients B_i and C_i are determined empirically.

In the case of a refractive lens, the focal length change as a induced by the chromatic aberrations are not linear and are limited to the dispersion of the material, as shown in Figure 3.12. However, as described below, diffractive lenses behave completely differently.

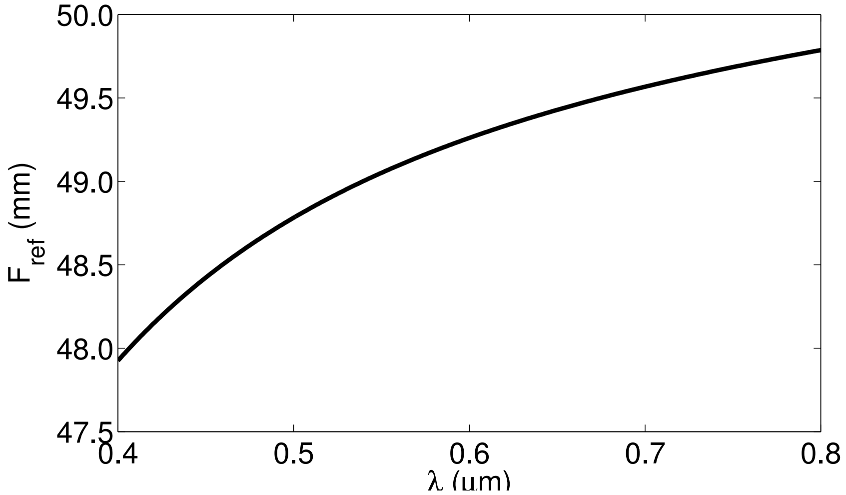

Figure 3.12: Change in focal length of a bi-convex lens of 50 mm radius and 5 mm thick of BK7 glass due to non-linear dispersion.

By collapsing the thickness of a lens to the order of the illumination wavelength, the lenses cannot be described by a ray trace method. The light is now considered as a wave. The continuous phase profile ϕ of a diffractive lens can be spherical, quadratic, polynomial or any circular symmetric function. Figure 3.13 shows a quadratic continuous profile [74].

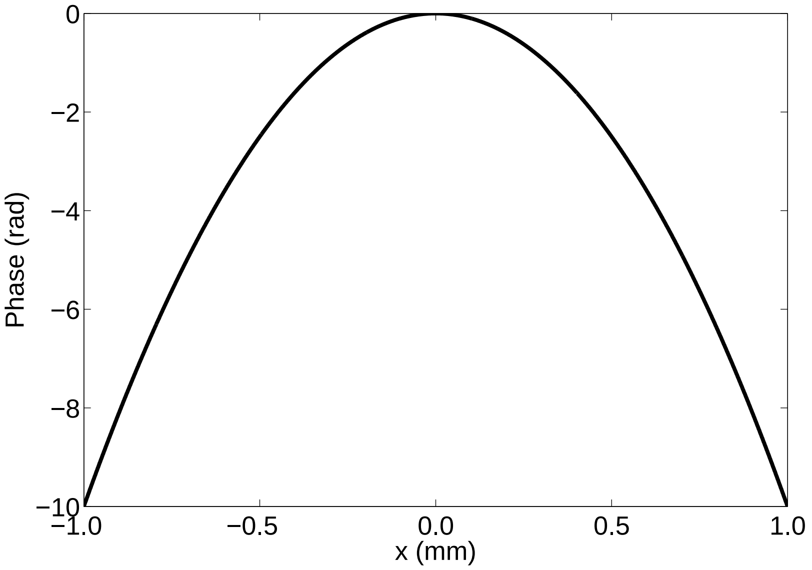

Figure 3.13: Continuous quadratic phase function of a lens.

The continuous quadratic profile shown in Figure 3.13 is modulated by $\delta\phi$, as shown in Figure 3.14 for a modulation $\delta\phi$ of 1.

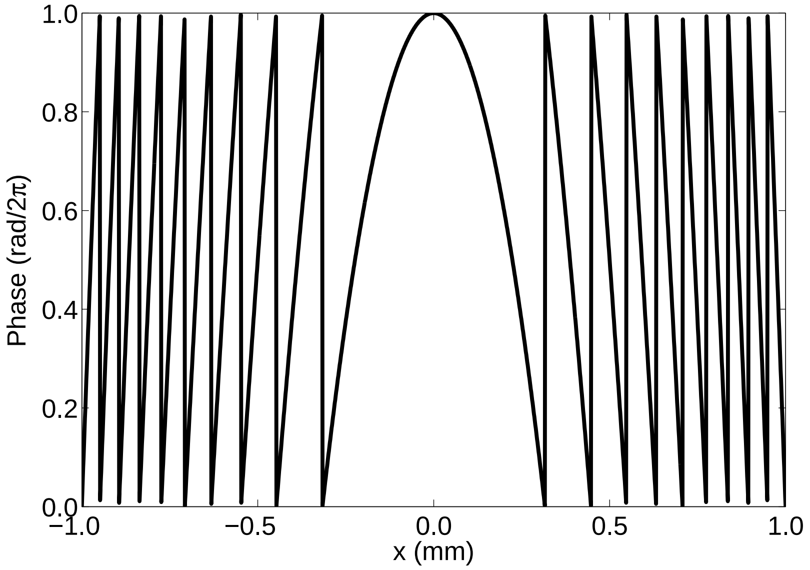

Figure 3.14: Modulated quadratic phase function of a diffractive lens.

By solving the Fresnel diffraction integral for these lenses, the focal length can be expressed as [74] :

$$F_{Diff} = F_0 \frac{\lambda_D}{\lambda} \frac{p}{m} \tag{3.19}$$

and

$$\delta z = \frac{p\,\lambda_D}{n-1} \tag{3.20}$$

and

$$\delta\phi = \delta z \frac{2\pi n}{\lambda_D} \tag{3.21}$$

where m is the diffraction order, p the harmonic, F_0 is the focal length at λ_D, δz the physical thickness of the diffractive lens, n the refractive index of the lens material, and $\delta\phi$ the phase thickness of the lens.

Hence, diffractive lenses have a focal length inversely proportional to the illumination wavelength. Therefore, as shown in Figure 3.15, the chromatic aberration of a diffractive lens is larger than for a refractive lens of similar focal length.

The chromatic aberrations of a diffractive lens are an order of magnitude higher than for the equivalent refractive lens. Therefore, diffractive lenses are attractive candidates for a hyper-chromatic role. However, the outer diffractive ring interval

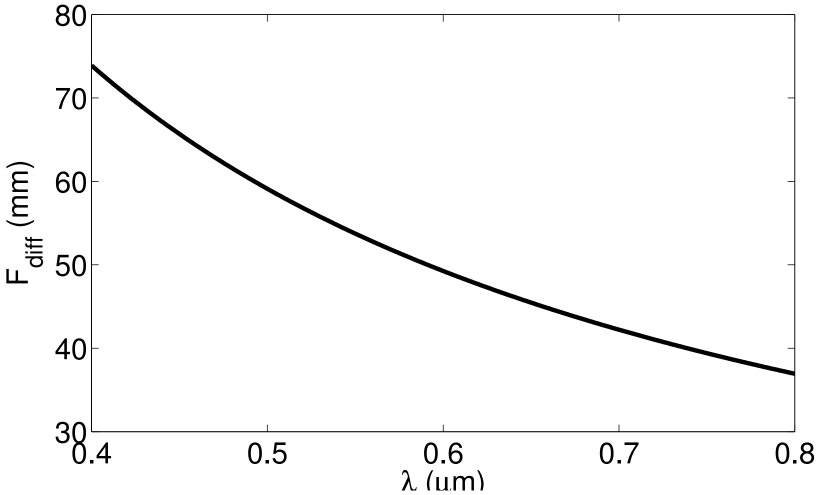

Figure 3.15: Change in focal length of a diffractive lens as a function of the illumination wavelength having a focal length at 0.6 μm equal to the lens described in Figure 3.12.

is directly proportional to the focal length. Hence, diffractive lenses with an NA of 0.2 and a chromatic depth of field in the visible domain of 3 mm typically exhibit more than 500 diffractive zones with a outer ring interval of less than 10 μm. Such a lens cannot be manufactured using SPDT without large light losses and geometric aberration.

So, summarising, refractive lenses allow the design of systems with NA exceeding 0.5 but with changes in focal length of less than 2 mm between 0.4 μm and 0.8 μm, diffractive lenses exhibit a change in focal length of more than 30 mm over the same wavelength range but are difficult to manufacture for NA value exceeding 0.2. The proposed solution is to use both [105].

The idea underlying Hybrid Aspheric Diffractive (HAD) lenses is to use the refractive profile for imaging and the diffractive profile for the chromatic aberrations [74]. The diffractive profile is superimposed onto the refractive profile as shown in Figure 3.16.

The chromatic aberrations can now be tailored to a specific NA and chromatic dispersion as shown in Figure 3.17

Furthermore, HAD surfaces extend the application domain of the CCM as shown in Figure 3.18.

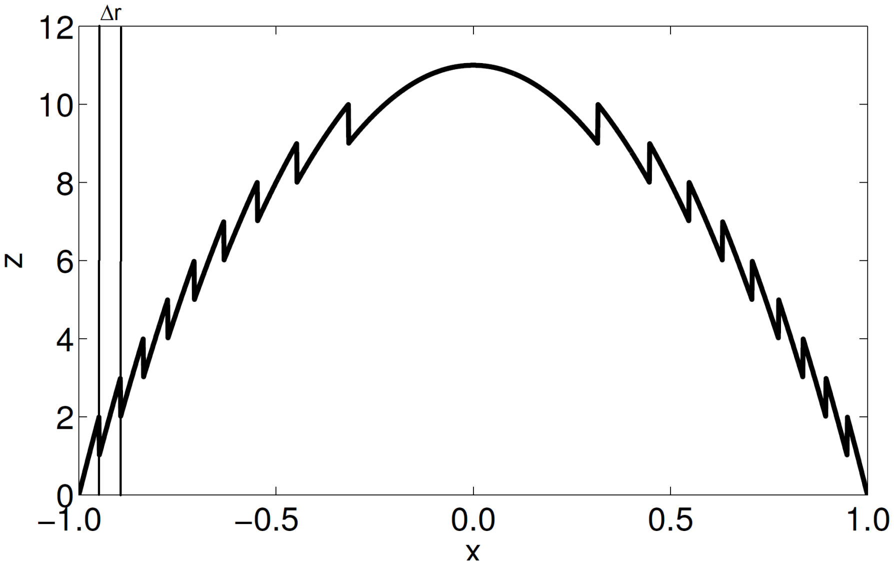

Figure 3.16: Profile of a HAD lens, the diffractive lens profile is simply super-imposed onto the refractive profile. Hence the number of elements on the optical design is reduced. The diffractive ring interval Δr is also shown

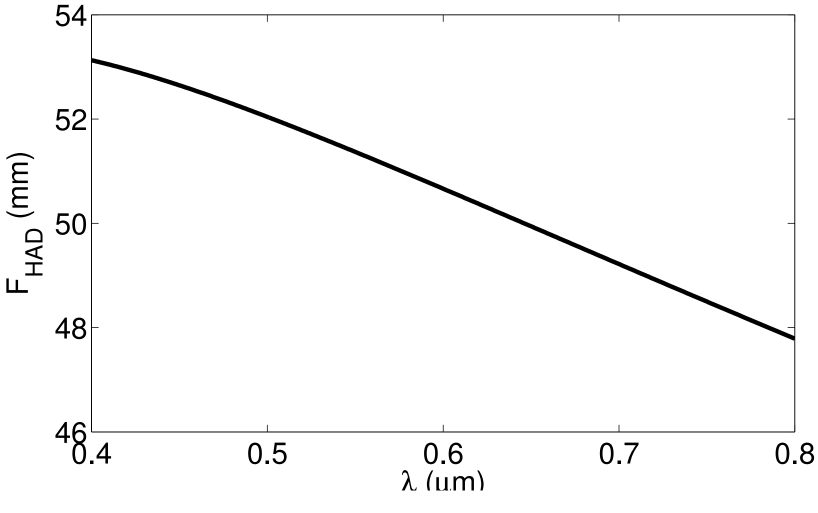

Figure 3.17: Focal length of a HAD lens between 0.4 μm and 0.8 μm. The chromatic aberrations are twice that of those of an equivalent refractive lens while the outer ring interval is 5 times larger than an equivalent diffractive lens. In addition, the linearity is improved.

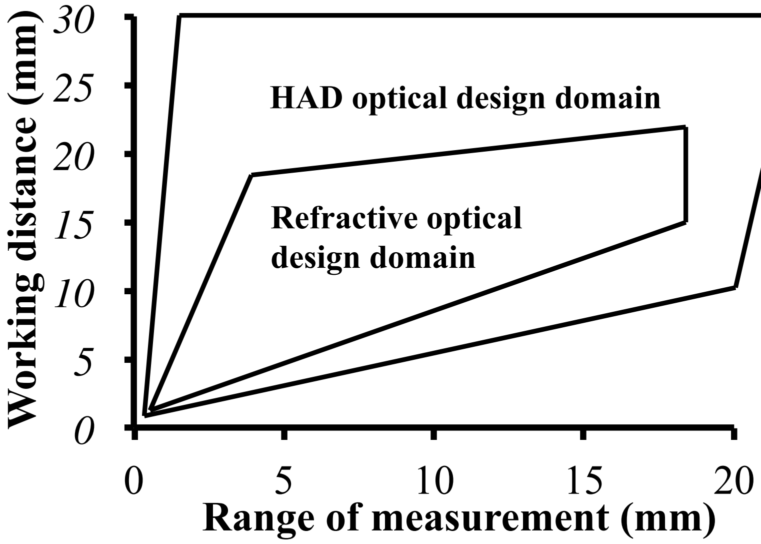

Figure 3.18: Map of possible optical design using a refractive and a HAD hyperchromatic lens of 8mm diameter. The HAD approach allows designs which are not achievable using refractive technology.

In addition, by increasing the harmonic p in equation 3.19 and 3.22, several orders can overlap spatially but not spectrally as shown in Figure 3.19. Hence, one surface is represented spectrally by several peaks. For the harmonic p of 11, 5 peaks can be observed simultaneously. By simply averaging the measured peak position, the noise is reduced by a factor $\sqrt{5}$.

Another approach is to use an intermodal harmonic with $p = 1.5$ as shown in Figure 3.20. Using the latter configuration, the energy is spread between two modes which extends the range of measurement by a factor two without changing the measurement uncertainty. Hence, the Dynamic Range (DNR) is doubled.

The diffraction efficiency of a diffractive lens decreases when the wavelength differs from the design wavelength [106]. Nevertheless, some arrangements allow the diffraction efficiency to exceed 95% over more than 400 nm of spectral bandwidth [49]. The scalar diffraction efficiency of a HAD can be expressed as [49]:

$$\eta = \operatorname{sinc}^2\left(p\frac{\lambda_0}{\lambda}\frac{n_1(\lambda) - n_2(\lambda)}{n_1(\lambda_0) - n_2(\lambda_0)} - m\right), \tag{3.22}$$

where $sinc(x) = sin(\pi x)/(\pi x)$, λ is the illumination wavelength, n_1 the refractive index before the surface, and n_2 the refractive index after the surface.

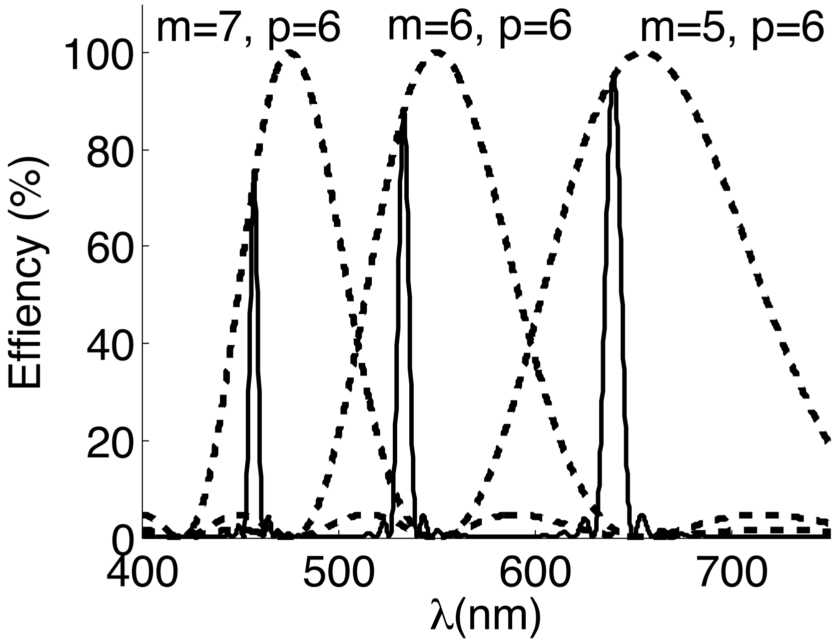

Figure 3.19: Dash line: Diffraction efficiency of 3 consecutive modes of harmonic $p = 6$. Plain line: Chromatic confocal response. For one surface, 3 peaks are observed simultaneously, therefore the measurement uncertainty is improved.

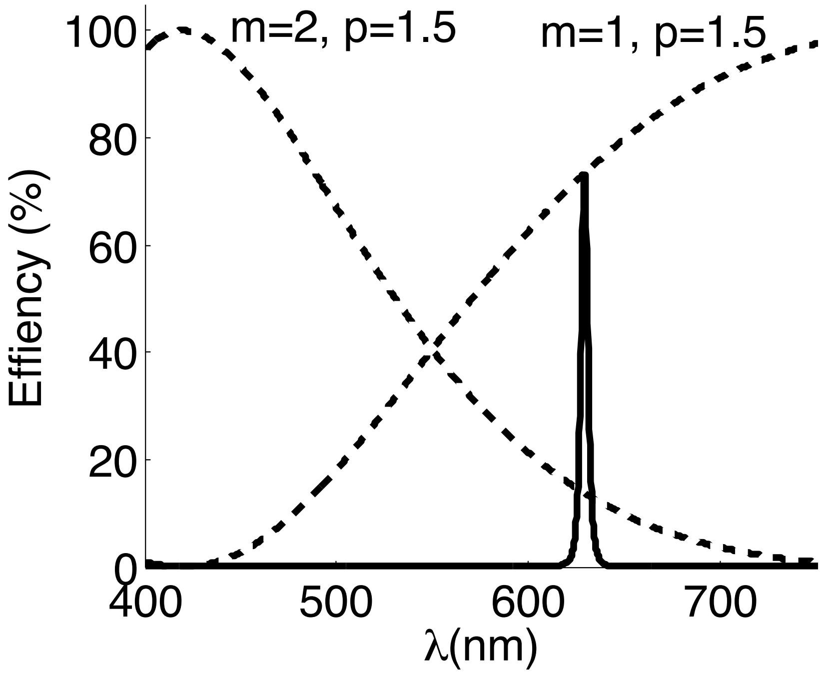

Figure 3.20: Dash line: Diffraction efficiency of two consecutive modes of harmonic $p = 1.5$. Plain line: Chromatic confocal response. By spreading the energy between two modes, the range of measurement is extended by a factor two.

In most cases the second medium is air. Therefore the refractive index is 1 which permits the realisation of thin and simple HAD lenses. However, the diffraction efficiency decreases when the illumination wavelength differs from the design wavelength [74].

It is assume that the second medium is not air, the efficiency can remain constant if the following condition is satisfied [49],

$$p\frac{\lambda_0}{\lambda}\frac{n_1(\lambda)-n_2(\lambda)}{n_1(\lambda_0)-n_2(\lambda_0)}=m \tag{3.23}$$

Hence, material satisfying Equation (3.23) over the illumination spectra will exhibit higher diffraction efficiency than with air. Several methods are presented on the literature to create multilayer HAD lenses [49]. However, most of these methods are complex and not suitable for HAD lenses. A cement concept is proposed as shown in Figure 3.21. The HAD is placed between two pieces of the same material and bonded by using the appropriate material. Therefore, the cement can be any material with a high viscosity at room temperature before curing. To find a suitable pair of materials a search algorithm has been developed combining any possible combination of materials on the database. This computes the diffraction efficiency using Equation 3.22. The design wavelength is then optimised in order to maximise the average diffraction efficiency.

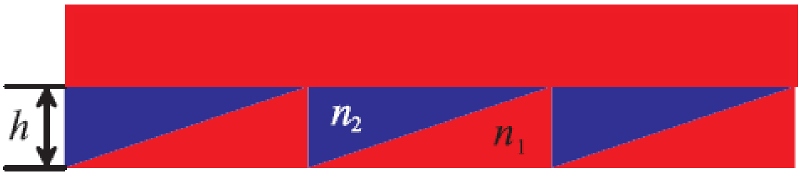

Figure 3.21: Diagram of the cement concept of the multilayer HAD. n_1 is the refractive index of the material and n_2 the refractive index of the cement material

As shown in Figure 3.22 and Figure 3.23 the couple 480R® [107] and NOA89® [108] has an average diffraction efficiency of more than 97 % while in the case of a 480R® with air, the average diffraction efficiency is below 70 %.

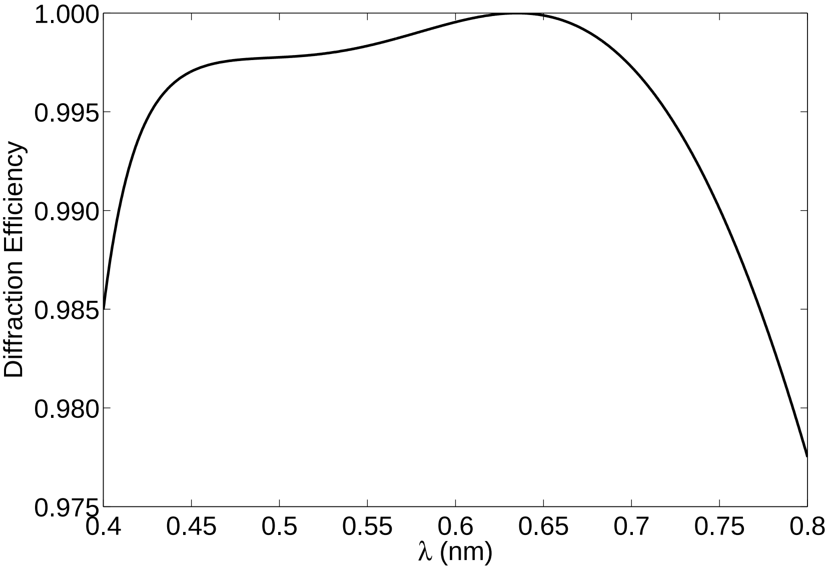

Figure 3.22: Diffraction efficiency of the doublet 480R® plastic with the NOA89® glue. Even with a broadband illumination, the diffraction efficiency exceed 98 % over 400 nm of spectral bandwidth.

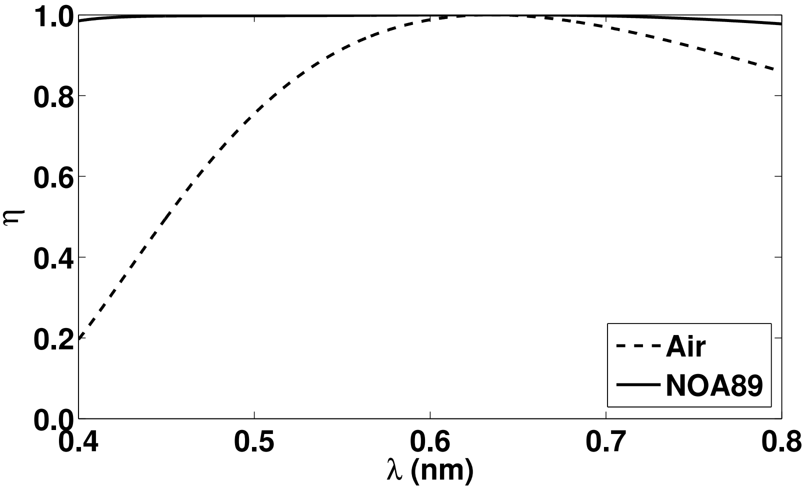

Figure 3.23: Diffraction efficiency of the 480R® plastic with air and with the NOA89® glue. The couple 480R® and NOA89® exhibit significantly higher diffraction efficiency than the couple 480R® and air.

These preliminary results are encouraging but there are several issues related to the broadband HAD design as exhibited in Table 3.4. On the one hand, broadband HAD lenses exhibit a higher diffraction efficiency over the wavelength range, on the other hand, the thickness of broadband HAD lenses needs to be 40 times higher than the thickness of a HAD lens. This step height, 40 times higher than a standard HAD lens raises several manufacturing issues. Therefore, the choice between HAD and broadband HAD is not only related to their theoretical diffractive efficiency but also to the manufacturability of the lenses.

Table 3.3: Relative comparison of different HAD structures for hyper-chromatic applications.

	GRIN	Refractive	Diffractive	HAD
Off the shelf availability (Number of supplier)	≈ 30	> 50	≈ 10	≈ 10
Custom design availability (Minimum number of supplier)	10	50	30	10
Temperature sensitivity $(\%/^{\circ}C)^1$	0.1	0.1	0.1	0.01
Numerical Aperture	> 0.5	> 0.5	≈ 0.1	> 0.5
Chromatic Dispersion $(\mu m/\mu m)^2$	≈ 33	≈ 15	≈ 150	≈ 75

^{1} : lowest linearity error expressed in % of the measurement range per $^{\circ}C$.
^{2} : Chromatic dispersion in μm of measurement range per μm of spectral range for comparable chromatic confocal optical heads of approximately 6 mm of clear aperture.

Table 3.4: Broadband (stack of 7 NOA89®/480R®) and thin HAD comparison for a quadratic diffractive lens of optical power 0.005mm^{-1}.

	Thin HAD	Thick HAD
Surface slope	low	high
Step height	1 μm	39 μm
Diffraction efficiency	>70 %	>97 %
Scattering losses	0.1 %	0.1 %
Shadow zone losses	38 %	3 %
Impulse response losses	1 %	7 %

Despite the attractiveness of HAD lenses compared to the other hyper-chromatic lens technologies highlighted in Table 3.3, the manufacturing of HAD surfaces with high diffractive power and efficiency is a challenge [109]. In fact the outer diffractive ring interval Δr, shown in Figure 3.16, is proportional to the focal length f of the diffractive lens as shown in the following equation

$$\Delta r = \frac{m}{p} \frac{f \lambda_0}{2R}. \tag{3.24}$$

Here m is the diffraction order, p the harmonic, R the lens radius, f the focal length and λ_0 the design wavelength.

The design of hyper-chromatic objectives using HAD lens requires dedicated manufacturing, optical design, and ray tracing models. These three points are studied in the following sub-sections.

3.2.3.2 Manufacturing error of diffractive lenses

To use a HAD surface in a CCM application it has been assumed the last diffractive interval is less than 10 μm and the number of diffractive ring more than 500. Using the current technology, it is not possible to manufacture such surfaces using SPDT. To understand the limiting factors of the manufacturing, a SPDT manufacturing error model has been built. Figure 3.24 shows the manufacture of a diffractive lens using an SPDT machine.

Due to the hemispheric tool geometry and the spiral tool path, SPDT manufacturing carries intrinsic errors. The three main intrinsic errors are:

- Tool shadow [110].
- Machine response.
- Surface scattering [110].

Due to the tool size and shape, a part of each zone cannot be machined as shown in Figure 3.25. When the tool contacts the theoretical surface at the discontinuity, the zone Λ has the shape of the tool and not the required diffractive profile. Therefore, the light going through this zone will not be correctly diffracted toward the focus.

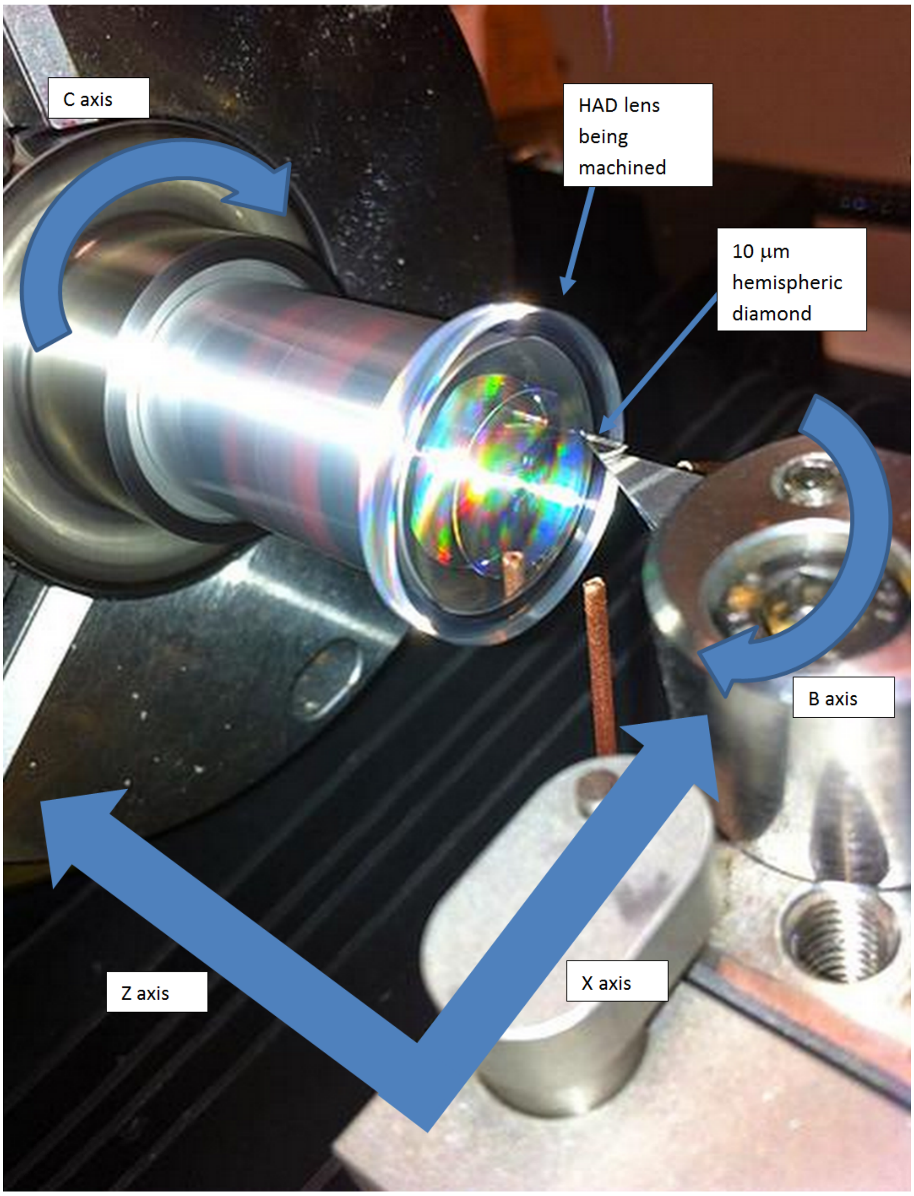

Figure 3.24: Picture of diffractive lens being manufactured on a SPDT machine.

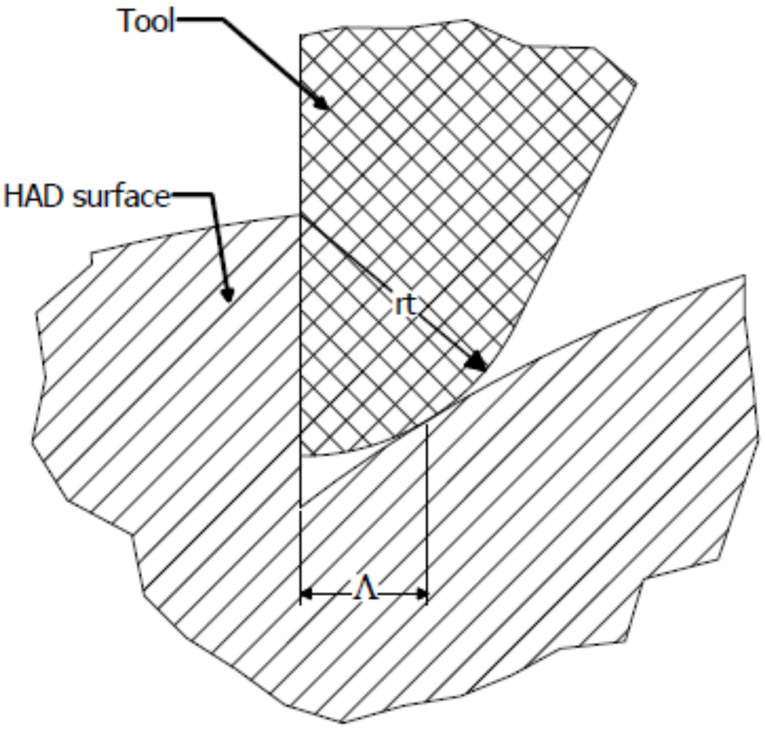

Figure 3.25: Tool at the diffractive zone discontinuity. The shadow zone Λ represents the part of the diffractive profile which cannot be machined.

The amount of light loss due to the tool shadow zone is the ratio of the area of the shadow zone over the area of the ring if it is assumed that the illumination is constant is over the ring, then this can be expressed as

$$\eta_{\text{ring}} = 1 - \frac{2\pi r\Lambda}{2\pi r\Delta r} = 1 - \frac{\Lambda}{\Delta r}, \tag{3.25}$$

where r is the radial position and Δr is the ring interval.

The integrated efficiency due to the shadow loss can be expressed as the sum of all the shadow zone areas over the area of the lens and therefore can be expressed as:

$$\eta_{\text{ring}} = 1 - \frac{\sum\limits_{n=1}^{N} 2\pi r_n r_t \sin\psi}{\pi R^2} \tag{3.26}$$

where r_n is the n$^{\text{th}}$ diffractive ring radius, r_t the SPDT diamond tool radius, R the lens semi-aperture and ψ the surface slope.

If it is assumed a quadratic diffractive lens the previous expression can be simplied to

$$\eta_{\text{lens}} = 1 - \frac{2\alpha r_t}{n_1 - n_2}\left(\frac{\alpha R^2}{\lambda_D} + 1\right), \tag{3.27}$$

where α is the optical power of the diffractive lens. The previous expression can also be formulated as a function of the NA. The NA can be approximated by the product of the radius R and the quadratic coefficient α. Therefore the previous expression can be written as

$$\eta_{\text{lens}} = 1 - \frac{2r_t}{n_1 - n_2}\left(\frac{\text{NA}^2}{\lambda_D} + \alpha.\right) \tag{3.28}$$

If the tool travels at a constant speed along the radius of the lens, the discontinuities cannot be machined perfectly. Instead, the tool path is a slope. Because the slope profile differs from the theoretical profile, the light passing through the slope region will not be diffracted as desired and therefore is lost. As previously, the amount of lost light is the ratio of the area of the lost zone over the area of the ring. Using the tool speeds radial v_r and SPDT maximum acceleration $a_{\max}$ can be expressed the integrated efficiency due to the machine response losses as the sum of all the lost area over the area of the lens and therefore can be expressed as

$$\eta_{\text{lens}} = 1 - \frac{2}{R^2} a_{\max}\left(\frac{\delta x}{v_r}\right)^2 \sum_{n=1}^{N} r_n. \tag{3.29}$$

As previously in the case of quadratic diffractive lens, the previous expression can be simplified as

$$\eta_{\text{lens}} = 1 - \frac{2}{R^2} a_{\max}\left(\frac{\delta x}{v_r}\right)^2 \sqrt{\frac{\lambda_D}{\alpha}} \sum_{n=1}^{N} \sqrt{n}, \tag{3.30}$$

with

$$N = \frac{R^2 \alpha}{\lambda_d}. \tag{3.31}$$

Modern SPDT machines reduce the tool feed-rate before the zone in order suppress this effect. Machine such as the Nanoform 700 from Precitech Inc. [111] actually stop the feed-rate before a diffractive zone. Hence, the machine impulse response is limited to some negligible over-shooting on the zone step.

SPDT evidently is a single point method. Therefore, along the radius, two consecutive tool positions create a high frequency residual profile. In order to evaluate the scattering, it is necessary to quantify the peak to valley error introduced by the machining. The peak to valley is estimated by finding the intersection point of two consecutive tool paths. In our case the tool geometry is hemispheric. It is assumed that the tool angle is zero and that the surface is linear between the two tool positions. The peak to valley function of the radius does not exhibit any discontinuity and contains mainly low spatial frequencies compare to the high spatial frequencies of the roughness generated by two consecutive tool positions. Therefore, it can assumed that the roughness profile is a nearly periodic profile. Therefore under the scalar approximation, the efficiency in the zero order due to the diffraction by the roughness profile can be estimated as

$$\eta(r) = \mathrm{sinc}^2\left(\frac{h_{PV}(r)(n_1 - n_2)}{\lambda}\right), \tag{3.32}$$

where h_{PV} is the height of the peak to valley error. Therefore, the efficiency of the surface can be estimated as

$$\eta = \frac{2}{R^2}\int\limits_0^R \eta(r) r dr. \tag{3.33}$$

The loss mechanisms strongly depend on the machine configuration and on the HAD geometry. The transmission efficiency is limited by a combination of the machine feed-rate, machine spindle speed, tool radius, surface slope, design wavelength and the machine impulse response

The machine feed-rate and spindle speed can be tuned easily and determine the radial spacing between two cuts. Therefore, the spindle speed is set to the highest possible value recommended by the manufacturer of the machine. For temperature stability, cycle times exceeding 20 minute should be avoided. The tool radius strongly influences the peak to valley [110]. On one hand, large tool radii reduce the local peak to valley error but increase the shadow zones. On the other hand, sharp tools strongly increases the peak to valley error Furthermore, in the case of broadband HAD, the peak to valley is multiplied by the refractive index difference. Therefore, even if the geometrical peak to valley is as high as $1\mu m$, it optically appears 50 times lower. Finally high surface slopes significantly reduce the local peak to valley error. More importantly, the transmission efficiency is a function of the NA and the radius of the lens. In fact, at equal NA, lenses with smaller radii exhibit a higher diffraction efficiency. However, at equal NA, the diffraction efficiency of HAD lenses is higher for small radii. In fact, smaller lenses have less diffractive rings, hence, the losses due to the shadow zone is smaller. The best trade-off of diffraction efficiency versus NA is for a system using an Step Diffractive Surface (SDS) [112].

3.2.3.3 Optical design using hybrid aspheric diffractive for hyper-chromatic application

An SDS is a HAD lens where the non-modulated diffractive profile is the inverse to the refractive profile as shown in Figure 3.26. Hence, SDS can be described by the following equation:

$$z(r) = z_{\text{ref}}(r) + \text{mod}(-z_{\text{ref}}(r), \delta z) \tag{3.34}$$

This immediately implies that the surface slope ψ in equation 3.26 is zero. Hence, HAD lenses do not exhibit shadow zone errors. The implication is that the tool radius can be optimised empirically to minimise the peak to valley error in equation 3.32.

As shown in figure 3.27 the diffraction efficiency of an SDS surface is superior to a classical and a broadband HAD surface. From a theoretical perspective, SDS lenses are the most appropriate structure for hyper-chromatic lenses required chromatic confocal sensing.

In order to evaluate the benefit of SDS lenses, a concave spherical SDS was

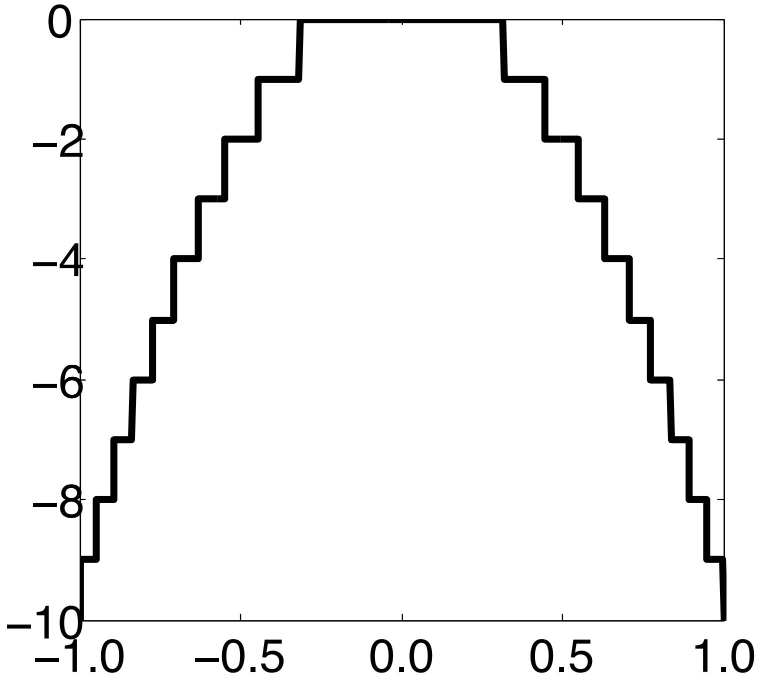

Figure 3.26: Profile of an SDS lens, the profile is simply consecutive steps of the height of the original diffractive profile. An SDS lens is powerless at the design wavelength

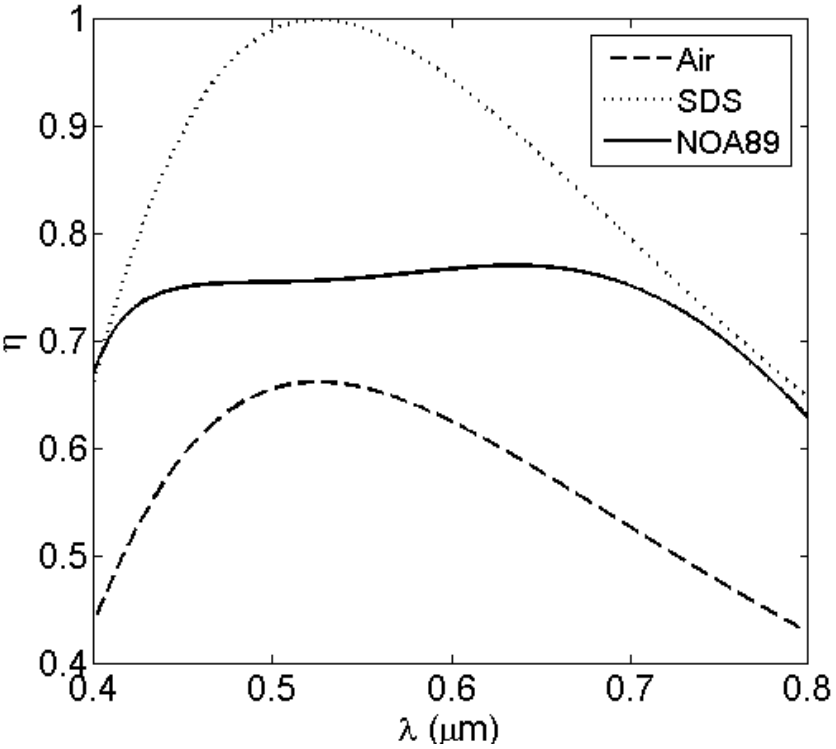

Figure 3.27: Efficiency of HAD lens, SDS lens of optical power of 0.005 mm^{-1} and a stack of 7 broadband HAD lenses equivalent to an optical power of 0.005 mm^{-1}. It appears that the SDS lenses offer the highest efficiency due to the low scattering losses, the low machine impulse response losses and no shadow zone losses.

machined. The radius is such that the outer ring interval is 5 μm. A 0.5 mm half radius natural diamond tool has been used. The surface was machined at a spindle speed of 10,000 rpm and a feed-rate of 1 mm/min.

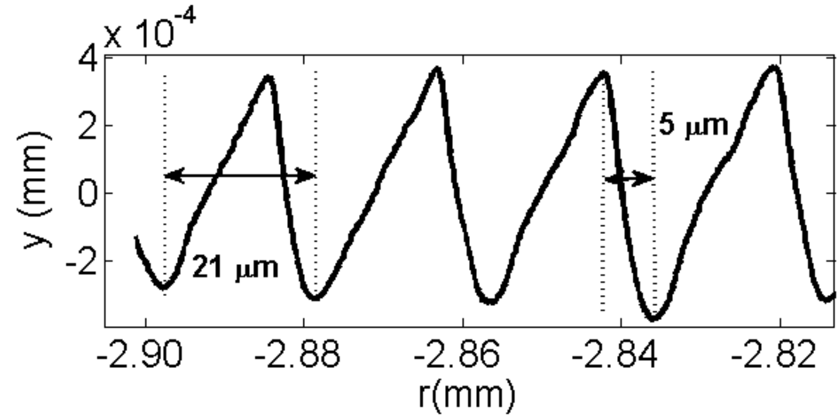

Figure 3.28: Diffractive profile of a HAD lens measured using a CCI white light interferometer. The shadow zone is 5 μm for a lens of ring size of 21 μm.

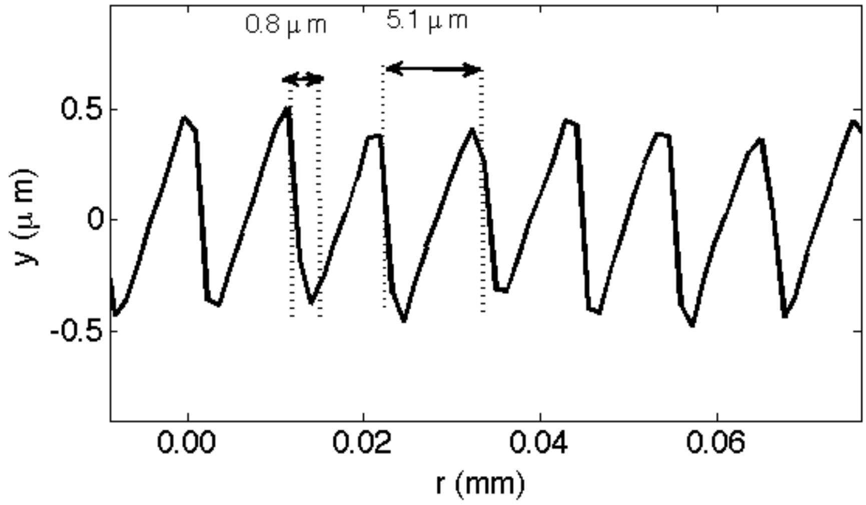

Figure 3.29: Diffractive profile of an SDS lens measured using a CCI white light interferometer. The shadow zone is 0.8 μm for a lens of ring size of 5 μm.

Figures 3.28 and 3.29 show that an SDS lens design has a shadow zone and machine response loss more than 5 times smaller than a HAD lens. In addition, SDS surfaces are more robust than their HAD equivalents. Figure 3.30 shows a HAD surface with a diffractive ring interval of 10 μm. HAD lens surface machining on plastic does not support fine structure due to material hardness limitation.

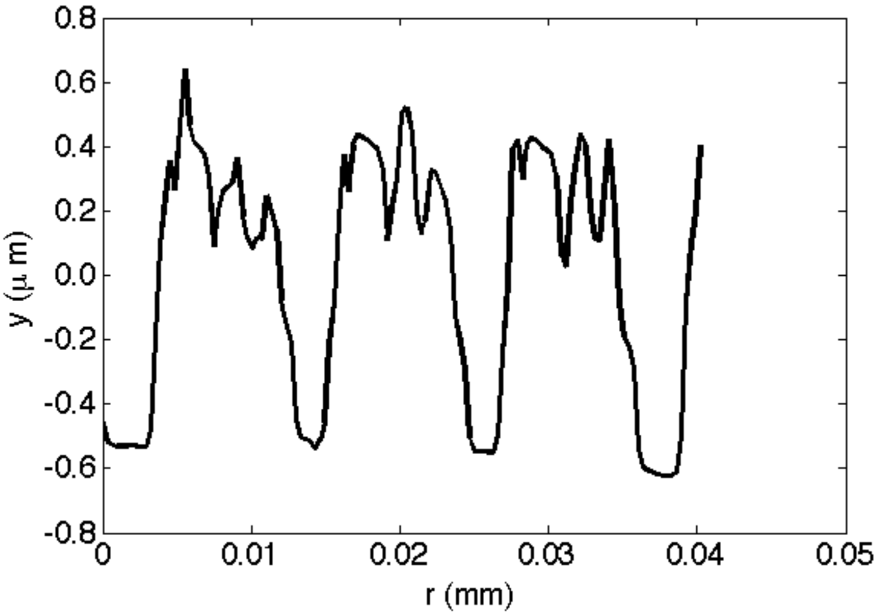

Figure 3.30: Quadratic HAD lenses with a ring width of around 10 μm. Due to the fine structure of HAD lenses, diffractive ring smaller than 10 μm suffers from high form error.

The HAD lens surface exhibits significant form variation at this scale resulting in a higher phase error. Using the SDS design, optical designs are now only limited by the computational method used. In fact, most software uses scalar diffraction theory to calculate ray propagation through diffractive objects. Therefore in the visible domain, the SDS outer ring interval should be restricted to at least 5 μm [113].

Table 3.5: Experimental relative chromatic confocal peak spectral irradiance of three comparable CCM optical heads using refractive, HAD, and SDS hyper-chromatic lenses. The peak response is normalised to the one of refractive technology

Hyper-chromatic technology	Relative efficiency
Refractive	1
HAD	0.15
SDS	0.83

To evaluate the manufacturability improvement of SDS over HAD lenses, the chromatic confocal peak spectral irradiance of HAD, SDS, and refractive hyper-chromatic technologies were measured. The measurement results are presented in Table 3.5. In order to measure comparable chromatic confocal peak

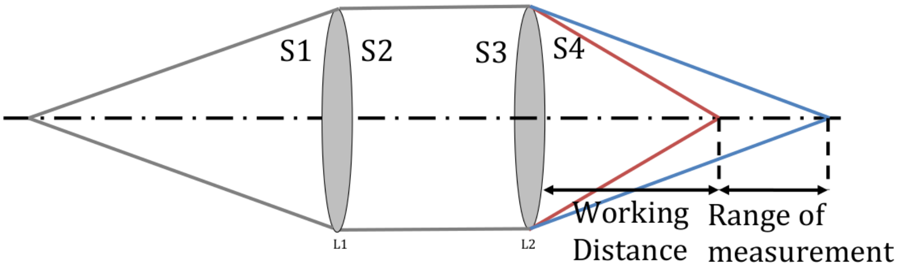

Figure 3.31: CCM optical head generic architecture. The entrance pinhole is placed on the left and surface to measure on the right. In the case of a HAD and SDS based CMM optical head, the diffractive surface is placed at the surface S3.

spectral irradiance, a generic optical layout of the CCM optical head has been used. The layout is presented in Figure 3.31. As expected, the chromatic confocal peak spectral irradiance of a CCM using an SDS lens is 5 times more efficient than for an equivalent design using a HAD lens. The SDS-based optical head is nearly as efficient as the refractive design. In addition, as a minor point, the lenses of the optical head using SDS lens were not coated unlike those of the refractive optical design.

3.2.3.4 Ray tracing model of hybrid aspheric diffractive surface

Optical design with HAD or SDS lenses cannot be performed in the same fashion as with classical refractive optics. Commercial ray tracing packages such as Zemax [114] or Code V [115] have implemented a diffractive surface capability by applying a scalar diffraction model and considering diffractive surface as a phase object with no thickness [116].

Ray tracing packages trace rays from surface to surface as shown in Figure 3.32 in 2 dimension for more clarity. Between surfaces, the direction cosine (l, m, n) is constant while the coordinates (x, y, z) change. When a surface is hit, the direction cosine (l, m, n) is changed. Ray tracing packages treat diffractive surface by calculating for a ray hitting the surface at a specific point the optical path difference δ_{binary} introduced by the surface and the gradient of the phase ϕ in Cartesian co-ordinates (x, y).

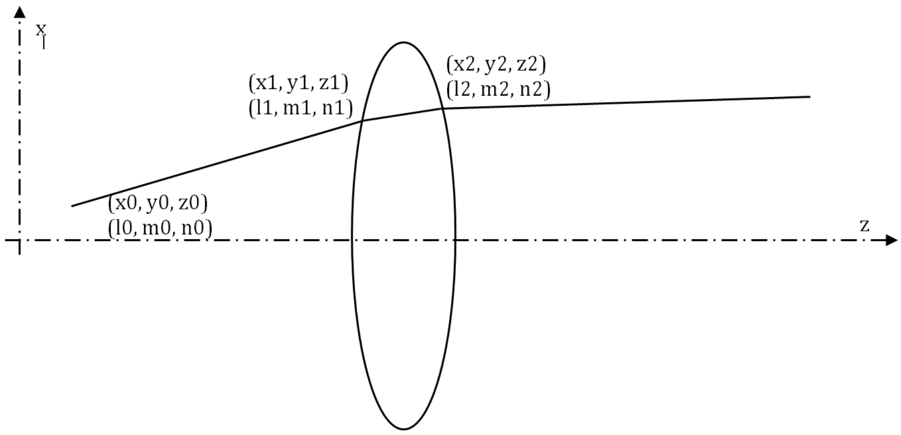

Figure 3.32: Sequencial ray tracing layout. A ray originating at (x0, y0, z0) with the direction cosine (l0, m0, n0) propagate until the first surface of the lens at (x1, y1, z1). The lens surface refract the ray to change the direction cosine to (l1, m1, n1).

The optical path difference δ_{binary} introduced by the surface is expressed as

$$\delta_{binary} = \frac{\lambda}{2\pi\, m} \sum_{i=1}^{k} \beta_i \left(\frac{r}{R_{norm}} \right)^i , \tag{3.35}$$

where β_i are the coefficients describing the surface phase profile, r is the radial coordinate of the surface and R_{norm} the normalised radius of the surface

The gradient of the phase ϕ in cartesian co-ordinates at the surface is expressed as

$$\begin{cases} \frac{\delta\phi}{\delta x} = \frac{\delta\phi}{\delta r}\frac{x}{r} \\ \frac{\delta\phi}{\delta y} = \frac{\delta\phi}{\delta r}\frac{y}{r} \end{cases} \tag{3.36}$$

Hence, the real diffractive surface profile z_{binary} to be manufactured is

$$z_{binary}(r) = \frac{\lambda_0}{2\pi(n(\lambda - 1)} \sum_{i=1}^{k} \beta_i \left(\frac{R_{norm}}{R} \right)^i \mathrm{mod} \left(\frac{\lambda_0}{n(\lambda_0) - 1} \right) \tag{3.37}$$

Equation 3.37 shows that important design and manufacturing parameters such as the design wavelength λ_0 are not considered during the design phase in the ray tracing package. In addition, aberrations specific to diffractive lens are ignored. Indeed, the phase difference introduced by the incident angle of ray to the surface is ignored. Therefore, a HAD user defined surface capability has to be build.

In a similar way, the optical path difference δ_{UDS} is defined as

$$\delta_{UDS} = \alpha_\theta(l,m,n)\,\frac{\lambda}{\lambda_0}\frac{p}{m}\sum_{i=1}^{k}\alpha_i\,r^i, \tag{3.38}$$

where α_i are the polynomial coefficients describing the phase profile of the lens. As mentioned previously, an off-normal incident angle of a ray onto the surface introduces a phase error. This effect is represented by the function $\alpha_\theta(l,m,n)$ calculated in the direction cosine [117] of a normal vector collinear to the incident ray. The function $\alpha_\theta(l,m,n)$ is defined as

$$\alpha_\theta(l,m,n) = \frac{1}{\cos\theta_i}, \tag{3.39}$$

where θ_i is the incident angle of the ray onto the surface in cylindrical coordinate system defined as

$$\theta_i = \arctan\left(\frac{\sqrt{l^2+m^2}}{n^2}\right) \tag{3.40}$$

In Equation 3.38, both the diffraction order m and the harmonic p are taken into account. In addition, the design wavelength λ_0 is directly incorporated at the ray tracing stage. In combination with the absence of radial normalisation R_{norm}, this approach gives direct knowledge of the optical power exhibited by the diffractive and thus the number of diffractive rings.

Hence, the real diffractive surface profile z_{UDS} to be manufactured for the user defined surface is expressed as

$$z_{UDS}(r) = \frac{1}{n(\lambda)-1}\sum_{i=1}^{N}\alpha_i\,r^i\text{mod}\left(\frac{\lambda_0}{n(\lambda_0)-1}\right). \tag{3.41}$$

The latter method is simpler to implement in the ray trace package but yet more precise in the description of HAD surfaces. If it is assume that the manufacturing method is SPDT, the efficiency of the manufactured surface can be implemented in the user defined surface. The efficiency described in Equations 3.22, 3.26 and 3.32 are implemented. Thus, not only can the phase profile can optimised during the design process of a HAD but also the manufacturing parameters such as the diamond tool radius and machine feed-rate.

3.2.4 Wavelength analyser

The aim of a wavelength analysis is to determine the surface height by measuring the wavelength reflected off the surface. Using a classical spectrometer, the peak wavelength is measured on a line sensor. The line sensor can be a CCD or a CMOS. The spectrometer used can have various configurations in terms of transmission or reflection and use various wavelength selection elements such as Linear Variable Filter (LVF) or Diffraction grating. Other spectrometer configurations such as Fourier Transform Spectrometer (FTS) or Fabry Perot spectrometer are also potential solution.

3.2.4.1 Linear variable filters

A linear variable filter is a thin film optical interference filter [118]. The filter can be high pass, low pass or band pass. The specificity of a LVF is that the cutting frequency is variable along the filter. Typically, high and low pass filter consist of groups of alternate high and low index quarter-wave filters, with each such group having a unique design wavelength. Bandpass filters typically consist of pairs of such groups on either side of the half-wave “resonator” layer. Especially, the finesse is defined by these groups while the bandpass location is defined by the resonator layer thickness.

The concept of an LVF is to tune the entire multi-layer to make the transmitted wavelength variable on one axis of the substrate. The LVF is placed in front of a light position sensitive detector such as a CCD, the measured spectral irradiance is a representation of the spectrum.

3.2.4.2 Diffraction gratings

A grating is a periodic diffractive element which modifies the direction of the incident light as a function of the wavelength. In other words, a spectral transformation is made.

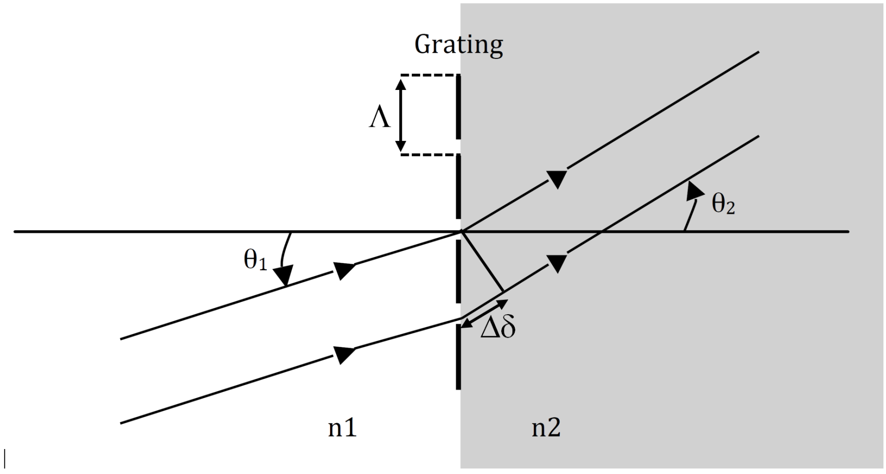

Figure 3.33: Diffraction grating interference principle illustrated with 2 rays.

As shown in Figure 3.33, two rays passing through two consecutive slits of the grating will exhibit an optical path difference which can be expressed as [13, p. 5.4]

$$\Delta\delta = n_2 \Lambda \sin\theta_2 - n_1 \Lambda \sin\theta_1, \tag{3.42}$$

where Λ is the grating period. Constructive interference will appear only when the optical path difference is a multiple of the illumination wavelength, hence [13, p. 5.4]:

$$m\lambda = n_2 \Lambda \sin\theta_2 - n_1 \Lambda \sin\theta_1, \tag{3.43}$$

Several grating types are widely available, such as:

- Transmission rules grating
- Ruled reflective grating
- Holographic reflective grating
- Echelle grating.
- Volume holographic grating.

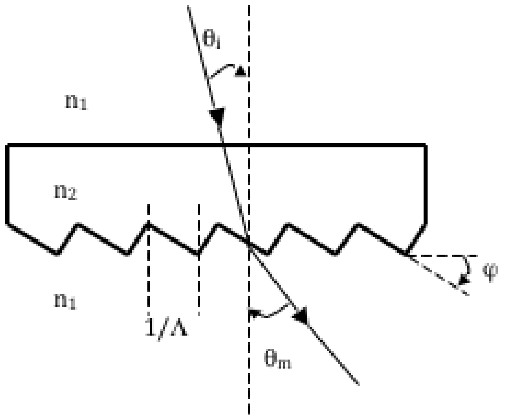

Figure 3.34: Blazed transmission diffraction grating geometry.

Blazed gratings, as shown in Figure 3.34, have a sawtooth profile and exhibit a high diffraction efficiency at the design wavelength for a medium grating period. Nevertheless, due to the manufacturing process, it is difficult to reach a high grating period. In addition, the diffraction efficiency decreases significantly as the grating period increases. Another problem with ruled gratings is the periodicity error which leads to ghosting [119, p. 211].

Transmission gratings allow the design of a simple optical system using achromatic lenses while reflection gratings permit the construction of a spectrometer that is both inexpensive and compact.

Holographic gratings exhibit a phase sinusoidal profile. The manufacturing process offers a high repeatability which leads to low ghosting and scattering. The downside is that the diffraction efficiency is significantly lower than with ruled grating. Nevertheless, high grating periods up to 3,600 lines/mm can be achieved [119, p. 81].

Volume Holographic Gratings (VHGs) are sinusoidal Bragg gratings recorded holographically. They offer high diffraction efficiency with low ghosting, low scattering, and a high period of 1,800 lines/mm. However, because VHG are recorded on photosensitive gelatine and then sealed, their unit cost is high at around £500 and a lifetime of a few years in humid environment[p. 346] [119].

3.2.4.3 The line sensor

The relevant line sensors are either CMOS or CCD. A marginal technology for our application is a position sensitive detector.

For a CCD, each charge of each pixel is transferred to be converted by a single charge amplifier. On the other hand for a CMOS, each pixel charge is individually converted by a separated electron to voltage converter [120]. CMOS offers clear embedded system advantages such as small packaging and low power consumption. Nevertheless, the SNR is often limited. Finally, due to the parallel electron to voltage conversion, the sensor speed can be theoretically higher and only a part of the sensor can be read [120]. CCD offers clear advantages toward image quality.

It could therefore appear that the CCD is the natural choice for our application. However, when price enters into the decision process, this obvious choice disappears. A CMOS sensor can offer a better image quality than a CCD sensor with a similar price. In fact, CCD and CMOS exhibit different volume discount characteristics. Finally, at line reading rate of a several kHz, CCDs suffer from a bottle neck effect at the electron to voltage conversion. This can lead to higher noise at full speed compared to a CMOS sensor. The limitation of both CMOS and CCD are the sensitivity, dynamic range and response time compare to a photo-diodes. Therefore, other photo-diode based wavelength analyser configurations using FTS or Fabry Perot spectrometer are attractive.

3.2.4.4 Fourier Transform Spectrometer

The Fourier transform of the spectra is measured by recording the interference pattern over the coherence length of the source. The basic setup is similar to a Michelson interferometer as shown in Figure 3.35

A typical confocal peak is 10nm wide. The coherence length of a source with a Gaussian spectral profile can be estimated using the following formula [122, p. 30];

$$L_{coh} = 0.66\frac{\lambda^2}{\Delta\lambda} \tag{3.44}$$

Hence, a chromatic confocal peak of 10 nm centered at around 550 nm has a

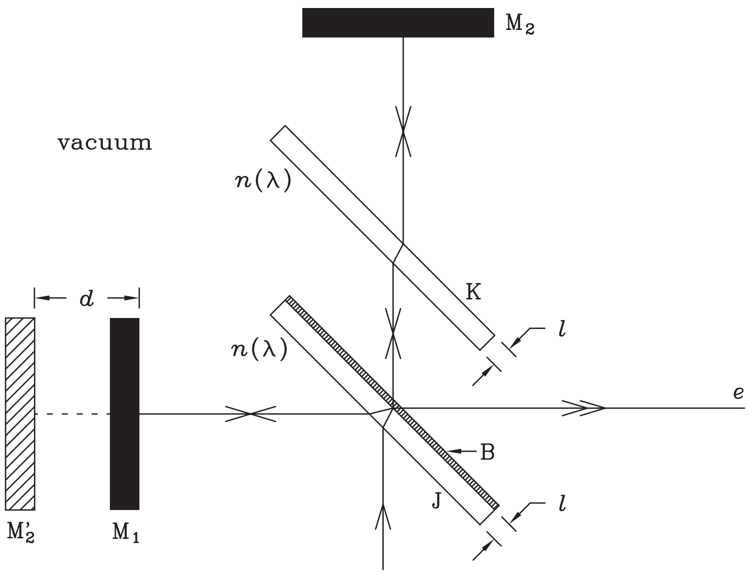

Figure 3.35: Basic principal of a Michelson interferometer. $M'2$ is the transpose of the $M2$ in the arm of M1. The Fourier transform of the spectra is measured by recording the interference pattern of a source over the full coherence length. The coherence length is scanned throughout the distance d. [121]

coherence length of 100 μm. Hence, the distance d needs to be increased by 50 μm to scan the full coherence length of the source. To be competitive against a grating based wavelength analyser, the scanning rate should be of the order of 10 kHz. This can only be achieved by an electro-optic modulator. However, for cost reasons, this solution is not viable. Another approach is to use a mirror mounted on a piezoelectric transducer. The current state of the art in piezoelectric transducer does not allow such displacement at 10 kHz. At 10 kHz, the achievable displacement is 500 nm. This mirror displacement corresponds to approximately two waves and is a fraction of the coherence length. Due to Parseval's theorem [123, p. 217], the majority of the peak information is lost. Despite this loss of information only the central frequency of the peak is of interest. In fact, if the distance d oscillates around zero, only the central frequency is observed. To estimate the DNR of such a spectrometer, the output signal of a FTS has been simulated for a Gaussian peak of 10nm FWHM centered at 550 nm. The signal is modelled as

$$S_{FTS} = exp\left(-\frac{\Delta\lambda\, d}{0.56\,\lambda^2}\right)\sin\left(\pi\frac{d}{\lambda}\right) + X(\delta, \sigma_{noise}), \tag{3.45}$$

where $X(d, \sigma_{noise})$ is a Gaussian distributed noise of standard deviation σ_{noise}.

The frequency of the measured sinus cannot be determined in the Fourier domain precisely due the low windowing. Another approach is to use a single tone detector. The chosen algorithm is based on a autoregressive filter [124]. The signal described in equation 3.45 is generated 1000 times with a SNR of 42 dB.

The DNR is estimated at 10,000. The DNR of the FTS is 3 times smaller than the one measured in Section 2.3. This low DNR is related to the instability of the single tone estimator as shown in Figure 3.36.

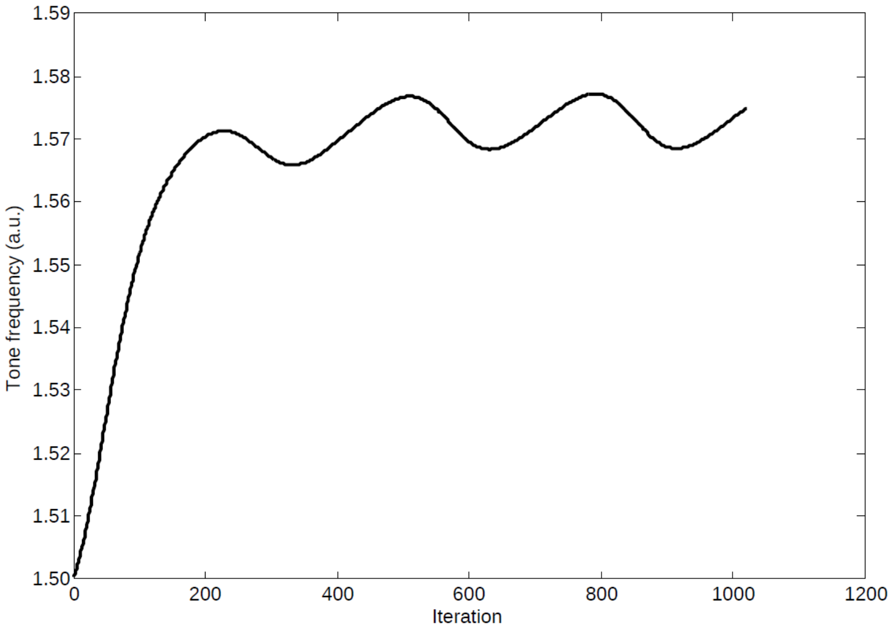

Figure 3.36: Convergence of the autoregressive algorithm for single tone detection. The algorithm is converging but oscillates.

The oscillating convergence is due to the Gaussian modulation of the sinusoidal signal. The single tone estimator searches for a pure sinusoidal signal, while in our case the sinusoidal signal is multiplied with a Gaussian envelope corresponding to the coherence length of the source. Hence, the observed frequency is not constant.

Thus, the FTS spectrometer is not suitable for the application. However, in the case of a FTS the dynamic range is defined as ratio of the source spectral range over the frequency uncertainty. Thus, if the source spectral range increases, the dynamic range increases.

3.2.4.5 Alternative design

An alternative to a spectrometer is a monochromator. Instead of measuring the reflected wavelength, an initial wavelength-scan is made. By synchronising this to a photo-diode detector the position of the surface can be determined.

Another alternative is to use a 2D image sensor. The grating needs to diffract the light over 2 dimensions. This can be achieved by using an echelle spectrometer or a rotationally symmetric grating. These two approaches greatly increase the dynamic range of the spectrometer. In fact, the DNR is more a less squared. However, the light level is reduced. The light is spread over an area rather than an line. The light level is therefore divided by the area of the sensor. It becomes now less obvious if the use of 2D sensor increases the dynamic range.

3.3 Design of a low cost version chromatic confocal microscope

The first system to be designed is a low cost version of the chromatic confocal microscope. The specifications are detailed in Table 3.6.

In order to design such a system, the most suitable technologies for each level 3 sub-system of the WBS described in Section 3.2 are first identified.

The first step is to choose which technology can be used. It can be difficult to compare different technologies together. In fact some characteristics such as spectral domain, spectrum continuity, manufacturability are non-numerical and are sometimes too different to be compared together. The chosen approach is to select several important characteristics for each level 3 sub-system. Each characteristic is weighted with the weights being normalised. Each technology is then associated with a score for these characteristics which ranges from 0 to 10. For example, if one characteristic is the spectrum continuity, a mercury low pressure lamp would score 0 while a black body source would score 10. All the scores are weighted and summed up. The technology with the highest score will be the selected one.

Table 3.6: Target specifications of the low cost version of the CCM

	Value	Unit
Working distance	> 20	mm
Range of measurement	≈ 7	mm
Resolution[1]	100	nm
Linearity	1	μm
Maximum measurement rate[2]	500	Hz
θ_{max} [3]	≈ 7	°
Spot size	≈ 30	μm
Thermal stability	<1	$\mu m/°C$
Head diameter	8	mm
Fixed material cost[4]	500	£

[1] : Defined as k=3 time the measurement standard deviation σ_{N-1} at a measurement rate of 5 Hz. The standard deviation is calculated using N=200 samples as in Equation 1.2.
[2] : The signal level must be at least 50 % on a polished metal target.
[3] : Maximum measurable surface tilt for a polished target. [4] : For 10 batches of 50 units per year.

3.3.1 The light source

The most important characteristic for such a system is the cost. In fact, a high luminous flux source requires an expensive power supply and a heat management system. Additionally, a long lifetime is a requirement. In fact, the product should have a low maintenance cost. A large spectral range is also essential considering the required range of measurement 7 mm. In Table 3.7, the relevant characteristics are weighted and a score is set to each technology. Table 3.7 highlights that the most relevant source for a low cost CCM is a LED.

3.3.2 The light splitter

Again, cost is the most important characteristic followed by the complexity of the system. A cost-effective solution has to consider the cost implication of the full system. The light circulator bandpass should also match the corresponding light source. Finally, light efficiency must be sufficient to reach a sampling frequency of 500 Hz and be polarisation independent due to the non-polarised nature of the chosen source as well as the polarisation impact of the measured surface [125].

Table 3.7: Comparison of the suitable light source for a CCM

	Weight	Discharge lamp	SLED	Supercontinuum laser	LED
Cost	0.2	6	2	0	10
Luminous flux	0.1	6	6	8	4
Numerical Aperture	0.1	2	8	8	4
Spectral range	0.12	10	3	10	6
Spectral Domain	0.1	10	4	8	8
Lifetime	0.12	6	6	4	10
Heat dissipation	0.08	0	8	4	10
Power consumption	0.08	1	6	0	10
Size	0.1	6	8	0	10
Score	1.0	5.72	5.36	4.56	7.92

Table 3.8: Comparison of the suitable light splitter for a chromatic confocal microscope

	Weight	Fibre optic circulator	Broadband fibre coupler	Telecom fibre coupler	Beam splitter
Cost	0.5	2	3	9	4
Complexity	0.2	9	9	9	2
Band pass	0.1	7	7	3	8
Efficiency	0.1	8	8	5	10
Polarisation dependency	0.1	7	7	7	2
Score	1	5	5.5	7.8	4.4

The telecom fibre coupler is by far the best solution. In fact, the low cost and simplicity make it an extremely attractive solution. The selected telecom fibre coupler has a core diameter 62.5 μm and an NA of 0.2.

3.3.3 Optical head design

The design of the optical head is probably the most critical phase of the design of the CCM. It has been identified in Section 3.3.3 that the most suitable hyper-chromatic technology is a SDS lens manufactured using SPDT.

The optical design of the confocal head is based upon the target specifications of the system. The relevant parameters are the working distance of 20 mm, the tube outer-diameter of 8 mm, the range of measurement of 7 mm, the spot size of 30 μm, and the maximum surface slope of 7°.

Some information is redundant. If the outer diameter of the tube must be 8 mm, the lens pupil should be around 6 mm. Therefore, if the working distance is at the minimum of 20 mm, the maximum surface slope is between 8° at the beginning of the measurement range and 6° at the end of the range. Despite this contradiction, the maximum surface slope is flexible and is not a critical factor.

Thermal stability of a CCM optical head is crucial. If the range of measurement is translated or even distorted with temperature variation, the technology is no longer a viable solution. A passive method has been developed when using refractive lens [80] and active when using GRIN lenses [68]. However, the thermal dispersion of diffractive lenses is often used to athermize optical design [74]. Hence, a SDS surface can potentially athermize the optical design.

Several lens configurations are viable when designing a CCM optical head in the visible domain. The first and simplest configuration is to use two plastic lenses manufactured using SPDT machining. The second approach is to mold in glass two lenses with mold manufactured using SPDT manufacturing. The third configuration is described in Figure 3.37 where two refractive glass lenses are used with a plastic SDS lens manufactured using SPDT machining. These three configurations are modelled thermally.

Table 3.9: Thermal drift coefficients of three design of the low cost version of the CCM between 15 $°C$ and 35 $°C$.

Design version	Thermal error coefficient
Full plastic	21 $\mu m/K$ or 0.3 $\%/K^*$
Full glass	0.056 $\mu m/K$ or 8.10 $^{-4}\%/K^*$
Hybrid glass/plastic	0.66 $\mu m/K$ or or 10 $^{-2}\%/K^*$

* : in percentage of the measurement range

The thermal error coefficients in Table 3.9 have been calculated in Zemax by changing the environment temperature, then the focus drift is calculated. Zemax takes into account the change in refractive index as well as the thermal expansion of the optical elements and of the mechanical housing. The results in Table 3.9 shows that the most stable solution is the full glass approach. As a matter of fact, the system can be considered fully athermised. The thermal stability is comparable to the Renishaw RLE fibre optic laser encoder [126] and more than one order of magnitude lower than the Solartron Metrology Ltd inductive gauge [127]. This figures could even be improved by an order of magnitude with an active temperature compensation. However, the manufacturing process must be flexible to allow several optical design iterations to allow for realistic development. Because plastic SDS can either be moulded or machined, such lens are more suitable than glass SDS which can only be moulded.

The optical architecture uses a first achromatic lens L1 to collimate the fibre output, a plastic SDS lens L2 to create the chromatic aberrations, and finally, a second achromatic lens L3 to focus the light beam onto the surface as shown in Figure 3.37. This hybrid glass-plastic structure is sufficiently stable with the temperature to reach the target specification as shown in Table 3.9. An additional, protection window can be added to protect the optical system.

The optical power of an SDS is null at the design wavelength. Thus, the SDS can be ignored when determining the focal length of the achromatic lens L1 and L3. The spot size is defined as the image of the pinhole by the optical head. Therefore, the spot size radius R_{spot} is defined as the product of the pinhole radius R_p multiplied by the magnification M. If it is assumed that the core radius R_p of the fibre coupler

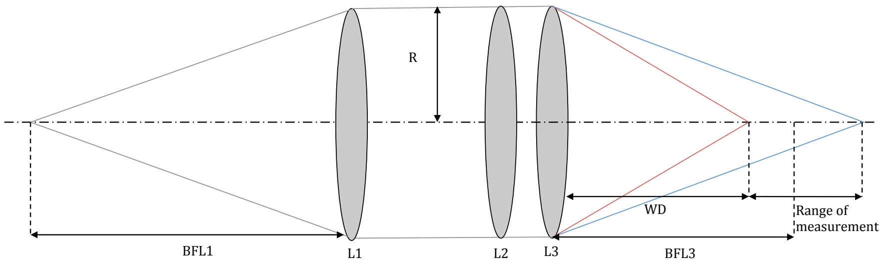

Figure 3.37: Schematic of the optical head design. The lens L1 collimates the light beam from the fibre coupler. L2 then generates the chromatic aberration due to the SDS surface. Finally, L3 focusses the collimated light to create the range of measurement at the working distance WD. Because the lens L2 is powerless at the design wavelength, the mid-range point is at the back focal length BFL3 of the lens L3.

chosen in Section 3.3.2 is 25 μm, then the magnification M of the system is 1. The magnification M of the system is defined as

$$M = \frac{F_{L2}}{F_{L1}} = 1, \tag{3.46}$$

thus, $F_{L2} = F_{L1}$. To reach the working distance of more than 20 mm, the back focal length at the design wavelength of L3 must be 23.5 mm. An off-the-shelf achromatic of diameter 6 mm and back focal length of 28 mm has been selected.

The optical system was then modelled on a ray tracing software for instance Zemax. The HAD surface profile of the lens L2 was then optimised to create the range of measurement and correct for the geometrical aberrations. After optimisation, the magnification was calculated to be 0.7 and the measurement working distance 25.6 mm. Thus, the spot size is now 35 μm.

3.3.4 Wavelength analyser

The design of the wavelength analyser is a two step process. First, the most suitable dispersive element is identified. Then, the optical system of the wavelength analyser is designed.

3.3.4.1 Identification of the most suitable dispersive element.

The wavelength analyser must be designed to match the wavelength range of the source. It has been identified in section 3.3.1 that the most suitable light source is a white light LED. Therefore, the wavelength analyser must cover a wavelength range from 400 nm to 800 nm. The most important component of the wavelength analyser is the dispersive element. The sub-system design is dependant on the type of the dispersive element. The relevant parameters for the wavelength analyser are the price, diffraction efficiency, system complexity, system size, and volume capability. The price and the light throughput efficiency are the most important parameters. In fact, light throughput efficiency is essential for the system. The light throughput efficiency must be maximised. The system complexity relates to the type of optical system which can be designed around the dispersive element. With an LVF, the system design is a simple illumination problem, while for a reflection ruled grating, off-axis optical design is necessary.

Table 3.10: Dispersion element technology comparison for a low cost version of the chromatic confocal microscope

	Weight	LVF	Transmission ruled grating	Reflection ruled grating	Reflection holographic grating	Volume holographic grating
Price	0.3	8	5	5	5	2
Diffraction efficiency	0.3	1	7	6	6	9
System complexity	0.2	8	7	4	4	7
System size	0.1	8	6	9	9	6
Volume capability	0.1	9	6	6	7	3
Score	1	6	6.2	5.6	5.7	5.7

It appears from Table 3.10 that the most suitable dispersive element is the transmission ruled grating followed closely by the LVF. In a first design iteration, the diffraction efficiency weighting has been underestimated. An LVF wavelength analyser has been designed but the light level was not high enough to reach the target measurement rate of 500 Hz. Nevertheless, the simple design and low volume cost might make this system interesting in the future for an entry price product.

3.3.4.2 Design of the wavelength analyser.

When produced, the wavelength analyser will be assembled by a work force with low optical expertise. Therefore, a transmission design was chosen. In fact, a transmission wavelength analyser is simple to align and assemble.

The wavelength analyser is the last part of the system. Thus, it must be designed to achieve the target measurement performances of 100 nm of resolution and 1 μm of linearity. One of these two target performance criteria limits the system or may be contradictory. Therefore, the limiting target performances must be identified. To do so, the required dispersion $\delta z/\delta p$ to reach the linearity and the resolution will be calculated individually.

A target resolution of 100 nm is desired at 5 Hz. However, the maximum measurement rate is 500 Hz. Therefore, the measurement at 5 Hz is averaged 10 times from a higher sampling speed. Thus, the resolution $U_{res}(z)$ can be expressed as

$$U_{res}(z) = \frac{\sigma_z \, k_e}{\sqrt{N}}, \tag{3.47}$$

where σ_z is the standard deviation of measurement, k_e is a constant extending the level of confidence, and N is the number of averaged samples through time.

To know if the system can reach the resolution of 100 nm , Equation 3.13 and Equation 3.47 can be re-written as

$$\frac{\delta z}{\delta p} \geq \left(\frac{\sigma_z \sqrt{n}}{k_e \, \sigma_{CCD}} \right)^2 \frac{1}{\mathrm{FWHM}_z}. \tag{3.48}$$

Equation 3.48 assumes that the dispersion $\delta z/\delta p$ is linear and the peak spectral irradiance I is equal to 1.

If it is assumed that the peak signal is at its maximum at 200 Hz, the number of averaged samples N is equal to 50. In addition, k_e is equal to 3 to achieve a degree of confidence of 99.7 % [3]. Using the optical parameters from Section 3.3.3

and using Equation 3.4 the FWHM of the confocal peak is equal to 299 μm. The chosen CCD line sensor is the TCD1205DG from Toshiba [128]. The TCD1205DG is a 2048 pixels line sensor with a pixel height of 200 μm and 14 μm width. The datasheet specifies a saturation voltage of 0.8 V and a dark signal of 2 mV. Thus, the normalised CCD noise standard deviation σ_{CCD} is equal 0.0025. Therefore, the dispersion $\delta z/\delta p$ must be below 24 μm/pixel.

To reach the linearity $\Delta\mu$ of 1μm, the dispersion $\delta z/\delta p$ must be optimised. In fact, Equation 3.14 does not have an analytical solution. It has been found numerically that to reach a linearity $\Delta\mu$ of 1 μm the dispersion $\delta z/\delta p$ must be below 37 μm/pixel.

In summary, to reach the target linearity and resolution, the dispersion $\delta z/\delta p$ must be below 24 μm/pixel. To ensure that the system could reach the target resolution, it has been decided to reduce the numerical value of the target resolution by 30 %. The associated dispersion $\delta z/\delta p$ is then 12 μm/pixel. The used spectral range of the source was reduced to 300 nm between 400 nm and 700 nm to ensure the 7 mm of measurement range. Hence, the spectrometer uses 600 pixels between 400 nm and 700 nm. Thus, the spectrometer spectral dispersion $\delta\lambda/\delta p$ is 0.5 nm/pixel.

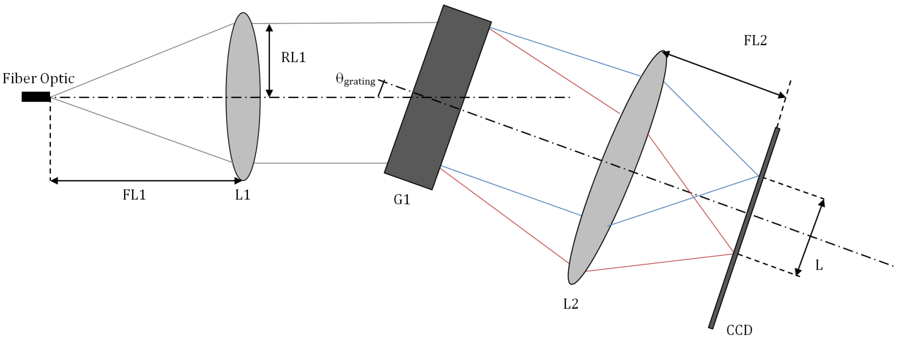

Figure 3.38: Wavelength analyser schematic. The design use two achromatic lenses L1 and L2 to respectively collimate and image to incident light. The grating G1 is tilted by an angle $\theta_{grating}$ with the optical axis of L1.

The chosen spectrometer design is described in Figure 3.38. The lens L1 collimates the light from the fibre circulator. The grating G1 is tilted by an angle $\theta_{grating}$ compared to the optical axis of the lens L1. The lens L2 is tilted at the same angle as the grating G1. The angle $\theta_{grating}$ is calculated using Equation 3.43

and with the condition that the diffraction angle at 400 nm is opposite to the diffraction angle at 700 nm. A spectrometer impulse response of 7 pixels is chosen to not significantly distort the measured peak. The focal length of the lenses L1 and L2 are respectively calculated to be 46 mm and 24 mm. Off-the-shelf achromatic lenses of 50 mm and 25 mm were selected from a catalogue.

3.3.5 Numerical performance estimation

The previously design system is summarised in Figure 3.39. To evaluate more precisely the expected performance of the system, the ray tracing data from the optical head and the wavelength analyser were analysed numerically by using the chromatic confocal peak theoretical model of Equation 3.3 and the resolution estimation described in Equation 3.13.

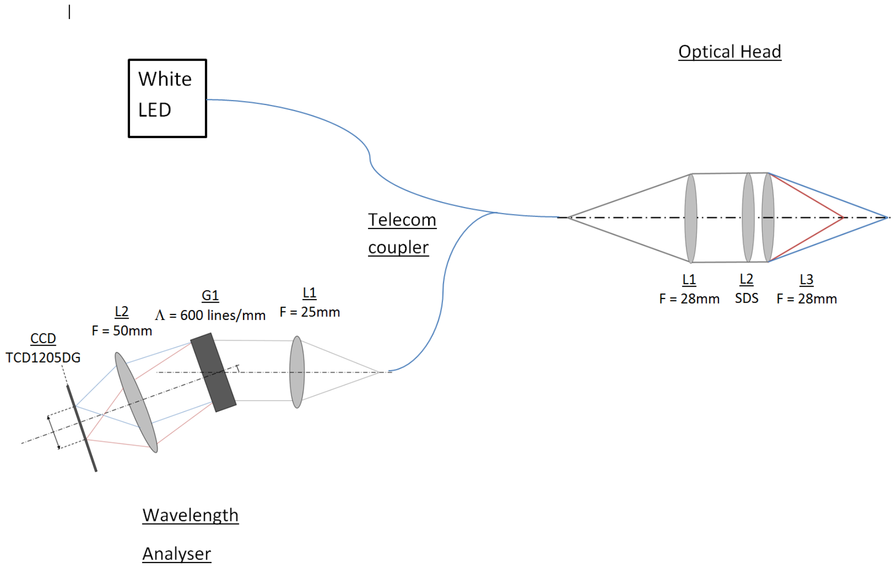

Figure 3.39: System layout of the low cost version of the chromatic confocal microscope.

Using the basic geometric data, the focus position as a function of wavelength is shown in Figure 3.40. As expected, the focus positions are nearly a linear function of the wavelength.

Using the useful aperture calculated on the ray tracing model of the optical head and the focus position, the maximum measurable surface slope was calculated as shown in Figure 3.41. The values are below the target of 7° but are still acceptable.

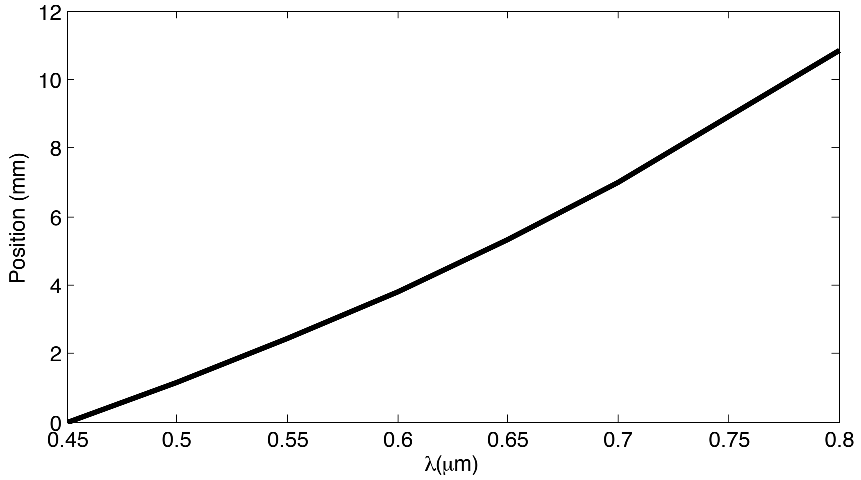

Figure 3.40: Focus position function of the illumination wavelength for the low cost version of the CCM. As expected, the focus position function is nearly linear.

The maximum measurable surface slope decreases with the focus position due to the reduction of NA.

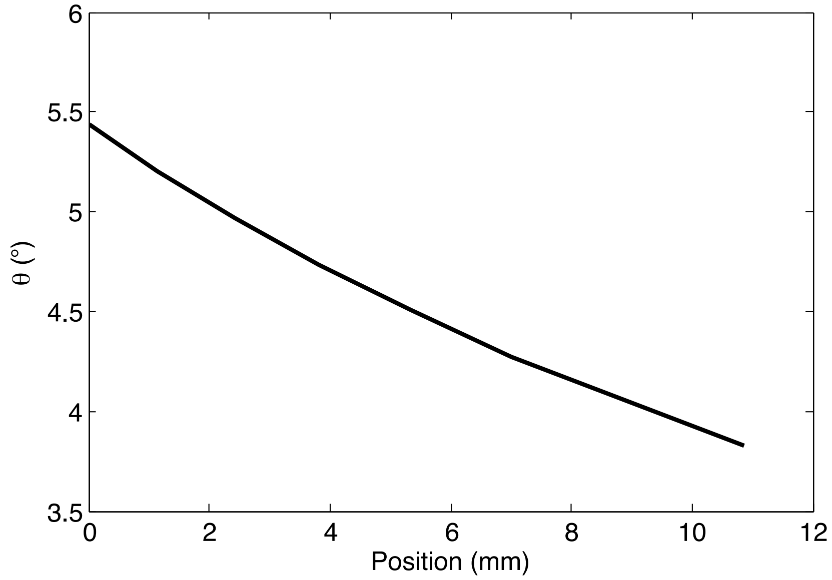

Figure 3.41: Maximum surface slope measurable by the low cost version of the CCM as a function of the illumination focus position. The measurable surface slopes are below 5.5° and reduce with the focus position.

Chromatic confocal peaks are calculated in the spatial space z using Equation 3.3 and converted in the wavelength space λ using the linearisation curve calculated in Figure 3.40 as shown in Figure 3.42. Since the wavelength analyser dispersion can be assumed to be linear, the chromatic confocal peaks in the wavelength space

λ, shown in Figure 3.42 are as observed by the wavelength analyser.

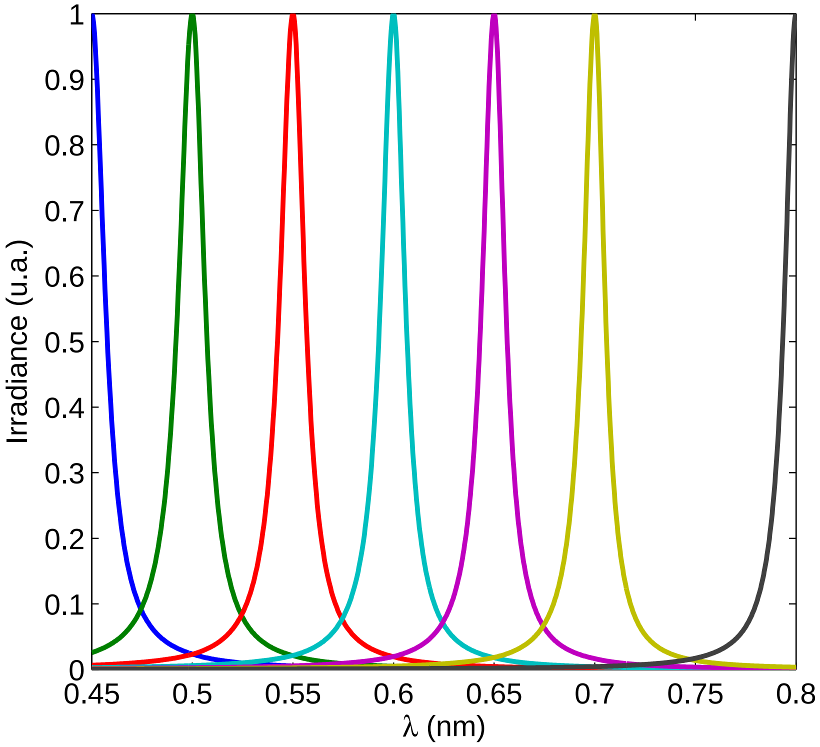

Figure 3.42: Several chromatic confocal peaks in the wavelength space of the low cost version of the chromatic confocal peak. The peak shape is visually maintained within the full spectral range.

By using the wavelength analyser dispersion of 50 nm/pixel calculated in Section 3.3.4.2, the chromatic confocal peaks in Figure 3.42 are converted to pixels rather than wavelength. Thus, Equation 3.12 can be applied to calculate the resolution in pixels. Then, the same procedure is applied backwards; the wavelength analyser dispersion and the optical head local dispersion are used to convert the calculated resolution from pixel to a metric unit. The calculated measurement resolution function of the range without averaging is shown in Figure 3.43.

The results in Figure 3.43 indicate that the resolution deteriorates with the position within the range of measurement. In fact, as indicated by Equation 3.4, the chromatic confocal peak FWHM is directly proportional to the distance from the optical head to the surface z_s. The worth resolution than calculated in Section 3.3.4.2 can be explained by the low NA of the optical head. In fact, during the

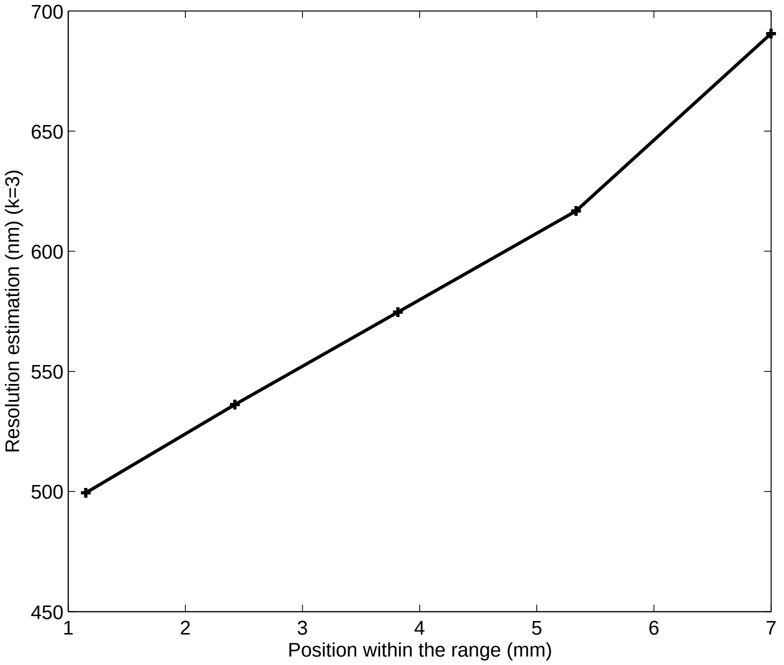

Figure 3.43: Numerically estimated resolution without a sample averaging function of the position within the range measurement of the low cost version of the chromatic confocal microscope. The resolution deteriorates with the position within the range of measurement due to the increasing chromatic confocal peak FWHM.

wavelength analyser design in Section 3.3.4.2, the optical head pupil diameter is considered to be 6 mm at the working distance of 25.6 mm while the ray tracing model suggests a useful aperture of around 5 mm at 25.6 mm. In addition, the resolution is calculated at the beginning of the range without considering the increase of the chromatic confocal peak FWHM throughput the range of measurement.

3.4 Design of a high resolution chromatic confocal microscope

The second system to be designed was a high resolution CCM. The aim of this CCM was to provide a resolution better than 10 nm over a minimum range of measurement of 50 μm at a measurement rate of 200 Hz. In addition, it is preferred that the maximum measurable surface slope exceed 30° and the working distance is at least 12 mm. For development cost reasons, this chromatic confocal microscope must use the off-the-shelf chromatic confocal wavelength analyser IFC2451 from Micro-Epsilon Gmbh [65]. An experimental evaluation had shown that the IFC2451 chromatic confocal wavelength analyser exhibits a spectral dispersion of 0.78 $nm/pixel$ over 512 pixels with a line sensor normalised noise standard deviation of 0.00016. The target specifications are sum up in Table 3.11.

Table 3.11: Target specifications of the high resolution version of the CCM

	Value	Unit
Working distance	>12	mm
Range of measurement	>50	μm
Resolution[1]	$\approx$ 10	nm
θ_{max} [2]	>30	°
Maximum measurement rate[3]	200	Hz

[1] : Defined as k=3 time the measurement standard deviation σ_{N-1} at a measurement rate of 5 Hz. The standard deviation is calculated using N=200 samples as in Equation 1.2.
[2] : Maximum measurable surface tilt for a polished target.
[3] : The signal level must be at least 50 % on a polished metal target.

The simplest procedure to achieve such a high resolution is to reduce the measurement range. In fact, the target measurement range of 50 μm is not challenging as this is equivalent to a dynamic range of 5,000 at the resolution of 10 nm. The major difficulty is the need for a working distance of 12 mm. With a working distance of 12 mm, the FWHM of the confocal peaks tend to increase. In addition, it is difficult to reduce the range of measurement to 50 μm. In fact, the minimum achievable measurement range is 250 μm. In Equation 3.13, the FWHM can only be partially reduced, the wavelength dispersion as well as the CCD noise are fixed and only the head dispersion can be tuned. Thus, the design procedure is to make the optical head dispersion non-linear, asymptotic to zero.

Due to the non-linearity of the dispersion curve, the design method used in Section 3.3 is not applicable. The design method for this optical head will be purely numerical using ray-tracing data, the theoretical confocal peak, and analytical measurement uncertainty.

The architecture of the optical head is the same as the one described in Figure

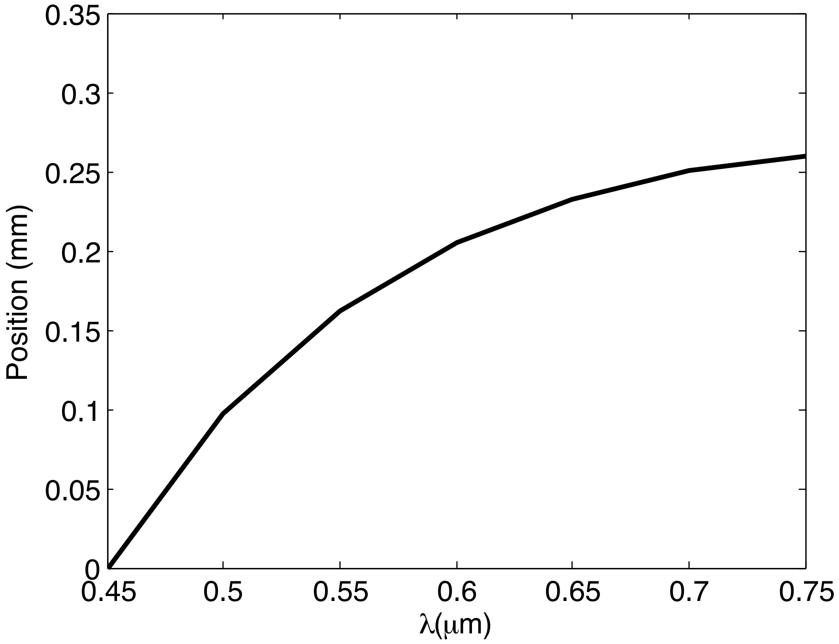

Figure 3.44: Focus position function of the illumination wavelength for the high resolution version of the CCM. The dispersion has been tailored to be asymptotic to zero in order to improve the measurement resolution.

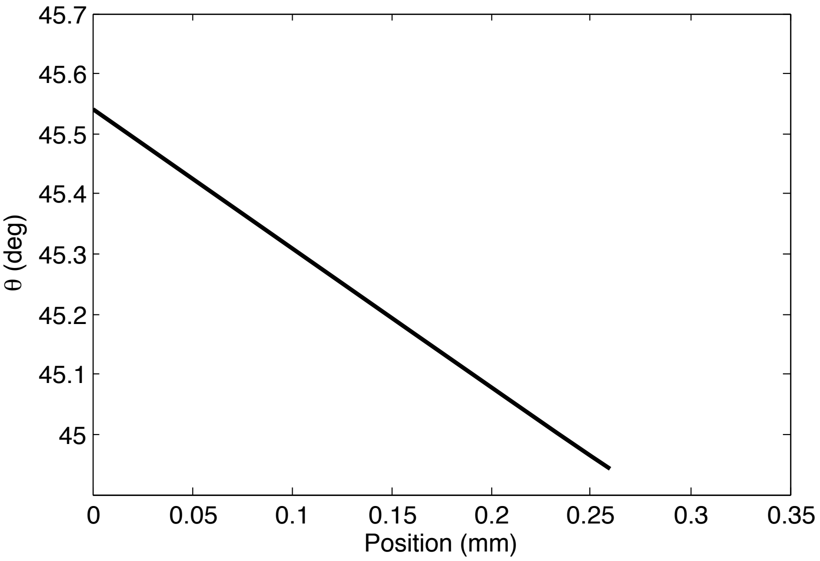

Figure 3.45: Maximum surface slope measurable by the high resolution version of the CCM function of the illumination focus position. The measurable surface slopes are below 45.6° and reduce with the focus position.

3.37 with L1 being an off-the-shelf achromatic lens, L2 a HAD and L3 an off the shelf aspheric lens. To match the target working distance and NA, the lens diameter is 25 mm. Then, the profile of the HAD was optimised in a ray tracing software to correct the remaining spherical aberration and create a dispersion of 250 μm. The difficulty in such a design is to reduce the optical head chromatic dispersion to a minimum without creating an inflection point. Once the focus position function of the range of measurement, shown in Figure 3.44, and the maximum measurement slope shown in Figure 3.45 are satisfied, the focal length of L1 is tuned to reach an acceptable compromise between the measurement resolution shown in Figure 3.47 and light throughput efficiency. The final system architecture is presented in Figure 3.46.

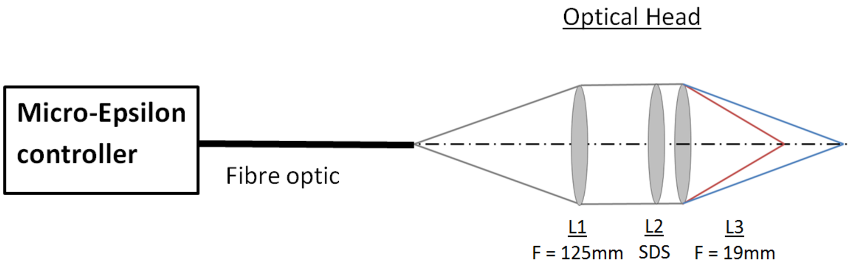

Figure 3.46: Architecture layout of the high resolution version of the CCM.

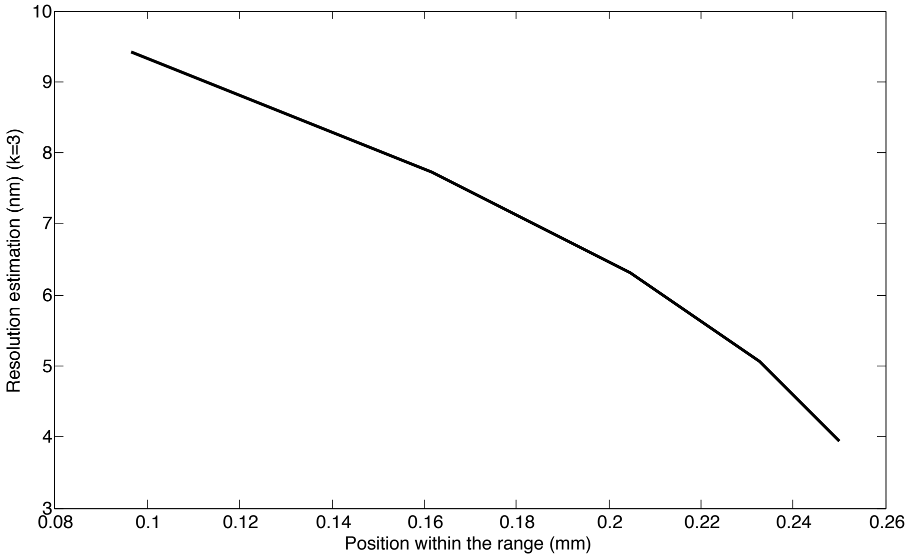

Figure 3.47: Numerically calculated resolution function of the position within the range of measurement of the high resolution version of the chromatic confocal microscope.

3.5 Discussion

This chapter has demonstrated how a deterministic approach allows the design of a low cost and a high resolution version of the chromatic confocal microscope with outstanding performance. The designed system fulfils all the target performances, especially the tight target cost of the low cost version. Both products are currently in the production phase. The novel numerical noise analysis combined with the novel analytical peak model has permitted the design of systems superior in their performance and costs to any others ever produced. In addition, the numerical analysis based on ray tracing data has enabled the reduction of the number of design cycles and prototypes. Hence, the cost and time necessary to design and develop a chromatic confocal microscope has been reduced.

It has to be mentioned that in this study the noise level is considered to be constant. In reality, the spectral efficiency of each individual element within the system will influence the measured spectral irradiance. Thus, the measurement resolution will deteriorate significantly at the extremum of the measurement range.

The design has been illustrated in this chapter in a linear and deterministic process. Nevertheless, the process described in Figure 3.1 needed to be applied several times, especially the “Investment/research” and “Capability”. The capability of the diffractive technology for chromatic confocal microscopy needed to be improved greatly compared to the current state of the art.

The following chapter will experimentally evaluate both systems. The experimental measurement will also validate the models build within this chapter. Finally, the impact of the measurement environment on both systems will be investigated.

Chapter 4

Performance evaluation and error correction of the chromatic confocal system

The performance of the two systems was evaluated numerically during the design phase in Chapter 3. However, the experimental performance as well as the impact of measurement environment onto the measurements were still unknown. Consequently, this chapter is dedicated to the experimental evaluation of the chromatic confocal microscope.

Firstly, the theoretical peak shape and measurement uncertainty models are validated experimentally. The validation and correction of the theoretical models allow the optimisation of the maximum signal irradiance against the height measurements averaged through time.

Secondly, the actual performance of both systems are measured to verify if the target specification are matched.

Finally, the impact of the measurement environment on the system is measured and mitigated when possible. This includes the surface slope, roughness, and reflectivity as well as the temperature of the measurement environment.

4.1 Validation of the chromatic confocal theoretical models

In the following section, the models developed in Section 3.1 are compared to experimental results. This includes the spectral irradiance and measurement standard deviation models. In addition, the peak irradiance function against the height measurements averaged through time is optimised.

4.1.1 Validation of the theoretical chromatic confocal peak shape

The novel analytical chromatic confocal spectral irradiance model described in Equation 3.3 is validated experientially with the optical head of the low cost version of the CCM and compared to the current confocal spectral irradiance model described in Equation 1.10 [71, 66].

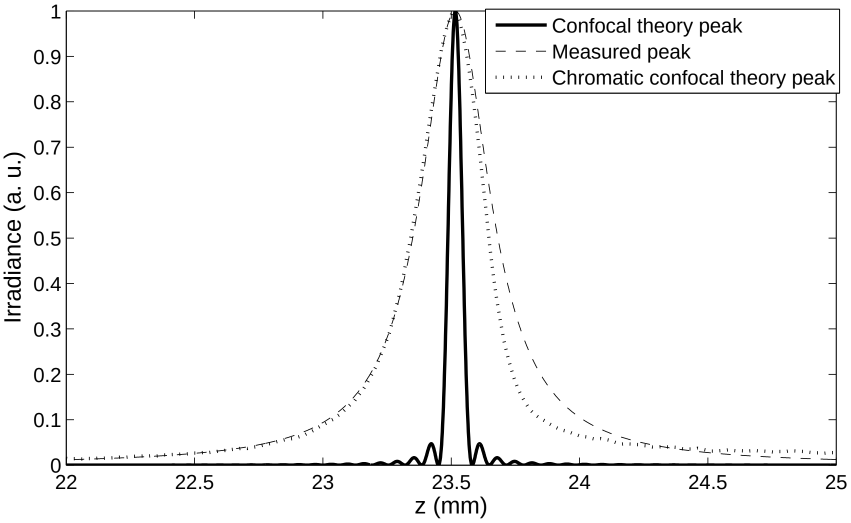

Figure 4.1: Chromatic confocal spectral irradiance comparisons for the low cost version of the CCM. The classical chromatic confocal spectral irradiance model, based on confocal theory, is compared with the novel chromatic confocal spectral irradiance model and a measured chromatic confocal spectral irradiance.

The parameters of the optical design simulation are used to calculate the spectral irradiance using Equation 3.3 and 1.10. The used pupil radius R is equal to 2.44 mm, the magnification M to 0.6887, the source pinhole radius R_p to 25 μm, and the focus position z_s to 23.5 mm.

Using these parameters, the chromatic confocal spectral irradiance is calculated using both the confocal and chromatic confocal models and compared to a measured chromatic confocal spectral irradiance, as shown in Figure 4.1.

Table 4.1: Comparison of the chromatic confocal peak FWHM calculated using the confocal and chromatic confocal spectral irradiance models to the measured chromatic confocal spectral irradiance of the low cost version of the CCM

	Measured	Confocal theory	Chromatic confocal Theory
FWHM (μm)	292	57	332
FWHM Error (μm)	0	235	40
Normalised peak integral error (a. u.)	0	248	39

As shown in Table 4.1, the integrated difference is more than 6 times lower using the novel chromatic confocal spectral irradiance model than with the confocal spectral irradiance model. This demonstrates the precision of the novel model compared to the previously used confocal model. In Figure 4.1, the major fitting error of the chromatic confocal spectral irradiance is on the right side of the peak. This error originates from the spectral irradiance of the light source which modulates the measured chromatic confocal peak shape. Therefore, the integrated difference between the measured and calculated chromatic confocal spectral irradiance could be improved by correcting the measured chromatic confocal spectral irradiance with the spectral irradiance of the light source.

Furthermore, the estimated FWHM using the chromatic confocal peak theory is 6 times more accurate than using the confocal peak shape theory, as exhibited in Table 4.1. In addition, the FWHM estimation error using the chromatic confocal peak theory suffers as well from the light source spectral irradiance modulation of the measured chromatic confocal peak.

It has been shown that the novel chromatic confocal peak theory described in Equation 3.3 allows a precise estimation of the chromatic confocal peak FWHM using only optical design parameters computed within the ray tracing software. These results are demonstrated on one chromatic confocal peak only. Nevertheless, the results are similar within the full measurement range and for other chromatic confocal optical heads. Using such a capability, the precision of the CCM noise model described in Section 3.1.2 can be fully calculated.

4.1.2 Validation of the chromatic confocal microscope noise model

The novel chromatic confocal microscope measurement standard deviation estimation, described in Equation 3.13, has yet to be validated. In fact, several assumptions have been made during the construction of the model.

The model is compared with the measured standard deviation of the low cost version of the CCM shown in Figure 4.6.

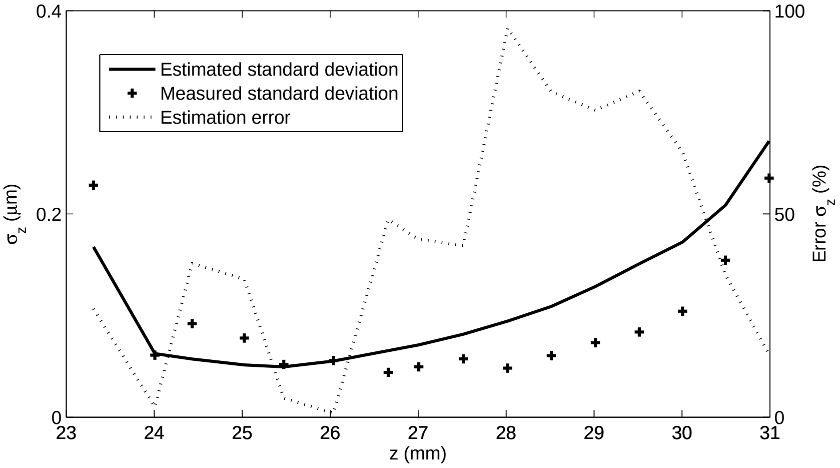

Figure 4.2: Comparison of the estimated with the measured standard deviation of the low cost version of the CCM measure at 200 Hz. The estimation error is below 50 % over the major part of the measurement range.

The optical parameters used to calculate the chromatic confocal peak FWHM are the same as for the previous section. The results shown in Figure 4.2 indicated a reasonable match between the measured and estimated standard deviation. In this thesis all the measurement standard deviations are always calculated from more than 200 samples . The estimation error is below 50 % over more than half of the measurement range and predicts the measurement standard deviation order of magnitude over the full measurement range. Furthermore, the estimation error is minimised when the normalised signal intensity is close to 1 as between 26 mm and

24 mm. The roots of the estimation errors are based on the assumptions made in Section 3.1.2. In Section 3.1.2, the chromatic confocal peak is Gaussian for computational simplicity. However, because of the shape of the peak is not Gaussian, the noise estimation is biased. In addition, as indicated by the non-homogeneity of Equation 3.12, the model is just an estimator using the peak FWHM as indicator. Furthermore, the parameter n in Equation 3.13 is estimated numerically assuming that the noise from the line sensor follows a Gaussian distribution.

Despite this limitation, this standard deviation estimation gives us access to information which was not accessible previously. The position standard deviation could only be measured. In addition, because of the estimator is pessimistic, the head can be designed with more confidence. This novel model allows us to reduce the number of design cycles necessary to reach the target performance. Moreover, the performances attainable can be estimated numerically to investigate potential new market opportunities.

4.1.3 Maximum signal intensity and position averaging optimization

The irradiance of the light reflected by the target varies as a function of the surface roughness, reflectivity, and slope. The irradiance measured on the line sensor can be tuned by changing the sensor integration time while increasing the measured irradiance increases the SNR: reducing the measured irradiance increases the sampling rate and therefore increases the number of positions averaged over time. Thus, the problem is to find, at a given sampling rate, which measured spectral irradiance minimises the measurement standard deviation.

Assuming that the measurement noise follows a Gaussian distribution, the position standard deviation averaged over time σ function of the number of locations averaged over time N, and the non-averaged measurement standard deviation σ_0 is

$$\sigma = \frac{\sigma_0}{\sqrt{N}}. \tag{4.1}$$

In section 3.1.2, it was shown that the measurement standard deviation σ_0

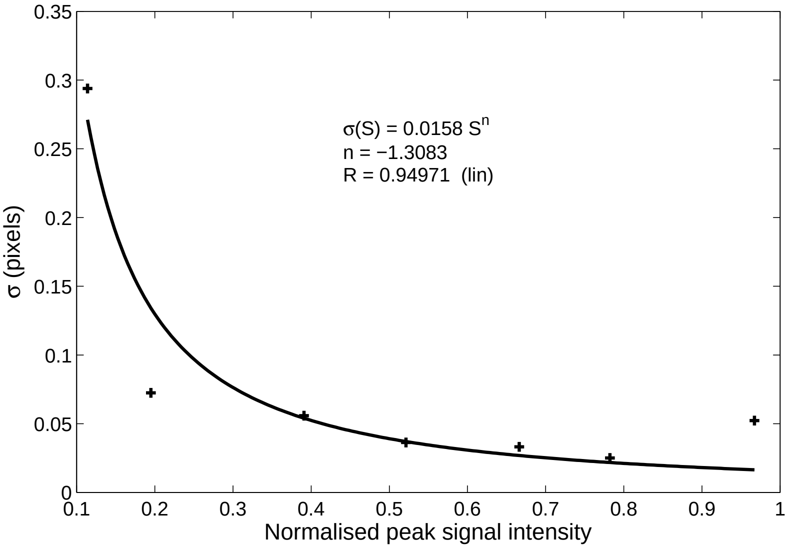

Figure 4.3: Line sensor reading standard deviation characteristic of the low cost version of the CCM. Cross mark: measured position standard deviation function function of the peak spectral irradiance. Line: Curve fitting. The fitted curve using the Equation 3.12 exhibit a reasonably high correlation ($R \approx 0.95$) with the measured data. The constant 0.0158 in the fitting equation represents the product of the line sensor reading standard deviation σ_{CCD} with the square root of the peak FWHM.

function of the peak spectral irradiance I can be expressed as

$$\sigma_0 = a\, I^n, \tag{4.2}$$

where a and n are constants.

The peak spectral irradiance I expressed as a function of the number of locations averaged over time N, can be expressed as

$$I = \frac{1}{N} \ . \tag{4.3}$$

Therefore by combining Equation 4.1, 4.2, and 4.3 the measurement standard deviation σ function of the peak spectral irradiance I and the number of average over time N can be expressed.

$$\sigma = a.N^{-(n+0.5)}. \tag{4.4}$$

Because the parameter n is estimated to be -1.139 in Section 3.1.2, the measurement standard deviation σ in Equation 4.4 at a given sampling rate increases with the number, N, of measurement locations averaged over time . The measurement standard deviation σ in Equation 4.4 at a given sampling rate reduces with N if, and only if, n is greater than -0.5.

Figure 4.3 demonstrates the validity of the measurement standard deviation model described in Equation 3.12. In fact, in Figure 4.3, a represents the product of the line sensor normalised reading standard deviation σ_{CCD} with the square root of the peak FWHM. The empirical parameter n in Figure 4.3 is close to the computed one in Section 3.1.2. Since the empirical parameter n is below -0.5, the peak spectral irradiance must be maximised in order to optimize the measurement resolution at a given sampling rate.

o

4.2 Performance evaluation of the chromatic confocal microscope

This section evaluates the performance of the low cost and high resolution versions of the CCM designed in Chapter 3. The parameters are calculated using the international standard ISO 25178-602:2010 [87] However, since this international standard does not describe explicitly the measurement protocol it has to be interpreted.

4.2.1 Experimental performance of the low cost version of the chromatic confocal microscope

The first specification to be verified is the calibration curve. To calibrate the probe, the RLU10 laser encoder from Renishaw [126] with a measurement resolution of 10 nm is used.

The measured chromatic confocal peak position on the line sensor against the relative distance is shown in Figure 4.5.

Because of a laser encoder is a relative distance measurement probe, the absolute

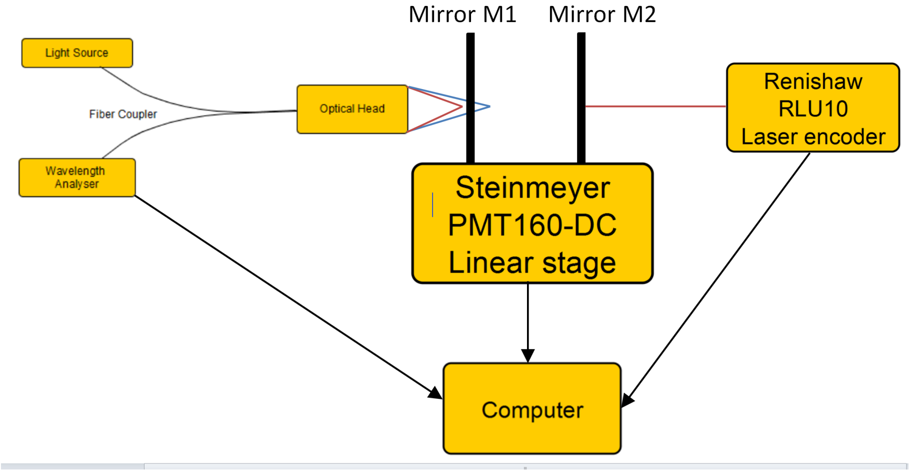

Figure 4.4: Experimental setup used to evaluate the performances of the low cost and high resolution version of the CCM. The setup uses a high precision linear stage from Steinmeyer [129] and a laser encoder from Renishaw [130]

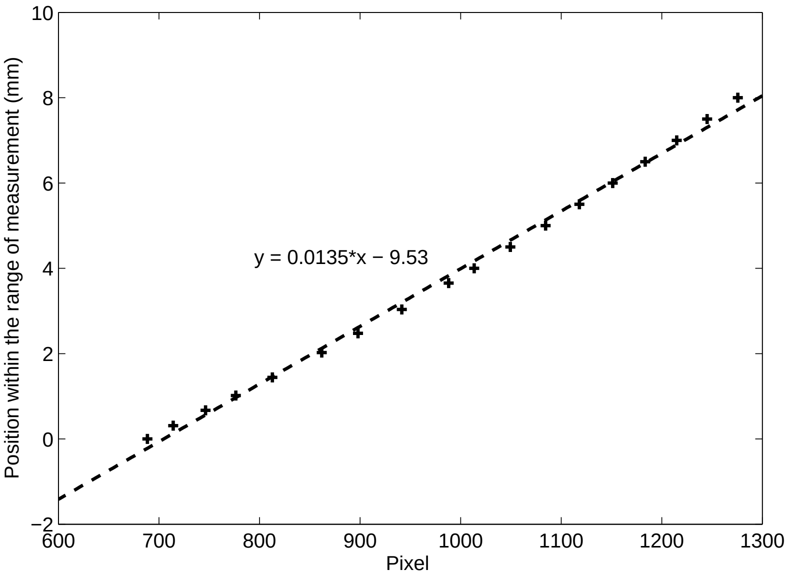

Figure 4.5: Calibration curve of the low cost version of the CCM. Cross mark : Experimental measurement. Dotted line : Strait line fit on the experimental data. As expected, the linearisation curve is nearly linear.

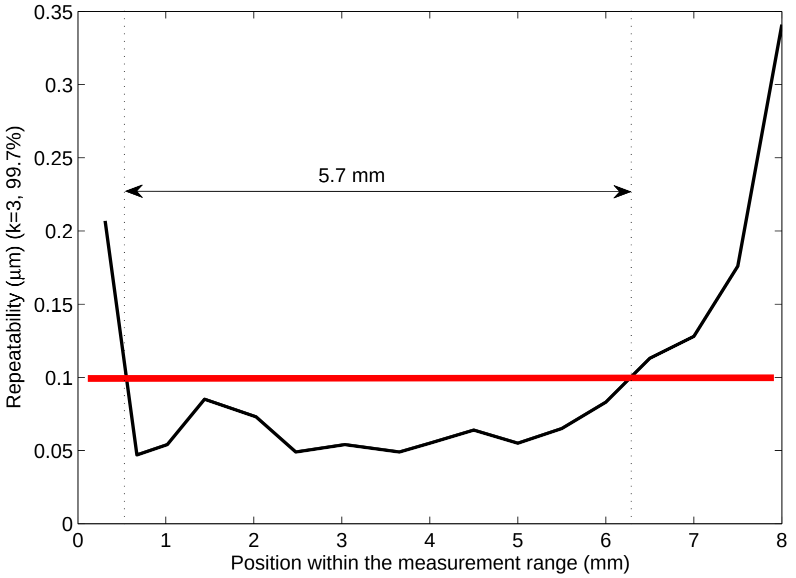

Figure 4.6: Resolution across the measurement range of the low cost version of the CCM. The Resolution is better than the target 100 nm at 5 Hz over 5.7 mm.

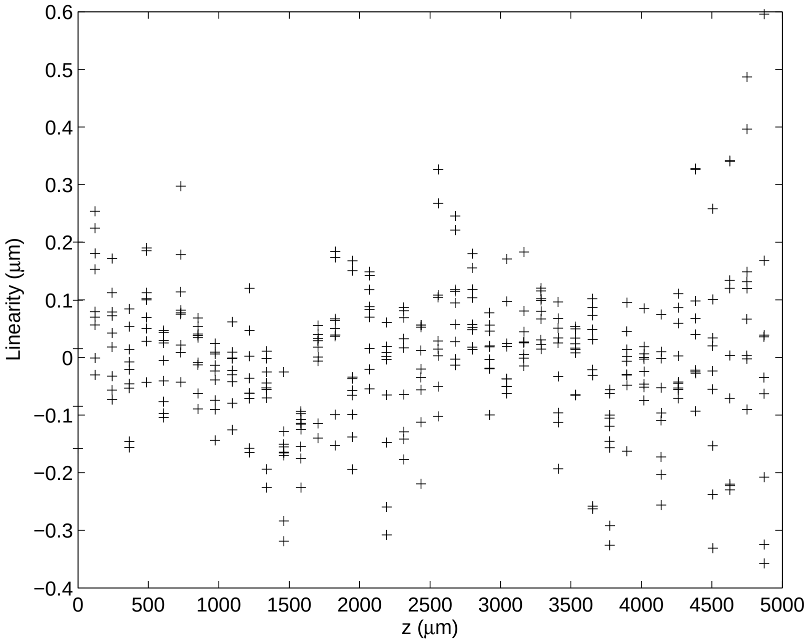

Figure 4.7: linearity of the low cost version of the CCM. All the points are within the target 1 μm.

position of the measurement is off-set by an arbitrary value. This arbitrary value is the measurement working distance. The measurement working distance is measured at 26 mm. The measurement is approximate since the mechanical housing of the lenses makes contact to the exit surface of the optical head difficult. However, an approximated measurement is sufficient.

The calibration curve shown in Figure 4.5 is nearly linear and equivalent to the one computed in Figure 3.40. Nevertheless, a linear fit is not sufficient to reach the required linearity. Two approaches are possible to extract the surface position from the linearisation curve; a polynomial fit or by interpolating between the measured points. The former method is computationally efficient and reduces the impact of the measurement uncertainty of the calibration curve. The latter allows highly repeatable measurement. However, it has been observed experimentally that the number of samples used for the calibration curve must exceed 500 and the measurement uncertainty of the measured point at least 5 times below the standard measurement repeatability. Due to frequency content exhibited by the calibration curve, the best results are obtained by using a piecewise cubic interpolation [131].

Figure 4.6 shows the resolution within the range of measurement at a sampling rate of 5 Hz. The resolution is better than the 100 nm target within 5.7 mm.

The shape of the curve is different from the theoretical measurement resolution shown in Figure 3.43. In fact, the “U” shape of the resolution in Figure 4.6 is induced by the variation of the peak spectral irradiance throughout the range measurement. In Figure 3.43, the SNR is assumed to be constant through the range of measurement.

Because the SNR is the factor limiting the measurement range, the measurement range is defined as the difference between the first $\overline{x}_{min}$ and the last point $\overline{x}_{max}$ with a measurement standard deviation σ_{n-1} 10 time the minimum standard deviation $\sigma_{n-1}|_{min}$ measured. Thus the range of measurement Δx is defined as

$$\Delta x = \overline{x}_{max}(\sigma_{n-1} = 10\ \ \sigma_{n-1}|_{min}) - \overline{x}_{min}(\sigma_{n-1} = 10\ \ \sigma_{n-1}|_{min}) \tag{4.5}$$

Using this definition, the measurement range is 7.8 mm. To sum up, the target measurement repeatability is achieved over 5.7 mm, although in fact the signal can be measured over more that 7.8 mm. The measured range significantly exceeds the target 7 mm.

The measurement repeatability, as defined by the BIPM [4], is measured by repeating the calibration protocol 10 times. Then, the deviation from the first linearisation curve is calculated. The linearity error results are in Figure 4.7 shows that all the points are within the 1 μm target. Furthermore, 90 % of the points are actually in a 0.5 μm band. The repeatability of 1 μm corresponds to 0.01 % of the measurement range. An equivalent system supplied by Micro Epsilon Gmbh. [65] exhibits a linearity of 0.2 % of the measurement range. In other words, the designed system improves the linearity by a factor 20. Furthermore, Micro Epsilon only repeats the calibration once to determine the repeatability. If the linearisation curve measurement is repeated only once, the repeatability is 0.003 % of the measurement range .

Since it takes more than an hour to record the 10 traces, it is difficult to maintain all the measurement conditions constant for such a period of time; especially the temperature. A $0.5°C$ temperature drift has been measured within the measurement cycle which has increased the repeatability error by around 0.5 μm due to the thermal drift coefficient of 0.9747 $\mu m/°C$ measured in Section 4.3.1. The temperature drift could also explain the “W” shape of the repeatability error shown Figure 4.7.

The last specification to be measured is the spot size on the target. The spot size is defined in the ISO 25179-602:2010 as the “maximum lateral size of the projected image of the source pinhole” [87]. However, this value is not practically measurable as it depends on SNR of the detector. The spot size W_{spot} as is defined as the FWHM of the irradiance projected onto the surface. Furthermore, in the ISO 25179-602:2010, the spot size W_{spot} is assessed through the lateral resolution by measuring a calibrated step [87]. However, such a method relies on the measurement uncertainty of an artefact. Since the lateral resolution is derived from the spot size W_{spot}, the spot size is assessed directly rather than through the lateral resolution.

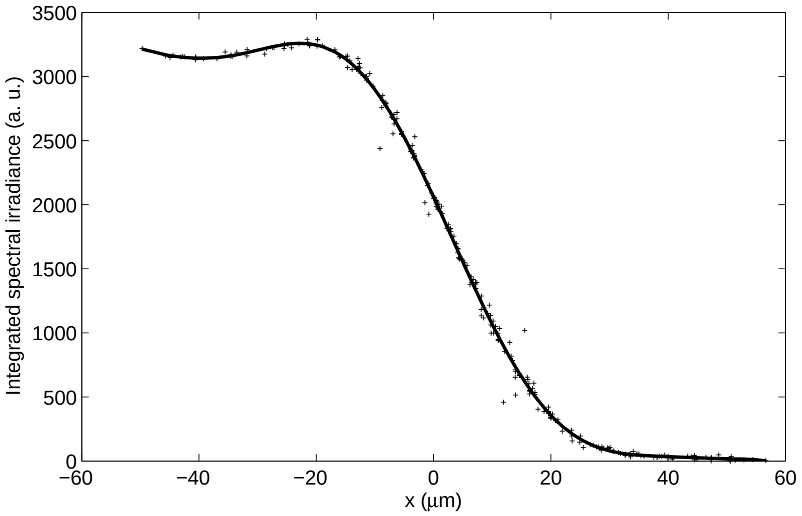

(a) Integrated spectral irradiance measured along the edge of a cleaved silicon wafer. The x positions are measured using a laser encoder with a resolution of 10 nm. The experimental data, cross mark, are fitted with a 5^{th} order polynomial function.

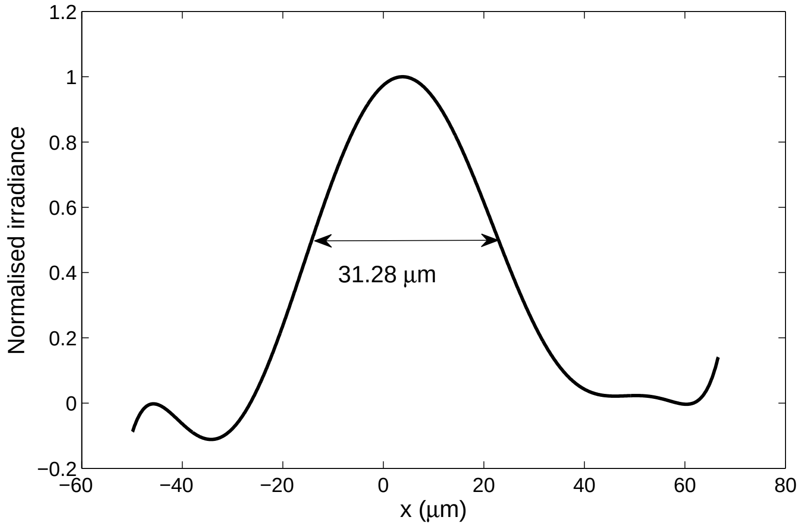

(b) Gradient of the integrated spectral irradiance measured in a). The measured spot size is 31.28 μm against 35 μm theoretically estimated in Section 3.3.3

Figure 4.8: Experimental measurement of the chromatic confocal spot irradiance distribution. The correlation between the theory and the experiment is satisfactory as the results are repeatable within less than 1 % of the FWHM.

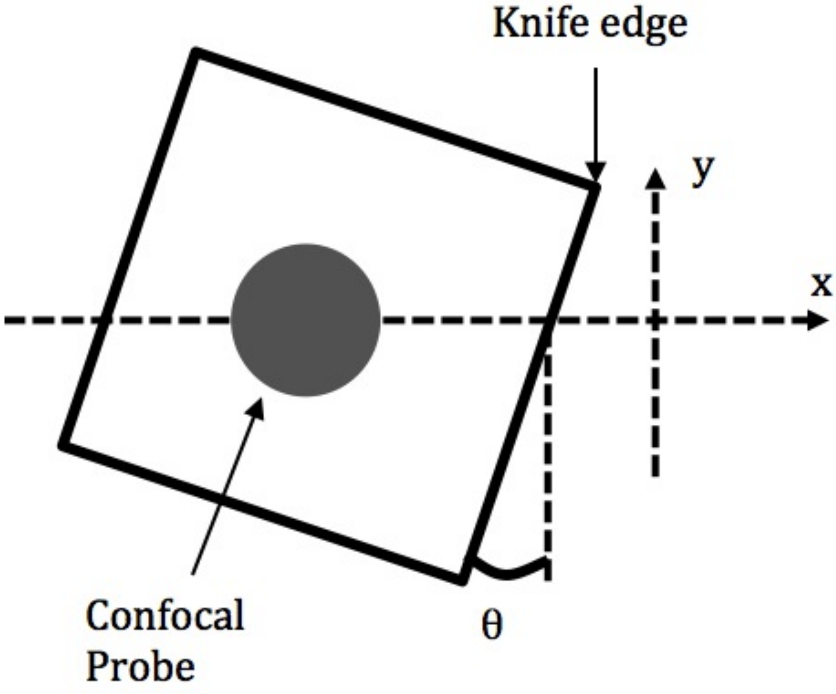

Figure 4.9: Schematic of the experimental set-up to measure the spot size W_{spot}

The spot size is calculated based on the one dimensional measurement of a cleaved silicon wafer acting as a perfect edge as shown in Figure 4.9. The concept is to measure the integrated signal intensity through the edge. The measured integrated spectral irradiance $I_{int}(x)$ is the convolution of the edge with the spot irradiance distribution $W_{spot}(x, y, \lambda)$ on one axis and can be expressed as following

$$I_{int}(x) \propto \int\int H(x) \ast W_{spot}(x, y, \lambda)\, \mathrm{d}y\, \mathrm{d}\lambda, \tag{4.6}$$

where $H(x)$ is the Heaviside function [22] and $\ast$ represent a convolution.

Because the gradient of a Heaviside function is a Dirac function [22], the spot irradiance distribution along the same axis as the Heaviside function can be accessed by calculating the gradient of the measured signal intensity distribution $I_{int}(x)$ as expressed in the following equation

$$W_{spot}(x) = \frac{\delta I_{int}(x)}{\delta x}. \tag{4.7}$$

If the spot is circular symmetric, the minimum FWHM will be measured when the misalignment angle θ, described in Figure 4.9, is null. In addition, if the spot irradiance distribution is Gaussian, the FWHM function of the angle θ is:

$$\mathrm{FWHM}(\theta) = \frac{\mathrm{FWHM}(0)}{\cos(\theta)}. \tag{4.8}$$

The measured spot size of 31.28 μm is close to the theoretically estimated 35 μm in Section 3.3.3. The measured spot size is smaller by several μm due to the real source pinhole irradiance distribution and the aberrations of optical system. In Section 3.3.3, the irradiance distribution has been considered uniform within the 50 μm diameter of the optical fibre core and the PSF of the optical system a Dirac function. Practically, the irradiance is higher at the center of the fibre optic core than at the edge, which leads to a reduction of the spot size. However, the aberrations of the optical system increase the spot size. Both phenomenons occur simultaneously but the fibre optic core irradiance distribution is predominant. Therefore, the measured spot size W_{spot} is smaller than the theoretically estimated one.

4.2.2 Experimental performances of the high resolution version of the chromatic confocal microscope

The performance of the high resolution version of the CCM is assessed similarly as for the low cost version of the CCM.

The measured resolution in Figure 4.6 is better than 10 nm over more than 200 μm of the measurement range. This is 4 times improved compared with the target 50 μm. Due to the asymptotic shape of the linearisation curve shown in Figure 3.44, the resolution function of the position within the range of measurement does not exhibit a “W” shape as in Figure 4.6. In fact, the impact of the SNR onto the resolution is compensated by the increasing chromatic dispersion within the range. Following the same protocol as in the previous section, the measurement range is measured to be 320 μm.

The repeatability shown in Figure 4.11 is contained within a band of 100 nm. These results are satisfactory since the measured linearity errors are mostly related

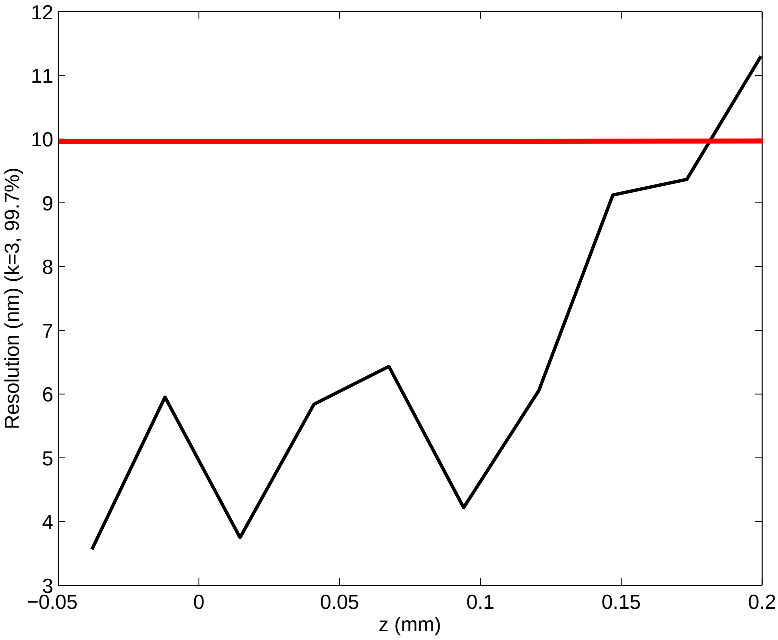

Figure 4.10: Resolution of the high resolution version of the CCM. The red line represents the target resolution of 10 nm. The resolution is better than the 10 nm target over more than 200 μm of the measurement range.

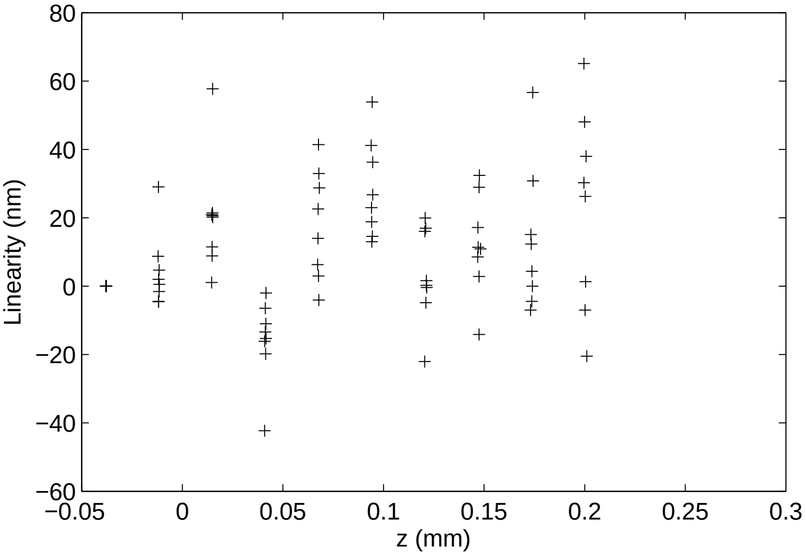

Figure 4.11: linearity of the High resolution version of the CCM

to the temperature variation within the measurement cycle. The measured repeatability is equal to 0.04 % of the measurement range, which is similar to the equivalent system from Micro Epsilon Gmbh. [65]. Furthermore, Micro Epsilon only repeats the calibration once to determine the repeatability. If the linearisation curve measurement is repeated only once, the repeatability is 0.16 % of the measurement range which is half that for the equivalent CCM optical head from Micro Epsilon Gmbh. [65].

4.3 Measurement environment impact on the measurement

The environment impact on the measurement can harm the performances of the system. The project aim is to build an industrial system suitable for use in various atmospheric condition and materials.

The low cost version of the CCM is designed to be used in a manufacturing environment on surfaces of various roughness and reflectivity. The low cost version of the CMM must have a temperature sensitivity below 1 $\mu m/°C$, a linearity error of less than 10 μm for samples with a roughness coefficient Rq [132] of 0.8 μm, and a linearity error of less than 10 μm for copper and brass samples.

The high resolution version of the CCM is designed to be used within the controlled environment of the SPDT machine on surfaces of various reflectivity with a specular reflection. The sensor is calibrated on the part to be measured. Hence, the surface reflectivity impact on the measurement is automatically compensated by the calibration. The temperature variation is not an issue for this application because the measurement cycle is less than a minute and the sensor is calibrated regularly. Moreover, since the measurement drift introduced by the temperature variation is mostly linear, significant drifts occurring outside the measurement cycle introduce only an measurement off-set. However, if the SPDT machine does not have a rotary “B” axis or the measured part has more than five degrees of freedom, the measured surface slope is not null. Thus, the measurements have to be corrected for the linearity error introduced by the slope of the measured surface

4.3.1 Temperature sensitivity of the measurement

The temperature related linearity error of the measurement has been previously studied in Section 3.2.3.3 for three optical head configurations. The results shown in Table 3.9 highlight that the most temperature stable configuration is for two glass lenses with one surface exhibiting a SDS profile. However, since a mould for precision glass moulding costs approximately \$50,000, this solution has not been tested experimentally. The thermal measurement stability has been measured for the full plastic and hybrid glass/plastic designs.

The temperature related linearity error is calculated by measuring a constant distance while changing the temperature of the measurement environment by a step of 10 $°C$ from 10 to 40 $°C$ and then back from 40 to 10 $°C$. The ramp up and down highlights the hysteresis of the temperature related linearity error. For each step, the temperature is maintained constant for 30 min to distinguish the transient from the steady state temperature related linearity error.

Table 4.2: Environment temperature impact on the measurement of the low cost version of the CCM. The temperature related linearity errors calculated in Section 3.2.3.3 match the measured ones. The transient coefficient, calculated for a temperature step of 10 $°C$, is similar for both designs.

	Full plastic	Hybrid glass/plastic
Calculated linearity error ($\mu m/°C$)	21	0.66
Measured linearity error ($\mu m/°C$)	15	0.97
Transient state coefficient τ for 10 $°C$ (s)	324	301

Firstly, no hysteresis linearity error has been observed in the steady state. Secondly, the calculated temperature related linearity errors match the ones shown in Table 4.2. The measured temperature related linearity error of the hybrid glass/plastic design is below the target of 1 $\mu m/°C$ as shown in Figure 4.12. The design choice in Section 3.2.3.3 is validated.

Finally, the transient state coefficient for a step of 10 $°C$ is similar for both

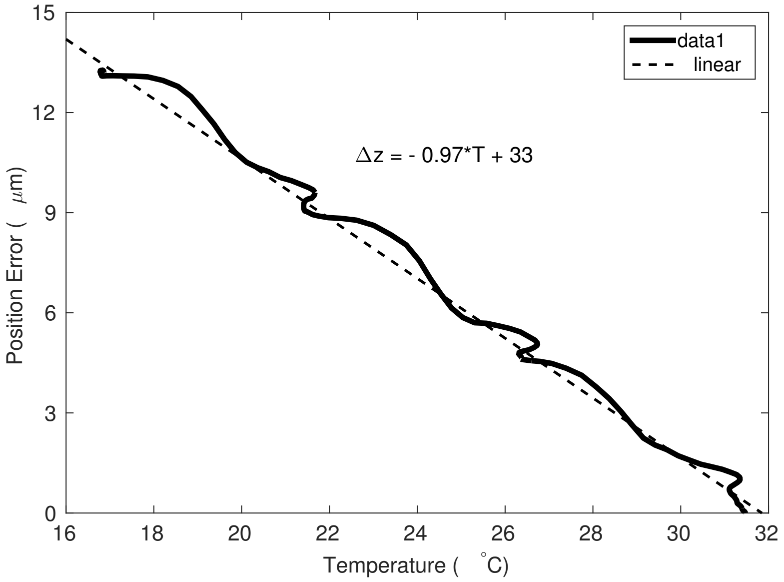

Figure 4.12: Position drift function of the temperature for the low cost version of the CCM with a full plastic optical system.

designs. The transient state coefficient is lower for the hybrid glass/plastic design because the plastic thermal conductivity such as PMMA is twice lower than of glass such as N-BK7 [133, 134]. The transient state coefficient τ is calculated by fitting the following equation to the linearity error Δz through time t in the transient state as shown in Figure 4.13,

$$\Delta z = \alpha \, \Delta T \, e^{-\frac{t}{\tau}}, \tag{4.9}$$

where α is the linearity error coefficient and ΔT the temperature step.

Since no hysteresis has been observed for the temperature related linearity error, this error can be actively corrected by calibrating the linearity error function of the temperature. If it is assumed that the temperture response of the system can be linear time invariant, Figure 4.13 would indicate that the system is of the first order. Thus, the transfer function in the Laplace space of the system is

$$H(s) = \frac{\alpha}{\tau + 1}. \tag{4.10}$$

The response of a system described in Equation 4.10 to linear gradient of

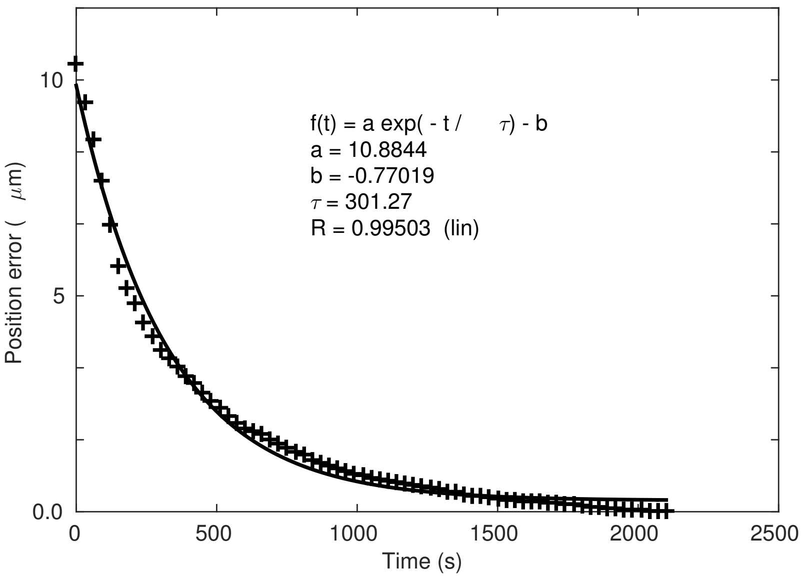

Figure 4.13: Transitional position error of the low cost version of the CCM for a temperature step of 10 $°C$. Cross mark: experimental data, Line: Exponential decay fit of the experimental data.

temperature generate a following error expressed as

$$\Delta z = \alpha \frac{\partial T}{\partial t} \tau. \tag{4.11}$$

Thus, if the target temperature related linerity error after active temperature correction is 100 nm, the maximum temperature gradient is 0.019 $°C/min$

4.3.2 Surface roughness sensitivity of the measurement

The roughness of the measured surface is known to influence non-contact distance measurement sensors such as MWLI [56] or laser triangulation gauge [135]. For the CCM, the understanding of the impact of the surface roughness on the measurement is limited [86]. Nevertheless, the roughness profile within the spot size must distort the chromatic confocal irradiance.

To quantify the linearity error of the low cost version of the CCM introduced by the surface roughness, samples of various surface roughness are measured laterally in the x direction as shown in Figure 4.14.

The flat measurement results shown in Figure 4.15 exhibit a linearity error of more than 40 μm.

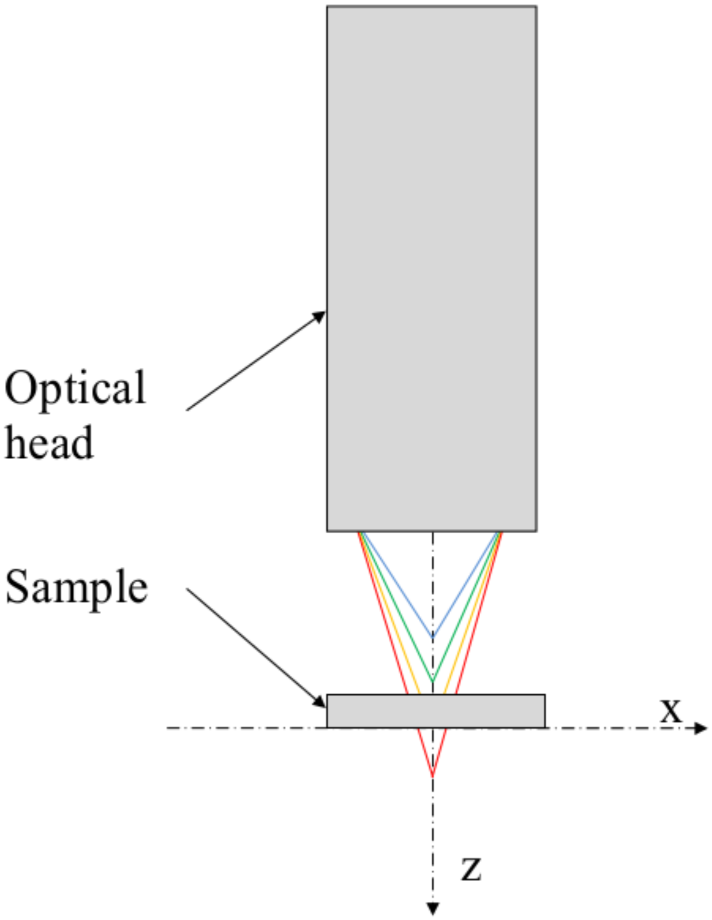

Figure 4.14: Schematic of the set up used to measure the impact of surface roughness on the CCM linearity.

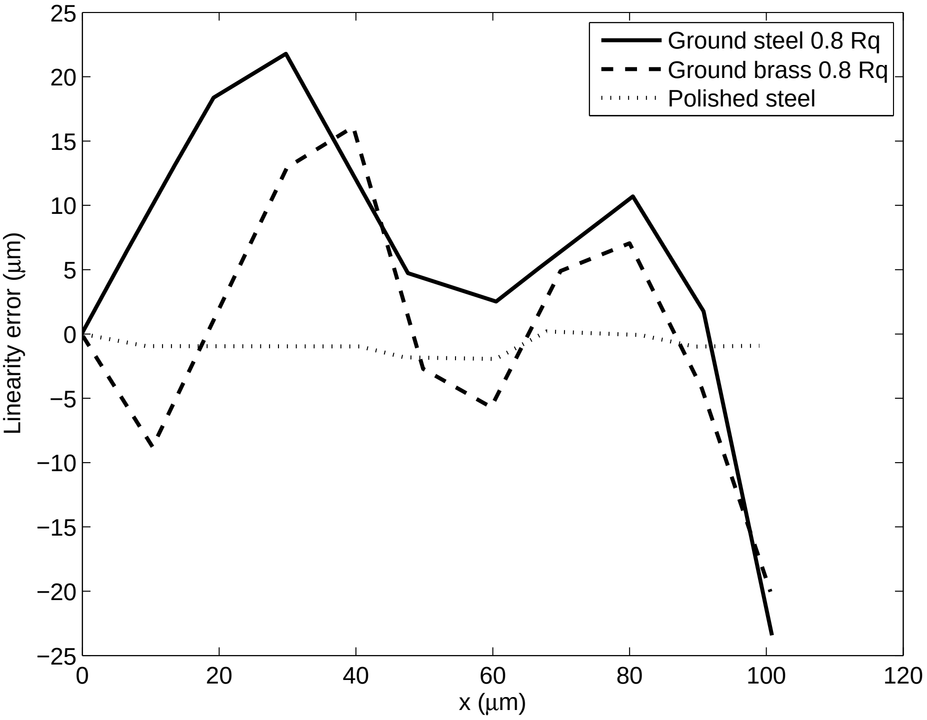

Figure 4.15: Lateral measurement of flat sample of various roughness and reflectivity in the x direction using the low cost version of the CCM.

The linearity error is above the 10 μm target. Therefore, the surface roughness impact onto the linearity has to be mitigated. The rather encouraging fact is that the linearity error profile are similar in shape to the brass and steel samples of 0.8 Rq [132]. Even if the surface reflectivity of the samples contributes to the linearity error, the correlation in shape between the measurements indicates that the linearity error associated with the surface roughness is deterministic and repeatable. Therefore, it might be possible to mitigate the linearity error associated with the surface roughness of the measured surface. One possible approach could be to fit the measured spectral irradiance with Equation 3.3 or a Gaussian distribution

Further experiments are currently carried out to quantify the improvement using this method.

4.3.3 Surface reflectivity influence on the measurement

The surface reflectivity impact on the chromatic confocal measurement is known to influence the linearity of the CCM [86]. However, the origin of the linearity error

Table 4.3: Computed linearity error introduced by a surface with roughness profile following a Gaussian distribution using various peak finding methods

Peak finding method	Gaussian Surface (0.3 μm Rq)	Sinus Surface (0.3 μm Rq)
CCM Theoretical irradiance fitting (μm)	70	17
Gaussian distribution fitting (μm)	46	2
Blai-Rioux peak detector	262	55

is not described in the literature. The measured CCM spectral irradiance $I_{Meas}(\lambda)$ can be expressed as

$$I_{Meas}(\lambda) = I_{Source}(\lambda) I_{Coupler}(\lambda)^2 I_{Spectrometer}(\lambda) I_{Head}(\lambda)^2 I_{Sample}(\lambda) I_{CCM}(\lambda), \quad (4.12)$$

where $I_{Source}(\lambda)$ is the light source spectral irradiance, $I_{Spectrometer}(\lambda)$ the spectrometer spectral efficiency, $I_{Coupler}(\lambda)$ the light circulator spectral efficiency, $I_{Head}(\lambda)$ the optical spectral efficiency of the head, $I_{Sample}(\lambda)$ the spectral reflectance of the measured sampled, and $I_{CCM}(\lambda)$ the CCM spectral irradiance described in Equation 3.3.

In Equation 4.12, $I_{Head}(\lambda)$ and $I_{Coupler}(\lambda)$ are squared because of the double pass of the light through the optical head and the fibre coupler. Therefore the chromatic confocal peak spectral irradiance $I_{CCM}(\lambda)$ is distorted in Equation 4.12.

Apart from the spectral irradiance of the surface $I_{Sample}(\lambda)$, the distortions are corrected by the linearisation of the chromatic confocal probe. Thus, for each sample with a different spectral reflectivity than the one used during the calibration, the linearity error is increased. The linearity error introduced by the spectral reflectivity is related to the gradient of the spectral reflectivity of the surface as shown in Figure 4.16.

Figure 4.17 shows the linearity error introduced by the spectral reflectance of a copper sample. The form of the linearity error in Figure 4.17 is similar to the computed one in Figure 4.16b.

The linearity error introduced by the spectral reflectivity of the copper sample

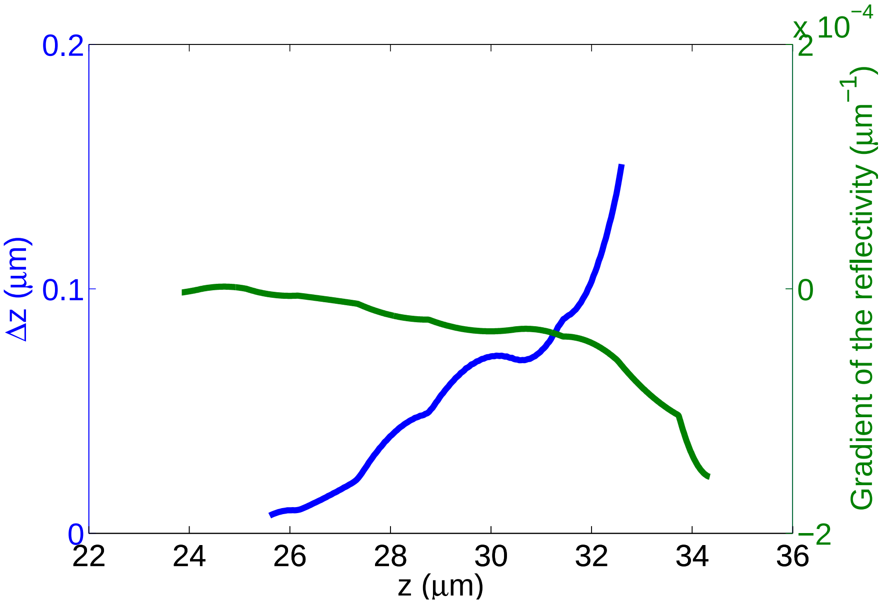

(a) Aluminium

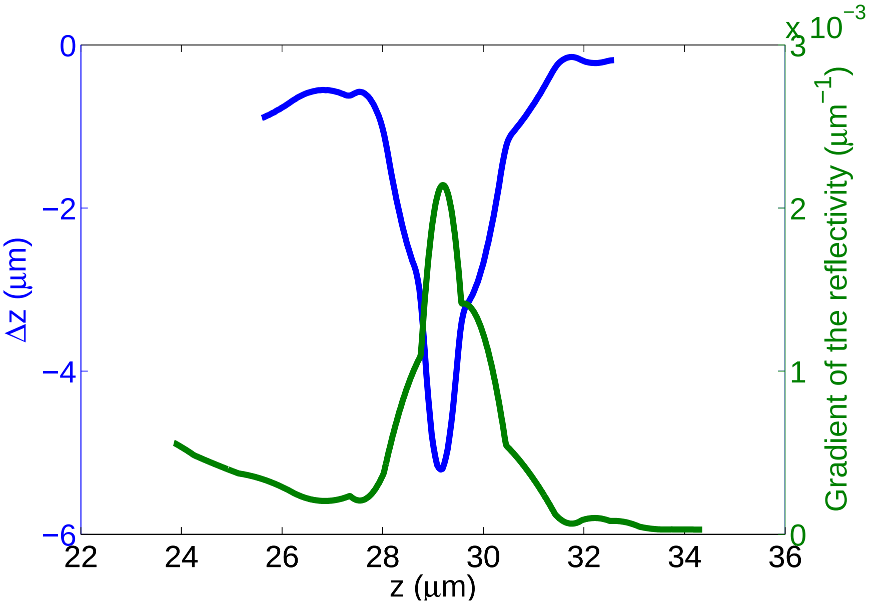

(b) Copper

Figure 4.16: Blue : Linearity error, Green : Reflectivity gradient of the sample. The linearity error introduced by the spectral reflectivity of the measured sample is related to the the gradient of the spectral reflectance. Thus, a material with a high reflectivity throughout the full visible domain such as aluminium exhibits a linearity error more than an order of magnitude lower than for a copper sample

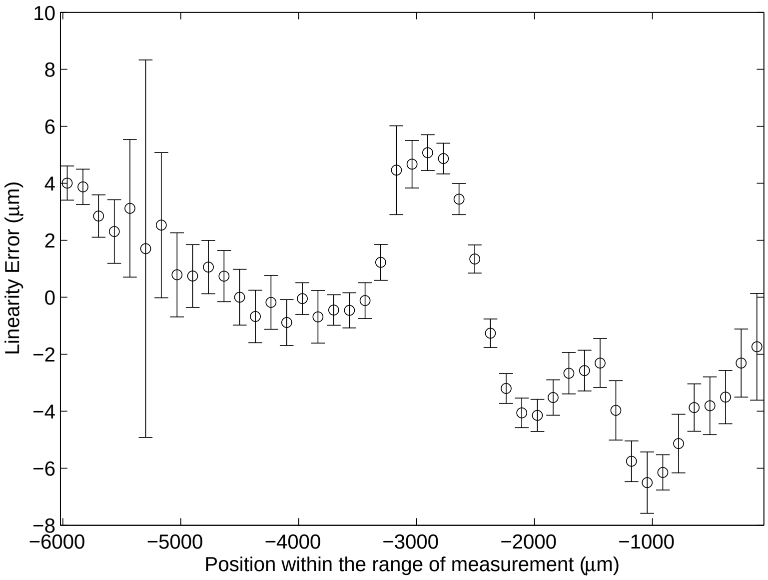

Figure 4.17: linearity error introduced by the surface reflectivity of a copper sample on the low cost version.

is more than 10 μm Peak To Peak (P2P). Therefore, to achieve the target of 10 μm, the linearity error must be mitigated.

The spectral efficiency of $I_{Source}(\lambda)$, $I_{Coupler}(\lambda)$, $I_{Spectrometer}(\lambda)$, and $I_{Head}(\lambda)$ can easily be measured during the calibration of the optical head by recording the maximum spectral irradiance through the measurement range. The spectral reflectance of the sample used during the calibration cannot be de-coupled from the system spectral efficiency. However, samples, such as aluminium or nickel, exhibit a non-significant reflectivity variation through the visible domain, as shown in Figure 4.16a. Therefore, by using the handbook value of the spectral reflectivity of material such as copper[134], the distortion introduced by the spectral reflectivity of the sample can be corrected. For alloys such as brass, the spectral reflectivity is unknown. By comparing the spectral irradiance efficiency of the system with the one performed on a Nickel or Aluminium sample, the spectral reflectivity $I_{reflectivity}$ of any material can be measured.

Attempts have been made to apply such a correction without significant success. The power supply of the light source or the reference voltage of the CCD analogue to digital converter is not stable enough; which leads to significant spectral irradiance variation through time. Further investigations are currently being carried out to improve the signal irradiance stability over time.

4.3.4 Surface slope sensitivity of the measurement

The measurement of the CCM is known to be surface slope dependant [86]. However, the source of the slope related linearity error is unknown.

To illustrate the linearity error introduced by the surface slope, Figure 4.18 shows the computed spectral irradiance for a surface slope of 0° and 20° for the optical head of the high resolution version of the CCM. The peak FWHM is enlarged by 85 % and the peak position is red shifted by 2.5 %.

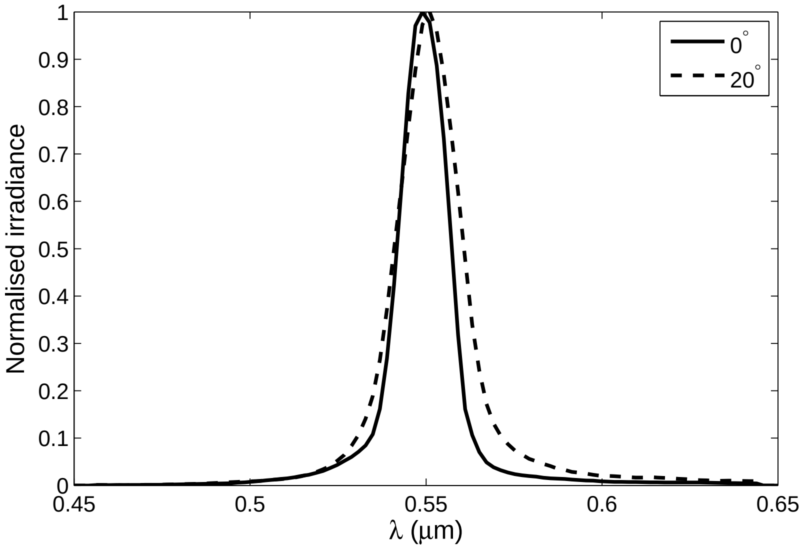

Figure 4.18: Computed spectral irradiance of the high resolution version of the CCM based computing using ray tracing for surface slope 0° and 20°. The peak response is enlarged and red shifted respectively by 85 % and 2.5 %

Among others, the possible source of surface slope related error are

- The optical magnification
- The pinhole size
- Optical aberration
- The PSF

Firstly, numerical computation indicates that the PSF distortion induced by the surface slope is not a significant source of surface slope related linearity error.

Secondly, ray tracing computation of an equivalent paraxial optical design to the high resolution version of the CCM exhibits no significant slope related error.

Thus, the surface slope related linearity errors are, in a first order, only related to optical aberration arising from the optical design, the optical element alignment error, and the form errors of the lenses. Considering the source pinhole size of only a few tens of μm, only aberrations occurring on the optical axis are relevant. In consequence, the relevant geometric aberrations are astigmatism and spherical [103]. Spherical aberration introduces a degeneration of the PSF in a rotationally symmetric fashion around the optical axis. Thus, the slope related linearity errors have two degrees of freedom; the measured position and the local surface slope. On the contrary, astigmatism is by nature non-rotationally symmetric. Consequently, an addition degree of freedom is added to slope related error. This addition degree of freedom can be corrected for 2D measurement. However, in 3D measurement assessing the local surface slope in the x and y direction is not practical. Therefore, the astigmatism of the optical system must be corrected to a minimum in to order to improve the correction of the slope related linearity error.

Because the source of the surface slope related errors are non-deterministic, each optical head has to be calibrated for those errors. The calibration involves the measurement of linearity errors at various surface slope within the range of measurement. Then, for each measurement, the height z_{Meas} and the local slope θ_S of the surface is measured. Function of the measured surface height z_{Meas} and slope θ_S, the measurement is corrected using the calibration function of the head $\delta_{Slope}(z_{Meas}, \theta)$. The corrected measurement can be expressed as

$$z_{Corr} = z_{Meas} - \delta_{Slope}(z_{Meas}, \theta_S) \tag{4.13}$$

The local surface slope θ_S can be assessed by two means; using the theoretical surface profile partial derivative with the radial coordinate of the object, or using the FWHM of the chromatic confocal peak. The former method assumes that the part is known and that the form error of the part is unimportant compares to the actual part form. The latter requires the FWHM function of the surface to be calibrated.

It has been demonstrated experimentally that the FWHM of the CCM peak shows a sufficient correlation with the local surface slope to achieve an uncertainty of 0.1°. Both methods are relevant but for simplicity reasons, the following work uses the theoretical partial derivative of the measured part to assess the local surface slope

Considering the measurement range of only 250 μm, such a calibration can only be performed on a high precision CMM such as a SPDT machine. No precision CMM has been available within the length of this project, therefore the surface slope related linearity error calibration is investigated using an equivalent optical design with a range of measurement of 600 μm.

The experimental set-up used to evaluate the slope related linearity error is presented in Figure 4.19. The aim of the set-up is to measurement the profile of cone of various angle. The cones have been manufacture using SPDT machining to exhibit an optical grade surface finish and a low form error. Five cone of 5°, 10°, 15°, 20°, and 25° are used for the calibration. A "flat" is manufactured on top of the cone, orthogonal to the rotation axis, to provide a measurement reference

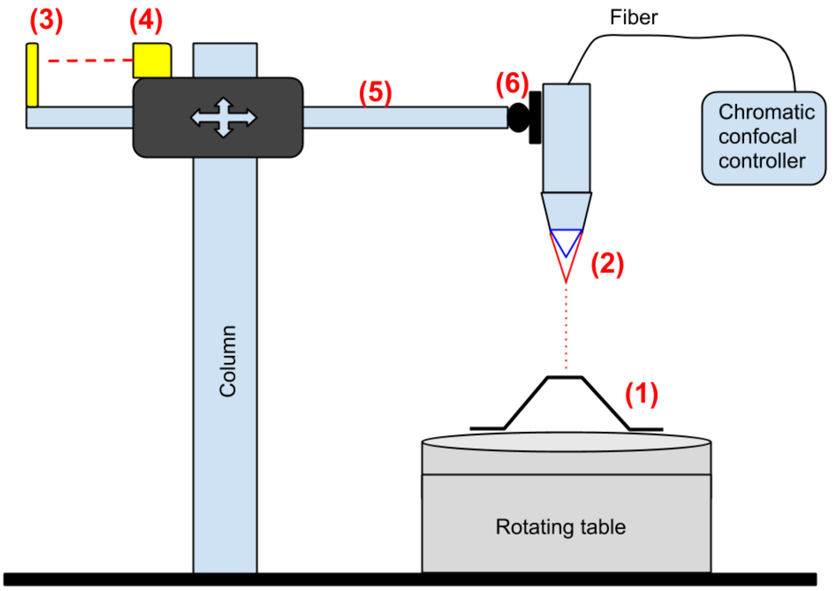

Figure 4.19: Experimental set-up used for the evaluation of the surface slope related linearity error. (1) Cone standard, (2) Chromatic confocal optical head, (3) reference mirror, (4) Laser encoder, (5) Measurement arm, (6) Optical mount. The rotating table allows the alignment of the optical axis of the optical head to be collinear to the rotation axis of the rotating table. The lateral position of the optical head is then translated to record the profile of the cone. The lateral position is measured using a laser encoder.

The rotating table used in Figure 4.19 is a high precision air spindle with an eccentricity error of only a few tens of nanometre. The rotating table is used as reference to align the rotation axis of the cone with the optical axis of the optical head to less than 500 nm eccentricity and 0.02°. The cone profiles are measured through the full measurement range and compared with reference measurements of the cone artefacts acquired using the PGI Dimension [2]. The difference between the two measurements for each cone artefact provides us with the slope related linearity error from 0 to 25° throughout the full measurement range of the optical head as shown in Figure 4.20.

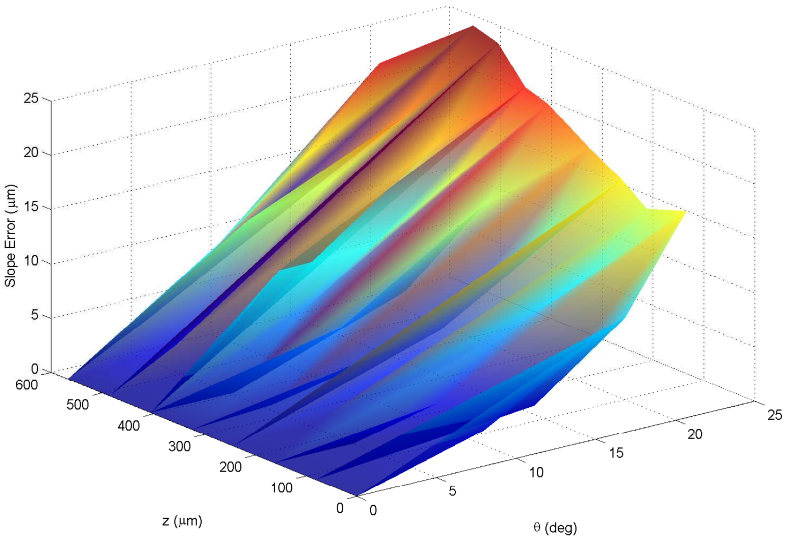

Figure 4.20: Slope related linearity error for a 600 μm measurement range CCM optical head from 0° to 25 ° through the measurement range.

Figure 4.20 highlights that the slope related linearity error correspond to approximately 4% of the measurement range.

In order to evaluate the capability of the calibration, a calibrated tungsten carbide ball of 12.4859 mm radius is measurement using the same set-up used during the calibration.

Without surface slope calibration, the residual error shown in Figure 4.21 correlates with the surface slope related linearity error measured in Figure 4.20. This exhibits a best fit radius error of 264 μm.

Using the calibration data of the surface slope related linearity error shown in Figure 4.20 the measurement is corrected and the residual form error is as shown in

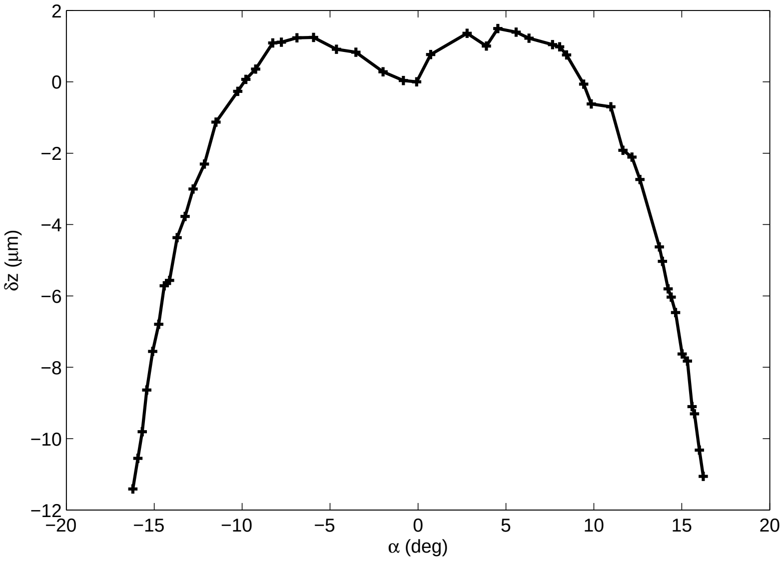

Figure 4.21: Nominal residual error of the measurement of a calibration ball of radius 12.4859 mm with a 600 μm measurement range chromatic confocal gauge. Deviation of more than 10 μm from the spherical profile are observed. The best fit radius is 12.7495 mm which correspond to a radius fitting error of 264 μm.

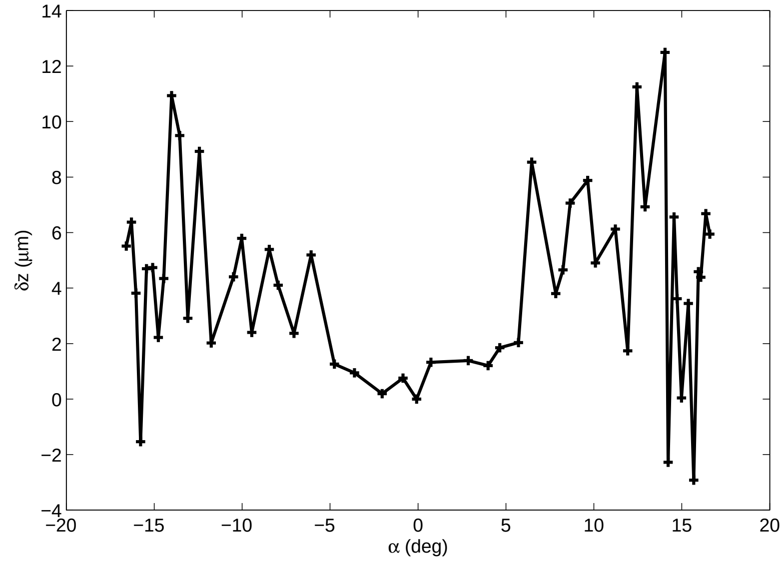

Figure 4.22: Nominal residual error of the measurement of a calibration ball of radius 12.4859 mm with a 600 μm measurement range chromatic confocal gauge with surface slope correction. Deviations of more than 10 μm from the spherical profile are observed. The best fit radius is 12.7495 mm which corresponds to a radius fitting error of 39 μm.

Figure 4.22. The P2P residual error of both measurement, with and without surface slope calibration, are comparable. Nevertheless the best fit radius is improved to reach an radius error of 39 μm. This fitting error can be improved further to reach only 5 μm by applying a spline filter of cut-off 0.2 mm to the measured data.

These results indicates that the method significantly corrects for the surface slope related error. In fact, even if the P2P residual error is not improved, the best fit radius improvement by a factor 50 indicates that the form errors associated with the surface slope related linearity error are corrected. The uncertainty of the surface slope calibration is responsible for the non-improvement of the P2P residual error. However, because this uncertainty is random, the best fit radius is not affected.

4.4 Discussion

This chapter demonstrated the experimental behaviour of the previously designed CCM. The superiority of the novel spectral irradiance model against the previously used model has been demonstrated. As a matter of fact, the novel model improves the prediction of the peak FWHM by a factor 5. In addition, the measurement standard deviation model demonstrates the capability to predict the resolution within an order of magnitude. Such a feature provides the full Ametek UPT, a distinct strategic advantage in the development of CCM. Further work could also develop the measurement standard deviation model to be based not on peak FWHM but on optical parameters of the optical head. Furthermore, using the measurement standard deviation model and experimental results, it is proven that, to optimise the measurement resolution, the measured peak spectral irradiance must be maximized.

The low cost version of the CCM features a resolution better than 100 nm over 5.7 mm of the measurement range with a linearity error below 0.01 % of the measurement range. This performance surpasses any equivalent CCM. A method is also proposed and applied to measure the spot size of the optical head onto the measured surface. The measured spot size FWHM correlates with the computed one in Chapter 3. The method uses a cleaved silicon wafer to measure the lateral step response of the system. The proposed method reduces the measurement uncertainty by not relying on a calibrated artefact. Moreover, the thermal drift coefficient is measured and satisfies the target of less $1\mu m/°C$. Furthermore, because no hysteresis is observed, an active temperature compensation of the measurement, based on calibration, can be applied. This temperature compensation could potentially reduce the linearity error induced by the temperature variation by an order of magnitude. A temperature correction would require a more precise evaluation of the temperature drift coefficient of the measurement. Currently, the measurement is based on the assumption that the distance between the optical head and the target surface is fixed. However, because of the thermal expansion of the fixture, this distance varies with the temperature. The expansion of the fixture could be corrected by using a laser interferometer measuring the common mode error of the fixture. Finally, the impact of the surface roughness and reflectivity onto the linearity error is evaluated but results indicate that the target performance is not achieved. Further work is required to mitigate this errors. Computation indicates that a measurement of the peak spectral irradiance position based on curve fitting would mitigate both errors. Regarding the reflectivity some hardware improvement is necessary to improve the calibration of the surface reflectivity linearity error.

The high resolution version of the CMM exhibits a resolution better than 10 nm over a measurement range of more than 200 μm with a linearity error of less than 0.02 % of the measurement range. Furthermore, the origin of the slope related linearity error is studied and a method to correct them is presented. This method improves the best fit radius on a calibration ball of 12.4952 mm radius by a factor 50 but does not improve the P2P residual form error. However, this method has yet to be implement to the high resolution version of the CCM. To both apply and reduce the uncertainty of the the surface slope calibration, the high resolution version of the CCM must be implemented into a high precision CMM. In fact, the high resolution version of the CCM is currently being implemented into a SPDT and measurements are anticipated within the next months.

Chapter 5

Conclusion and future work

5.1 Discussion

This work embodied in this thesis has focused on the design, development, and evaluation of a state of the art CCM. Using a generic yet flexible design method, a high resolution and low cost version of the CCM have been developed and tested within their respective measurement environments.

The former outperforms every aspect of comparable commercial systems. Thanks to the novel SDS approach, the system exhibits a longer working distance than optical heads with similar measurement ranges. Moreover, because the optical head uses only two off-the-shelf lenses and one mass produceable plastic SDS, the cost involved in the manufacture of the system is considerably lower than other CCMs. Furthermore, the measurement standard deviation model coupled with the spectral irradiance model allows a rapid product design cycle; this has enables Solartron Ltd. to rapidly develop a large catalogue of optical heads. To sum up, the presently designed low cost version of the CCM gives Solartron Ltd., both a cost leadership and differentiation strategic advantage.

The high resolution version of the CCM provides Precitec Inc. with a unique in-line metrology capability. Once more, thanks to the tunable chromatic dispersion of the SDS lens, the optical head of the high resolution version of the CCM exhibits the highest ever achieved CCM resolution with a working distance of more than 12 mm with. The achieved resolution is better than 10 nm at 200 Hz.

Previous to this system, the highest ever achieved resolution was better than 10 nm at 2 Hz. Thus high resolution version for the CCM is better by two orders of magnitude compared with the previous technology leader. Furthermore, by using the measurement standard deviation model, the chromatic dispersion of the optical head is designed to be minimum in order to increase the sensitivity of the measurement to improve the measurement resolution. This system provides Precitec Inc. a strong differentiation strategic advantage.

5.1.1 Design of state of the art chromatic confocal systems

Chapter 3 presents in the first instance a general CCM system design based on analytical models. These models allow the optimisation of the basic parameters of the CCM. Coupled with a literature review on the currently available technologies for the sub-systems of the CCM, a low cost and high resolution version of the CCM have been designed in a deterministic fashion.

Both systems exhibit superior performance to comparable “state of the art” CCMs. The former is a compact and low cost-orientated design. Despite the low cost of this system, the challenging target performances required the use of an SDS lens. SDS lenses allow the design of high chromatic dispersion and irradiance efficiency to be mass produced inexpensively using injection molding. This system is currently going through its pre-production phase and is expected to be sold by the end of 2015.

The high resolution version is designed to exhibit a resolution better than 10 nm over a measurement range of at least 50 μm. This optical head exhibits the highest resolution for commercially available systems. Furthermore, commercially available optical heads with comparable measurement ranges exhibit a working distance of half the value. This performance can only be achieved by using SDS lenses to tailor the chromatic dispersion of the optical head.

5.1.2 Evaluation and linearity improvements of non-contact distance measurement gauge

Chapter 4 is focused on the evaluation and linearity improvement of the both systems designed in Chapter 3. In the first instance, the standard deviation and spectral irradiance models are validated experientially using the low cost version of the CCM. The correlation the between predicted and measured values is satisfactory. The gained confidence in the model is crucial for future work. Indeed, Taylor Hobson Ltd. can now use the models to reduce its design cycles and time-to-market for such CCM products.

Chapter 4 also compares the performance of the low cost and high resolution versions of the CCM against the target values set in Chapter 3. All the target performances are matched for both systems. Furthermore, a method for evaluating the spot size using a cleaved silicon wafer is developed. This method improves the precision of the measurement by providing a 2 or 3 dimensional representation of the irradiance distribution on the surface. Furthermore, this method does not rely on the calibration of a standard. Therefore the uncertainty of the spot size measurement is reduced.

Finally Chapter 4 evaluates the behaviour of both systems in their respective measurement environments. The investigated factors for the low cost version of the CCM are the measurement environment temperature variations as well as the surface spectral reflectivity and roughness. The temperature sensitivity of the measurement is acceptable and matches the target performances. However, the impact of the surface spectral reflectivity and roughness exceeds the target. In both cases, the sources of the linearity errors are investigated and protocols to mitigate this errors proposed.

Due to the measurement protocol used with the high resolution version of the CCM, only the surface slope related linearity errors are relevant. The sources of the slope related errors are investigated and the origin of such errors highlighted for the first time. Because the slope related linearity error is related to the form and alignment error of the optical elements of the optical head, every optical head must be calibrated for the slope related error. A protocol is proposed and applied to calibrate the slope related error.

5.2 Future prospects

Although this thesis attempts to be as complete as possible, several areas of the work completed in this thesis can be investigated even further.

5.2.1 Measurement standard deviation model

The novel measurement standard deviation model offers a unique design tool to reduced the time to market for a CCM system. Despite the novel capability to predict the measurement uncertainty, Chapter 4 highlighted the limited confidence in the model; for instance, the model is based on the detection of a Gaussian peak using a Blais-Rioux peak detector.

The peak is known to not follow a Gaussian distribution but a profile expressed in Equation 3.3. Furthermore, Chapter 4 highlights the linearity issues related to the use of a peak detector. Using Equation 3.3, the maximum position of the peak can be determined using a curve fitting method. Such a method has not been applied for computation time reasons. However, modern multi-core computers and Digital Signal Processors (DSPs) can now carry out the required computation at a sampling rate exceeding 30 kHz. In sum, using a similar method as in Section 3.1 yet using a curve fitting, a measurement standard deviation model expressed in optical parameters rather than peak FWHM could be developed. Moreover, the standard deviation of the line sensor reading is assumed to follow a Gaussian distribution. One could use the measured reading standard deviation of the line sensor in order to develop an even more precise, although less flexible, CCM measurement standard deviation model.

5.2.2 NIR non-contact distance measurement gauge

For strategic reasons, this thesis partially fulfilled the goal of providing Taylor Hobson Ltd. with the most precise non-contact distance measurement sensor. In fact, during the period of this work, Taylor Hobson Ltd. acquired Luphos Gmbh. and with it the Multi-Wavelength Light Interferometer (MWLI) technology. Therefore, the strategic need for the most precise non-contact distance measurement sensor has been mitigated. Nevertheless, the MWLI suffers from limitations in sampling rate and NA. Using the current architecture developed in Section 3.4, the measurement resolution is limited by the total spectral irradiance coupled into the optical fibre and the reading noise of the line sensor. In order to be a viable substitute to the MWLI, the CCM must reach a sampling rate exceeding 2 kHz and a measurement resolution better than 5 nm.

As suggested by Equation 3.13, the measurement uncertainty can only be reduced further by reducing the normalised line sensor reading standard deviation. In order to maintain the resolution at 5 nm at a sampling rate of more than 2 kHz the spectral irradiance must be significantly increased.

In order to reach the required sampling rate of more than 2 kHz with a high DNR line sensor, the only suitable light source is a SLED such as the SLD-34-HP with a wavelength band from 810 nm to 880 nm [136]. Using such an SLED, the spectral range is 30 nm. With this spectral range, an optical head with a measurement range of 100 μm, a working distance of 12 mm, NA of 0.8, and a magnification of 0.1 as been designed. Hence, using Equation 3.4, the chromatic confocal peak FWHM is 1 μm. Because SLEDs uses a mono-mode optical fibre and the system magnification is 0.1, the image of the pinhole on the surface is the diffraction limit of the system. Since the SLD-34-HP operates in the NIR domain, the SDS lens can be machined directly on ZnSe. Because no plastic part are used, the thermal drift of the measurement should be similar to 0.056 $\mu m/K$ shown in Table 3.9 for the full glass design.

To reduce the normalised line sensor reading standard deviation, the DNR of the line sensor must be enhanced. This suggest the use of CMOS line sensors. The proposed sensor is the Dr-2k-500 [84] from Awaiba Gmbh. The full well capacity is 46,000 electrons and the temporal noise is 22 electrons which is equivalent to a normalised line sensor reading noise of 5.10^{-4}. If 2,000 pixels of the Dr-2k-500 cover the 100 μm measurement range, the FWHM of 1 μm is equivalent to 20 pixels. Therefore, using Equation 3.12, the measurement standard deviation is 2.10^{-3} pixels, which is equivalent to a resolution of 0.3 nm. The maximum sampling rate is estimated to be 168 kHz for a perfect mirror and 5 kHz for glass. Such a high resolution is likely to be deteriorated due to temporal effects such as vibration. Nevertheless, thanks to the fact that the CCM does not have any moving parts, vibration related errors are minimum.

5.2.3 Implementation in surface and roundness measurement instruments

The next action for Taylor Hobson Ltd. is to implement the high resolution version of the CCM into a roundness and surface measurement instrument.

In fact, even though Taylor Hobson Ltd. recently acquired the MWLI technology, the CCM offers advantages such as cost and NA. The MWLI requires an additional rotary axis to maintain the optical axis of the probe normal to the surface which limits the measurement of rotationally symmetric parts when measuring a spiral scan or cylindrical in raster scan. Therefore, the CCM offers a simpler approach to the measurement of more complex parts such as free-forms, albeit with the caveat that such simplicity is at the cost of surface slope introduced errors. Clearly the envelope of such CCM applicability needs to be explored. However, as discussed in 5.2.2 and as exemplified by Taylor Hobson Ltd. CCI, there are strong arguments to suggest that the propose NIR, high NA version would very substantially address there caveats.

As a final comment, the CCM designed in the previous section can potentially improve both the sampling frequency and resolution compared to the MWLI technology.

5.2.4 Reduction of the surface slope calibration time

The time required to carry the calibration of a high precision surface metrology instrument is crucial. In fact, measurement cycle time is one of nowadays highest concern for costumers. Because the high resolution version of the CCM has to be calibrated as a function of the position within the range of measurement and the surface local slope, the calibration protocol using a calibrated sphere required 10 traces to be measured. The measurement of 10 traces is extremely time consuming.

SPDT uses a high precision rotatory axis to machine work-pieces. If the rotary axis is used during a measurement an addition degree of freedom is added and the surface is measured in 3 dimensions following a spiral trace. This additional degree of freedom can be used to simultaneously calibrate an optical head along the z and ϕ axis, respectively the position within the range of measurement and the local surface slope. However, a spherical artefact lacks the degree of freedom to enable calibration along the z and ϕ axis. Instead, a cylinder, tilted by an angle α around the x axis, is proposed. The measured height in Cartesian coordinates can be expressed as

$$z(x,y) = \frac{x^2}{R\left(1+\sqrt{1-\frac{x^2}{R^2}}\right)} + y\ \tan\alpha. \tag{5.1}$$

The normal vector to the surface $N(x,y)$ can be expressed as

$$N(x,y) = \begin{bmatrix} z_x(x,y) \\ z_y(x,y) \\ \sqrt{1-z_x(x,y)^2-z_y(x,y)^2} \end{bmatrix}, \tag{5.2}$$

where $z_x(x,y) = \partial z/\partial x$ and $z_y(x,y) = \partial z/\partial x$ are partial derivatives.

Hence, the local surface slope is expressed as

$$\phi(x,y) = \arccos\sqrt{1-z_x(x,y)^2-z_y(x,y)^2}. \tag{5.3}$$

Hence, by combining Equation 5.1 and 5.3 the calibration region A_{Cal} is defined as

$$A_{Cal}(\phi, z) = \begin{cases} \phi(r, \theta) \\ z(r, \theta) + \Delta z \end{cases} \quad \text{for} \quad r \in \{0, C_R\} \quad \text{and} \quad \theta \in \{0, 2\pi\}\,. \tag{5.4}$$

where C_R is the maximum radius of the measurement spiral. Equation 5.4 has been converted to cylindrical coordinate system to suit the measurement of the artefact using a spiral trace.

Such an artefact permits a calibration region in the (z, ϕ) plane to be covered at an arbitrary high density. Thus, the need for extrapolation between the original measurement lines is substantially reduced. Figure 5.1, shown the calibration region A_{Cal} for the low cost version of the CCM. Using a cylinder of radius 10 mm, tilted by 2.35°, only three measurements are necessary to cover the full measurement range from 2.35° to 30°.

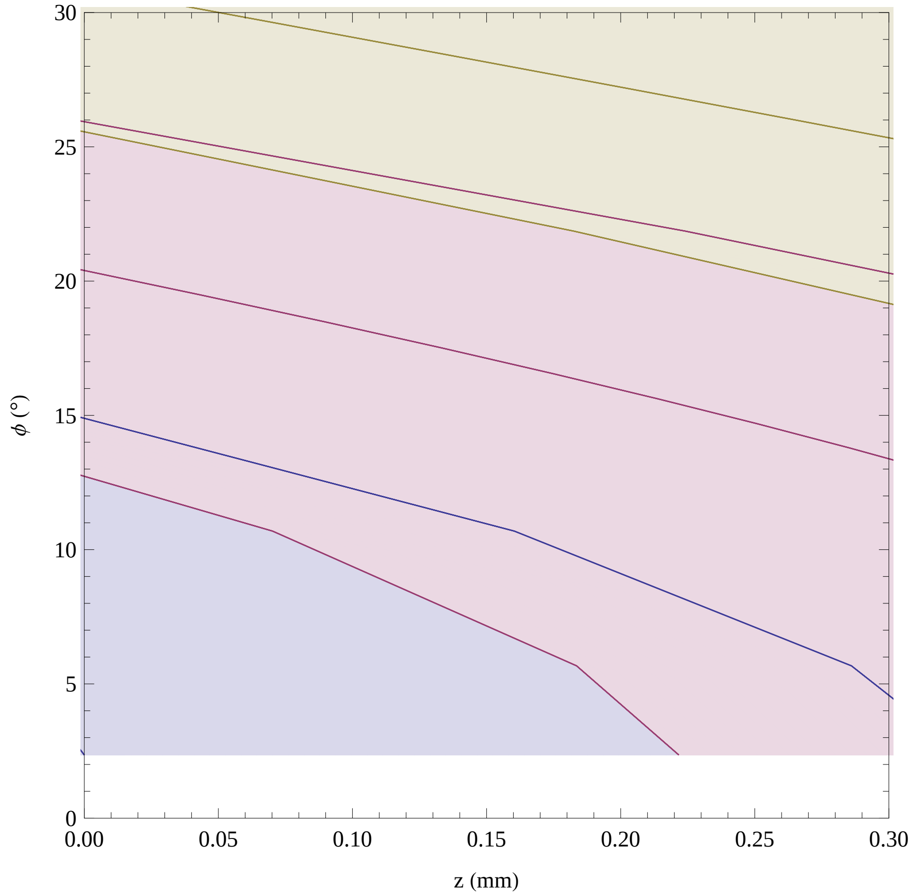

Figure 5.1: three calibrations region described in Equation 5.4 for R = 10 mm, $\alpha = 2.35°$, $\Delta z = \{0,\ 0.6,\ 1.2\}$ mm.

However, this method does not permit the surface slope related error below the tilt angle α of the cylinder to be measured. However, the sensitivity of the surface slope related linearity error is minimum for small angles. Therefore, the slope related linearity error can be extrapolated for surface slopes below the cylinder tilt angle α.

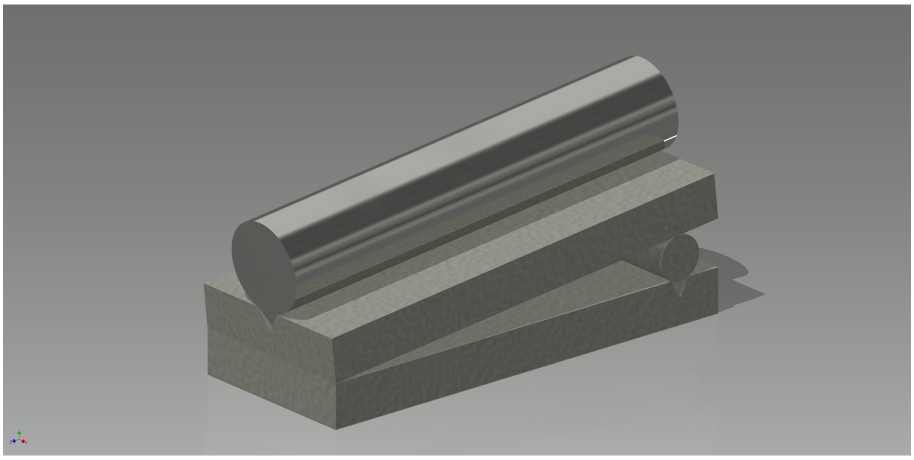

Figure 5.2: Graphical representation of the cylindrical artefact used for the calibration of a CCM head in the (z, ϕ) plane. The cylinder is mounted on an fixture to introduce the required tilt angle α.

The cylindrical artefact can be machined from a tungsten carbide rod with an electroless nickel plating using an SPDT machine. The machined rod can then be tilted to the required angle using a fixture as shown in Figure 5.2. The cylinder radius can be calibrated using a white light interferometer.

5.2.5 Research in high precision dimensional metrology

Currently two technologies are growing rapidly in the field of high precision dimensional metrology; the MWLI and the NVTM presented in Section 2.1. The MWLI and NVTM reduce the measurement cycle time while the data density is increased. Both technologies rely on high precision positioning control technology. In fact, high precision manufacturing being a fast growing market, those systems grow in synergy with high precision positioning control technologies.

Because the TRL of the MWLI is high, this technology currently goes through a phase of market expansion. Recently acquired by Taylor Hobson Ltd., the application domain has recently been expended from radially symmetric lenses, measured using a spiral profile [137], to cylindrical lenses, measured using a raster scan profile [138]. Both spiral and raster scans can only measure parts with five degrees of freedom. Hence, the remaining application domain to develop is that of free-form parts with six degrees of freedom.

The interest in the NVTM is growing and various institutions, such as Rochester University [139], are working on this method. While yet restricted to parts with low surface gradient, the NVTM can measure free-form surfaces. However, the practical industrial implementation of the NVTM is still marginal.

While high precision non-contact dimensional measurement system fill a market niche for high end product, a market gap is left for mid-precision non-contact dimensional metrology, with a measurement repeatability below $1\mu m$. In terms of contact measurement system, the current market leader that addresses both these high and medium precision regimes is Form Talysurf PGI [140]. However, non-contact instruments could potentially reduce further the measurement cycle time and damage on the surface while maintaining the measurement repeatability.

5.3 Conclusion

Two CCM systems have been developed and evaluated; a low cost and high resolution version. Both systems exhibit state of the art performance. The low cost and high resolution version of the CCM were designed using novel theoretical models of the CCM. Those models improve the performance of the systems and reduce the number of required design cycles. Furthermore, using SDS lens, the application domain of the CCM has been increased. The low cost and high resolution version of the CCM have been fully evaluated. The linearity of the systems is improved by an order of magnitude compare to equivalent commercially available designs. However, further research is necessary to improve the measurement of tilted and rough surfaces. Both systems are currently in pre-production phase.

Further research opportunities are presented in this chapter. Those future prospect emphasise the necessity to reduce the measurement cycle time of a part and to increase the data density.

References

[1] "The Taylor Hobson Story." [Online]. Available: http://www.taylor-hobson.com/history.html

[2] "PGI Dimension specification." [Online]. Available: http://www.taylor-hobson.com/products/10/64.html#PGI-Dimension2

[3] B. N. Taylor, *Guidelines for Evaluating and Expressing the Uncertainty of NIST Measurement Results.* DIANE Publishing, 2009.

[4] BIPM, IEC, ILAC, IFCC, IUPAC, ISO, OIML, and IUPAP, "International vocabulary of metrology Basic and general concepts and associated terms, 2008," *JCGM 200*, pp. 99–12, 2008.

[5] L. J. Porter and A. J. Parker, "Total quality management-the critical success factors," *Total quality management*, vol. 4, no. 1, pp. 13–22, 1993.

[6] D. H. Stamatis, *Six Sigma Fundamentals: A Complete Guide to the System, Methods and Tools.* Productivity Press, 2004.

[7] D J Whitehouse, "Surface metrology," *Measurement Science and Technology*, vol. 8, no. 9, p. 955, May 1997.

[8] L. C. Tang, T. N. Goh, S. W. Lam, and C. W. Zhang, "Fortification of Six Sigma: expanding the DMAIC toolset," *Quality and Reliability Engineering International*, vol. 23, no. 1, pp. 3–18, 2007.

[9] "LVDT, Half Bridge and Digital Transducer Theory." [Online]. Available: http://www.solartronmetrology.com/service-support/knowledge-base/theory.aspx

[10] I. K. Buehring and D. Mansfield, "Probe measurement apparatus using a curved grating displacement interferometer," *US Patent 5,517,307 A*, 1996. [Online]. Available: http://www.google.de/patents/US5517307

[11] X. Jiang, P. J. Scott, D. J. Whitehouse, and L. Blunt, "Paradigm shifts in surface metrology. Part II. The current shift," *Proceedings of the Royal Society A: Mathematical, Physical and Engineering Science*, vol. 463, no. 2085, pp. 2071–2099, 2007.

[12] P. Eaton and P. West, *Atomic Force Microscopy.* OUP Oxford, 2010.

[13] M. Bass, C. DeCusatis, and J. Enoch, *Handbook of optics, Volume II: Design, fabrication and testing, sources and detectors, radiometry and photometry*, 3rd ed. McGraw-Hill Professional, Sep. 2009.

[14] "Taylor Hobson Ltd, CCI Optic," Technical Specifications, 2013. [Online]. Available: http://www.taylor-hobson.com/products/33/109.html

[15] C. E. Shannon, "Communication in the presence of noise," *Proceedings of the IRE*, vol. 37, no. 1, pp. 10–21, 1949.

[16] P. Hariharan, *Optical Interferometry*, ser. Electronics & Electrical. Academic Press, 2003.

[17] A. D. Bankhead, I. McDonnell, and Others, "Surface profiling apparatus," *US Patent 7,385,707 B2*, 2008. [Online]. Available: http://www.google.com/patents/US7385707

[18] M. Minsky, "Microscopy apparatus," *US Patent 3,013,467 A*, 1961. [Online]. Available: http://worldwide.espacenet.com/publicationDetails/biblio?CC=US&NR=3013467A&KC=A&FT=D

[19] T. R. Corle, C.-H. Chou, and G. S. Kino, "Depth response of confocal optical microscopes," *Optics Letters*, vol. 11, no. 12, 1986.

[20] G. B. Airy, "On the Diffraction of an Object-glass with Circular Aperture," *Transactions of the Cambridge Philosophical Society*, vol. 5, pp. 283–291, 1835.

[21] R. L. Price and W. G. Jerome, *Basic Confocal Microscopy.* Springer, 2011.

[22] F. W. J. Olver, *NIST handbook of mathematical functions.* Cambridge University Press, 2010.

[23] H. Mintzberg, “Patterns in strategy formation,” *Management science*, vol. 24, no. 9, pp. 934–948, 1978.

[24] R. E. Miles, C. C. Snow, A. D. Meyer, and H. J. Coleman, “Organizational strategy, structure, and process,” *Academy of management review*, vol. 3, no. 3, pp. 546–562, 1978.

[25] “Key Enabling Technologies.” [Online]. Available: http://ec.europa.eu/enterprise/sectors/ict/key$\delimiter”026E30F$_technologies/

[26] T. R. Thomas, “Trends in surface roughness,” *International Journal of Machine Tools and Manufacture*, vol. 38, no. 5, pp. 405–411, 1998.

[27] M. Stedman, “Basis for comparing the performance of surface-measuring machines,” *Precision Engineering*, vol. 9, no. 3, pp. 149–152, 1987. [Online]. Available: http://www.sciencedirect.com/science/article/pii/0141635987900328

[28] X. Jiang, P. J. Scott, D. J. Whitehouse, and L. Blunt, “Paradigm shifts in surface metrology. Part 1. Historical philosophy,” *Proceedings of the Royal Society A: Mathematical, Physical and Engineering Science*, vol. 463, no. 2085, pp. 2049–2070, 2007.

[29] D. R. Rink and J. E. Swan, “Product life cycle research: A literature review,” *Journal of business Research*, vol. 7, no. 3, pp. 219–242, 1979.

[30] G. S. Day, *Analysis for strategic market decisions*, ser. West Series on Strategic Market Management. West Pub. Co., 1986.

[31] B. Hedley, “Strategy and the ”business portfolio”,” *Long Range Planning*, vol. 10, no. 1, pp. 9–15, 1977. [Online]. Available: http://www.sciencedirect.com/science/article/pii/0024630177900425

[32] B. C. Group, “The Product Portfolio Concept: Perspective,” *Boston Consulting Group*, vol. 66, 1970.

[33] M. E. Porter, “How Competitive Forces Shape Strategy,” *Harvard Business Review*, vol. March–Apr, p. 6, 1979.

[34] D. N. Dwivedi, *Microeconomics: Theory And Applications.* Pearson Education, 2002.

[35] “Marh Gmbh.” [Online]. Available: http://www.mahr.de/

[36] “Panasonic Inc.” [Online]. Available: http://industrial.panasonic.com

[37] “Sensofar.” [Online]. Available: http://www.sensofar.com/sensofar/

[38] “Luphos Gmbh.” [Online]. Available: http://www.luphos.de/

[39] “Aerotech Inc.” [Online]. Available: http://www.aerotech.com/

[40] M. E. Porter, *Competitive Advantage: Creating and Sustaining Superior Performance.* Free Press, 2008. [Online]. Available: http://books.google.co.uk/books?id=H9ReAijCK8cC

[41] M. E. Porter and V. E. Millar, “How information gives you competitive advantage,” 1985. [Online]. Available: http://www.ida.liu.se/~TDEI65/documents/8500002422.pdf

[42] “Ametek Inc. ultra precision division.” [Online]. Available: http://www.ametek.com/businesses/index.aspx

[43] M. E. Porter, *Competitive Strategy: Techniques for Analyzing Industries and Competitors.* Free Press, 2008.

[44] “Solartron metrology Ltd.” [Online]. Available: http://www.solartronmetrology.com/

[45] “Precitech Inc.” [Online]. Available: http://www.precitech.com/

[46] E. Papastathopoulos, K. Körner, and W. Osten, "Chromatic confocal spectral interferometry," *Applied optics*, vol. 45, no. 32, pp. 8244–8252, 2006.

[47] J. Petter, "Multi Wavelength Interferometry for High Precision Distance Measurement," *Proceedings OPTO 2009 & IRSˆ2 2009*, pp. 129–132, 2009.

[48] H. Martin and X. Jiang, "Dispersed reference interferometry," *CIRP Annals - Manufacturing Technology*, vol. 62, no. 1, pp. 551–554, Jan. 2013. [Online]. Available: http://eprints.hud.ac.uk/18513/

[49] B. B. H. Kleemann, M. Seesselberg, J. Ruoff, and M. Seeß elberg, "Design concepts for broadband high-efficiency DOEs," *Journal of the European Optical Society-Rapid publications*, vol. 3, Apr. 2008. [Online]. Available: https://www.jeos.org/index.php/jeos_rp/article/view/176

[50] E. Abbe, "Measuring instruments for physicists," *Journal for Instrumental Information*, vol. 10, pp. 446–448, 1890.

[51] "Novacam." [Online]. Available: http://www.novacam.com/products/profilometers/

[52] P. Drabarek, "Short coherence fiber probe interferometric measuring device," *US Patent 6741355 B2*, 2004.

[53] F. Depiereux, N. König, T. Pfeifer, and R. Schmitt, "Fiber-based white-light interferometer with improved sensor tip and stepped mirror," *IEEE Transactions on Instrumentation and Measurement*, vol. 56, no. 6, pp. 2279–2283, 2007.

[54] F. Depiereux, P. Lehmann, T. Pfeifer, and R. Schmitt, "Fiber-optical sensor with miniaturized probe head and nanometer accuracy based on spatially modulated low-coherence interferogram analysis." *Applied optics*, vol. 46, no. 17, pp. 3425–3431, 2007.

[55] H. Matsumura, D. Tonaru, T. Kitayama, K. Usuki, T. Kojima, J. Uchikoshi, Y. Higashi, and K. Endo, "Effects of a laser beam

profile to measure an aspheric mirror on a high-speed nanoprofiler using normal vector tracing method," *Current Applied Physics*, vol. 12, Supple, no. 0, pp. S47–S51, 2012. [Online]. Available: http://www.sciencedirect.com/science/article/pii/S1567173912001617

[56] R. Nicolaus, J. Petter, T. Tschudi, A. Noack, and Others, "Fibre-optic multiwavelength interferometer (mwli) for the absolute measurement of distances and topologies for surfaces at a large operating distance," 2010.

[57] G. Molesini, G. Pedrini, P. Poggi, and F. Quercioli, "Focus-wavelength encoded optical profilometer," *Optics Communications*, vol. 49, no. 4, pp. 229–233, Mar. 1984.

[58] W. S.-c. Chang, *Principles of lasers and optics.* Cambridge University Press, 2005.

[59] K. Meiners-Hagen, R. Schödel, F. Pollinger, and A. Abou-Zeid, "Multi-wavelength interferometry for length measurements using diode lasers," *Measurement Science Review*, vol. 9, no. 1, pp. 16–26, 2009.

[60] J. C. Mankins, "Technology readiness levels: A white paper," *Office of Space Access and Technology. NASA*, vol. 6, 1995. [Online]. Available: http://www.hq.nasa.gov/office/codeq/trl/trl.pdf

[61] P.-H. Cu-Nguyen, A. Grewe, M. Hillenbrand, S. Sinzinger, A. Seifert, and H. Zappe, "Tunable hyperchromatic lens system for confocal hyperspectral sensing," *Optics Express*, vol. 21, no. 23, pp. 27 611–27 621, Nov. 2013. [Online]. Available: http://www.opticsexpress.org/abstract.cfm?URI=oe-21-23-27611

[62] "Stil SA Catalogue." [Online]. Available: http://www.stilsa.com/catalog2/pdf/catalogue.pdf

[63] "Precitech Gmbh." [Online]. Available: http://www.precitec.de/en/products/optical-measuring-technology/how-it-works/

[64] "Nanovea." [Online]. Available: http://www.nanovea.com/chromatic-confocal.html

[65] "Micro Epsilon Gmbh. catalogue." [Online]. Available: http://www.micro-epsilon.co.uk/download/products/cat--confocalDT--en.pdf

[66] H. J. Jordan, M. Wegner, and H. Tiziani, "Highly accurate non-contact characterization of engineering surfaces using confocal microscopy," *Measurement Science and Technology*, vol. 9, p. 1142, 1998.

[67] H. J. Tiziani and H. M. Uhde, "Three-dimensional image sensing by chromatic confocal microscopy," *Applied Optics*, vol. 33, no. 10, 1994.

[68] R. Hoenicka and A. Fink, "Method for compensating for temperature related measurement errors in a confocal chromatic measuring distance sensor," *US Patent 8,248,598 B2*, 2012.

[69] S. Cha, P. C. Lin, L. Zhu, P.-C. Sun, and Y. Fainman, "Nontranslational three-dimensional profilometry by chromatic confocal microscopy with dynamically configurable micromirror scanning," *Applied Optics*, vol. 39, no. 16, p. 2605, Jun. 2000.

[70] C. Yang, K. Shi, H. Li, Q. Xu, V. Gopalan, and Z. Liu, "Chromatic second harmonic imaging," *Optics Express*, vol. 18, no. 23, pp. 23 837–23 843, Nov. 2010. [Online]. Available: http://www.opticsexpress.org/abstract.cfm?URI=oe-18-23-23837

[71] A. K. Ruprecht, T. F. Wiesendanger, and H. J. Tiziani, "Chromatic confocal microscopy with a finite pinhole size." *Optics letters*, vol. 29, no. 18, pp. 2130–2132, 2004.

[72] P. C. Lin, P. C. Sun, L. Zhu, and Y. Fainman, "Single-shot depth-section imaging through chromatic slit-scan confocal microscopy," *Applied optics*, vol. 37, no. 28, pp. 6764–6770, 1998.

[73] S. L. Dobson, P. C. Sun, and Y. Fainman, "Diffractive lenses for chromatic confocal imaging." *Applied optics*, vol. 36, pp. 4744–4748, 1997.

[74] G. J. Swanson, "Binary optics technology: the theory and design of multi-level diffractive optical elements," Massachusetts Intitute of Technology, Tech. Rep., 1989.

[75] S. R. Goldstein, "Confocal scanning laser microscope having no moving parts," *US Patent 4,827,125 A*, 1989. [Online]. Available: http://www.google.com/patents/US4827125

[76] A. W. Krause, "Spatially light modulated confocal microscope and method," *European Pattent 0911667 B1*, 2003. [Online]. Available: http://www.google.com/patents/EP0911667B1?cl=en

[77] K. Carlsson, P.-E. Danielsson, R. Lenz, A. Liljeborg, L. Majlöf, and N. Å slund, "Three-dimensional microscopy using a confocal laser scanning microscope," *Optics Letters*, vol. 10, no. 2, pp. 53–55, 1985.

[78] M. Hillenbrand, A. Grewe, and S. Sinzinger, "Parallelized Chromatic Confocal Systems Enable Efficient Spectral Information Coding," *Iraqui Journal of Applied Physics*, vol. 9, pp. 3–4, 2013. [Online]. Available: http://iraqiphysicsjournal.com/wp-content/uploads/2012/11/3-41.pdf

[79] P. Baker and W. Kuhn, "Distance measuring confocal microscope," *US Patent 5,785,651*, 1998. [Online]. Available: http://www.google.com/patents/US5785651

[80] E. Altendorf, "Chromatic sensor lens configuration," *US Patent 7,626,705*, 2009. [Online]. Available: http://www.google.com/patents/US7626705

[81] D. Sesko, "Dynamic compensation of chromatic point sensor intensity profile data selection," *US Patent 7,990,522*, 2011. [Online]. Available: http://www.google.com/patents/US7990522

[82] K. Atherton, M. Nahum, and D. Sesko, “On-site calibration method and object for chromatic point sensors,” *US Patent 7,873,488*, 2011. [Online]. Available: http://www.google.com/patents/US7873488

[83] D. Sesko, “Intensity compensation for interchangeable chromatic point sensor components,” *US Patent 7,876,456*, 2011. [Online]. Available: http://www.google.com/patents/US7876456

[84] “Awaiba Gmnh. dr-2k-500 Datasheet.” [Online]. Available: http://www.awaiba.com/v2/wp-content/uploads/2010/01/DRAGSTER_SENSOR_short_SPECIFICATION_v_3-03.pdf

[85] F. Blais and M. Rioux, “Real-time numerical peak detector,” *Signal Processing*, vol. 11, no. 2, pp. 145–155, 1986.

[86] H. N. Anwer, N. El-Hayek, X. Yuan, and N, “Characterization of the main error sources of chromatic confocal probes for dimensional measurement,” *Measurement Science and Technology*, vol. 25, no. 4, p. 44011, 2014. [Online]. Available: http://stacks.iop.org/0957-0233/25/i=4/a=044011

[87] ISO, “BS EN ISO 25178-602:2010, Geometrical product specifications (GPS). Surface texture. Areal. Nominal characteristics of non-contact (confocal chromatic probe) instruments,” 2010.

[88] C.-H. Niu, W.-Y. Deng, X.-H. Mao, X. Gao, and C. Han, “Theoretical and experimental study on chromatic confocal position sensor,” in *Proc. SPIE*, 2010, pp. 78 531B–78 531B–8.

[89] Y. Xie, “Chromatic confocal point sensor aperture configuration,” *European Pattent 2388635 A1*, 2011. [Online]. Available: https://www.google.com/patents/EP2388635A1?cl=en

[90] J. K. Patel and C. B. Read, *Handbook of the Normal Distribution, Second Edition*, ser. Statistics: A Series of Textbooks and Monographs. Taylor & Francis, 1996.

[91] Osram, "XBO Xenon short-arc lamps without reflector." [Online]. Available: http://www.osram.com/osram_com/products/lamps/specialty-lamps/xbo/xbo/index.jsp?productId=ZMP_56398

[92] S. Shionoya and W. M. Yen, *Phosphor Handbook*, ser. The CRC Press laser and optical science and technology series. Taylor & Francis, 1998.

[93] P. Mottier, *LED for Lighting Applications.* John Wiley & Sons, 2009.

[94] Exalos, "Exalos SLEDs specification." [Online]. Available: http://www.exalos.com/sled-modules.html

[95] G. Alphonse, D. Gilbert, M. Harvey, and M. Ettenberg, "High-power superluminescent diodes," *IEEE Journal of Quantum Electronics*, vol. 24, no. 12, pp. 2454–2457, Dec. 1988. [Online]. Available: http://adsabs.harvard.edu/abs/1988IJQE...24.2454A

[96] J. G. F. Wolfgang Drexler, Ed., *Optical Coherence Tomography: Technology and Applications.* Springer, Sep. 2008.

[97] C. Holtmann, P. A. Besse, and H. Melchior, "High power superluminescent diodes for 1.3 mu m wavelengths," *Electronics Letters*, vol. 32, pp. 1705–1706, 1996.

[98] A. M. Smith, M. C. Mancini, and S. Nie, "Bioimaging: second window for in vivo imaging." *Nature nanotechnology*, vol. 4, no. 11, pp. 710–1, Nov. 2009. [Online]. Available: http://www.pubmedcentral.nih.gov/articlerender.fcgi?artid=2862008&tool=pmcentrez&rendertype=abstract

[99] NKTphotonics, "NKTphotonics supercontinuum laser specification." [Online]. Available: www.nktphotonics.com/superk_extreme_specifications?cid=7856

[100] R. Alfano, *The Supercontinuum Laser Source.* Springer, 2006.

[101] K. Shi, P. Li, S. Yin, and Z. Liu, "Chromatic confocal microscopy using supercontinuum light," *Optics Express*, vol. 12, no. 10, pp. 2096–2101, May

2004. [Online]. Available: http://www.opticsexpress.org/abstract.cfm?URI=oe-12-10-2096

[102] A. Ghatak and K. Thyagarajan, *An Introduction to Fiber Optics.* Cambridge University Press, 1998.

[103] E. Hecht, *Optics*, 4th ed. Addison Wesley, 2002.

[104] Sellmeier, "Zur Erklarung der abnormen Farbenfolge im Spectrum einiger Substanzen," *Annalen der Physik*, vol. 219, no. 6, pp. 272–282, 1871. [Online]. Available: http://dx.doi.org/10.1002/andp.18712190612

[105] T. Stone and N. George, "Hybrid diffractive-refractive lenses and achromats." *Applied optics*, vol. 27, pp. 2960–2971, 1988.

[106] T. R. Sales and G. M. Morris, "Diffractive refractive behavior of kinoform lenses," *Applied Optics*, vol. 36, pp. 253–257, 1997.

[107] "Zeonex properties." [Online]. Available: http://www.zeonex.com/applications_optical.asp

[108] "Norland NOA89 properties." [Online]. Available: http://www.norlandprod.com/adhesives/NOA89.html

[109] T. Wang, H. Liu, H. H. Zhang, Q. Sun, and Z. Lu, "Effect of incidence angles and manufacturing errors on the imaging performance of hybrid systems," *Journal of Optics*, vol. 13, no. 3, p. 35711, Mar. 2011. [Online]. Available: http://iopscience.iop.org/2040-8986/13/3/035711

[110] M. J. Riedl, "Predesign of diamond turned refractive/diffractive elements for IR objectives," in *NASA. Marshall Space Flight Center, Conference on Binary Optics: An Opportunity for Technical Exchange*, Aug. 1993, pp. p 369–385. [Online]. Available: http://ntrs.nasa.gov/search.jsp?R=19940012886

[111] "Precitech Inc. Nanoform 700 lathe description." [Online]. Available: http://www.precitech.com/products/nanoform700ultra/nanoform_700_ultra.html

[112] J. M. Sasian and R. A. Chipman, "Staircase lens: a binary and diffractive field curvature corrector," *Applied optics*, vol. 32, no. 1, pp. 60–66, 1993.

[113] D. A. Pommet, M. G. Moharam, and E. B. Grann, "Limits of scalar diffraction theory for diffractive phase elements," *Journal of the Optical Society of America A*, vol. 11, p. 1827, 1994.

[114] "Zemax Inc." [Online]. Available: https://www.zemax.com/home

[115] "Code V." [Online]. Available: http://optics.synopsys.com/codev/

[116] N.-H. Kim, "How Diffractive Surfaces are Modeled in Zemax." [Online]. Available: https://www.zemax.com/support/knowledgebase/how-diffractive-surfaces-are-modeled-in-zemax

[117] E. W. Weisstein, "Direction Cosine." [Online]. Available: http://mathworld.wolfram.com/DirectionCosine.html

[118] I. S. Richard, B. L. Swaby, R. J. Ryall, S. E. Solberg, and E. W. Anthon, "Monolithic linear variable filter and method of manufacture," Feb. 1999. [Online]. Available: http://www.google.com/patents/US5872655

[119] J. W. Goodman, *Introduction to Fourier Optics*, 3rd ed. Roberts & Company Publishers, Jan. 2005.

[120] G. C. Holst and T. S. Lomheim, *CMOS/CCD Sensors and Camera Systems.* JCD Publishing, 2011.

[121] J. Kauppinen and J. Partanen, *Fourier Transforms in Spectroscopy.* Wiley, 2001.

[122] K. J. Gå svik, *Optical Metrology*, 2nd ed. Wiley, 2002.

[123] K. F. Riley, *Mathematical Methods for the Physical Sciences: An Informal Treatment for Students of Physics and Engineering.* Cambridge University Press, 1974.

[124] H. C. So, "Adaptive single-tone frequency estimation based on autoregressive model," in *Proc. X European Signal Processing Conf., Tampere, Finland.* Citeseer, 2000.

[125] E. Mendez and K. O'Donnell, "Observation of depolarization and backscattering enhancement in light scattering from gaussian random surfaces," *Optics Communications*, vol. 61, no. 2, pp. 91–95, Jan. 1987. [Online]. Available: http://www.sciencedirect.com/science/article/pii/0030401887902252

[126] "Renishaw RLE laser encoder datasheet." [Online]. Available: http://resources.renishaw.com/download.aspx?lang=en&data=33411

[127] "Solartron Metrology Ltd. inductive gauge specifications." [Online]. Available: http://www.solartronmetrology.com/download.asbx?AttributeFileId=28326f41-538e-434a-8f89-3c950850e19c

[128] Toshiba, "Toshiba TCD1205DG datasheet." [Online]. Available: http://www.eureca.de/datasheets/01.xx.xxxx/01.04.xxxx/01.04.0059/TCD1205DG.pdf

[129] "Steinmeyer Linear stage." [Online]. Available: http://mechatronik.steinmeyer.com/en/products/1/3/products_detail/pmt160-dc/

[130] "Renishaw RLE laser encoder." [Online]. Available: http://resources.renishaw.com/en/details/data-sheet-rle-system-performance--33411

[131] F. N. Fritsch and R. E. Carlson, "Monotone Piecewise Cubic Interpolation," *SIAM Journal on Numerical Analysis*, vol. 17, pp. 238–246, 1980.

[132] ISO, "ISO 25178-2:2012, Geometrical product specifications (GPS) – Surface texture: Areal – Part 2: Terms, definitions and surface texture parameters," 2012.

[133] J. Brandup, E. Immergut, and E. Grulke, *Polymer handbook.* Wiley New York, 1999.

[134] M. Bass, C. DeCusatis, J. Enoch, V. Lakshminarayanan, G. Li, C. MacDonald, V. Mahajan, and E. V. Stryland, *Handbook of Optics, Third Edition Volume IV: Optical Properties of Materials, Nonlinear Optics, Quantum Optics.* McGraw Hill Professional, 2009.

[135] A. H. Slocum, *Precision Machine Design.* Society of Manufacturing Engineers, 1992.

[136] "Superlum Ltd." [Online]. Available: http://www.superlumdiodes.com/slds_overview.htm

[137] "LuphoScan." [Online]. Available: http://www.luphos.de/en/products/luphoscan.html

[138] "LuphoSharp 150." [Online]. Available: http://www.luphos.de/en/products/luphosharp-150.html

[139] J. Ellis and M. A. Echter, "Non-contact, Point-to-point Methods for Measuring Freeform Optics," in *Classical Optics 2014.* Washington, D.C.: OSA, 2014, p. OW2B.5.

[140] "Form TalySurf PGI." [Online]. Available: http://www.taylor-hobson.com/products/12/107.html